Magmatic-Hydrothermal Processes

along the Porphyry to Epithermal Transition

Kumulative Dissertation

zur Erlangung des akademischen Grades
„doctor rerum naturalium"
(Dr. rer. nat.)
in der Wissenschaftsdisziplin Geochemie

eingereicht an der
Mathematisch-Naturwissenschaftlichen Fakultät
der Universität Potsdam

vorgelegt von:

Malte Stoltnow

Potsdam, 12.05.2023

Malte Stoltnow
Magmatic-Hydrothermal Processes along the Porphyry to Epithermal Transition

First advisor (erster Betreuer): Priv. Doz. Dr. Philipp Weis
Second advisor (zweiter Betreuer): Dr. Volker Lüders

Referees (Gutachter):
Priv. Doz. Dr. Philipp Weis,
German Research Center for Geosciences Potsdam GFZ, Potsdam, Germany
Institute of Geosciences, University of Potsdam, Germany
apl. Prof. Dr. Uwe Altenberger,
Institute of Geosciences, University of Potsdam, Germany
Prof. Dr. Reiner Klemd,
Department of Geography and Geosciences, Friedrich-Alexander-Universität, Germany

Doctoral Committee (Promotionsausschuss):
apl. Prof. Edward Sobel, PhD (Head/ Vorsitz),
Institute of Geosciences, University of Potsdam, Germany
Prof. Dr. Max Wilke,
Institute of Geosciences, University of Potsdam, Germany

Für meine Mutter,
die mich in jeglicher Lebenslage
liebevoll unterstützt hat.

"If we remove metals from the service of man, all methods of protecting and sustaining health and more carefully preserving the course of life are done away with. If there were no metals, men would pass a horrible and wretched existence in the midst of wild beasts; they would return to the acorns and fruits and berries of the forest. They would feed upon the herbs and roots which they plucked up with their nails. They would dig out caves in which to lie down at night, and by day they would rove in the woods and plains at random like beasts, …"

„Wenn wir die Metalle aus dem Dienst des Menschen entfernen, werden alle Maßnahmen zum Schutz und zur Erhaltung der Gesundheit und zur sorgfältigeren Aufrechterhaltung des Lebens mit ihnen verschwinden. Gäbe es keine Metalle, würden die Menschen ein schreckliches und elendes Dasein inmitten von wilden Tieren fristen; sie würden zu den Eicheln und Früchten und Beeren des Waldes zurückkehren. Sie würden sich von den Kräutern und Wurzeln ernähren, die sie mit ihren Fingernägeln ausrissen. Sie gruben sich Höhlen, in denen sie sich nachts hinlegten, und tagsüber streiften sie wie wilde Tiere in den Wäldern und Ebenen umher …"

Georgius Agricola, De Re Metallica, 1556

"There was a house in a field on the side of a cliff
And the waves crashing below were just said to be a myth
So they ignored the warnings from the ships in the docks
Now the house on the cliff is the wreckage on the rocks"

„Es war einmal ein Haus auf einem Feld am Rande einer Klippe
Und die Wellen, die da drunter tobten, galten als reiner Mythos
Also ignorierten sie die Warnungen der Schiffe in den Häfen
Jetzt ist das Haus an der Klippe das Wrack auf den Felsen"

Enter Shikari, 2012

Declaration of authorship

I hereby confirm that the thesis entitled "Magmatic-Hydrothermal Processes along the Porphyry to Epithermal Transition" I am submitting is entirely my own original work without use of others than the indicated sources. I am aware of the University's regulations concerning plagiarism, including those regulations concerning disciplinary actions that may result from plagiarism. Any use of the works of any other author, in any form, is properly acknowledged in the "preface". I further declare that I have not submitted this thesis at any other institution in order to obtain a degree. This work was accomplished during the PhD candidature at the University of Potsdam.

Date, Signature:

_____

Potsdam, 12.05.2023, Malte Stoltnow

x

Acknowledgements

Abstract

Magmatic-hydrothermal systems form a variety of ore deposits at different proximities to upper-crustal hydrous magma chambers, ranging from greisenization in the roof zone of the intrusion, porphyry mineralization at intermediate depths to epithermal vein deposits near the surface. The physical transport processes and chemical precipitation mechanisms vary between deposit types and are often still debated.

The majority of magmatic-hydrothermal ore deposits are located along the Pacific Ring of Fire, whose eastern part is characterized by the Mesozoic to Cenozoic orogenic belts of the western North and South Americas, namely the American Cordillera. Major magmatic-hydrothermal ore deposits along the American Cordillera include (i) porphyry Cu(-Mo-Au) deposits (along the western cordilleras of Mexico, the western U.S., Canada, Chile, Peru, and Argentina); (ii) Climax- (and sub−) type Mo deposits (Colorado Mineral Belt and northern New Mexico); and (iii) porphyry and IS-type epithermal Sn(-W-Ag) deposits of the Central Andean Tin Belt (Bolivia, Peru and northern Argentina).

The individual studies presented in this thesis primarily focus on the formation of different styles of mineralization located at different proximities to the intrusion in magmatic-hydrothermal systems along the American Cordillera. This includes (i) two individual geochemical studies on the Sweet Home Mine in the Colorado Mineral Belt (potential endmember of peripheral Climax-type mineralization); (ii) one numerical modeling study setup in a generic porphyry Cu-environment; and (iii) a numerical modeling study on the Central Andean Tin Belt-type Pirquitas Mine in NW Argentina.

Microthermometric data of fluid inclusions trapped in greisen quartz and fluorite from the Sweet Home Mine (Detroit City Portal) suggest that the early-stage mineralization precipitated from low- to medium-salinity (1.5-11.5 wt.% equiv. NaCl), CO_2-bearing fluids at temperatures between 360 and 415°C and at depths of at least 3.5 km. Stable isotope and noble gas isotope data indicate that greisen formation and base metal mineralization at the Sweet Home Mine was related to fluids of different origins. Early magmatic fluids were the principal source for mantle-derived volatiles (CO_2, H_2S/SO_2, noble gases), which subsequently mixed with significant amounts of heated meteoric water. Mixing of magmatic fluids with meteoric water is constrained by δ^2H_w-$\delta^{18}O_w$ relationships of fluid inclusions. The deep hydrothermal mineralization at the Sweet Home Mine shows features similar to deep hydrothermal vein mineralization at Climax-type Mo deposits or on their periphery. This suggests that fluid migration and the deposition of ore and gangue minerals in the Sweet Home Mine was triggered by a deep-seated magmatic intrusion.

The second study on the Sweet Home Mine presents Re-Os molybdenite ages of 65.86±0.30 Ma from a Mo-mineralized major normal fault, namely the Contact Structure, and multimineral Rb-Sr isochron ages of 26.26±0.38 Ma and 25.3±3.0 Ma from gangue minerals in greisen assemblages. The age data imply that mineralization at the Sweet Home Mine formed in two separate events: Late Cretaceous (Laramide-related) and Oligocene (Rio Grande Rift-related). Thus, the age of Mo mineralization at the Sweet Home Mine clearly predates that of the Oligocene Climax-type deposits elsewhere in the Colorado Mineral Belt. The Re-Os and Rb-Sr ages also constrain the age of the latest deformation along the Contact Structure to between 62.77±0.50 Ma and 26.26±0.38 Ma, which was employed and/or crosscut by Late Cretaceous and Oligocene fluids. Along the Contact Structure Late Cretaceous molybdenite is spatially associated with Oligocene minerals in the same vein system, a feature that precludes molybdenite recrystallization or reprecipitation by Oligocene ore fluids.

Ore precipitation in porphyry copper systems is generally characterized by metal zoning (Cu-Mo to Zn-Pb-Ag), which is suggested to be variably related to solubility decreases during fluid cooling, fluid-rock interactions, partitioning during fluid phase separation and mixing with external fluids. The numerical modeling study setup in a generic porphyry Cu-environment presents new advances of a numerical process model by considering published constraints on the temperature- and salinity-dependent solubility of Cu, Pb and Zn in the ore fluid. This study investigates the roles of vapor-brine separation, halite saturation, initial metal contents, fluid mixing, and remobilization as first-order controls of the physical hydrology on ore formation. The results show that the magmatic vapor and brine phases ascend with different residence times but as miscible fluid mixtures, with salinity increases generating metal-undersaturated bulk fluids. The release rates of magmatic fluids affect the location of the thermohaline fronts, leading to contrasting mechanisms for ore precipitation: higher rates result in halite saturation without significant metal zoning, lower rates produce zoned ore shells due to mixing with meteoric water. Varying metal contents can affect the order of the final metal precipitation sequence. Redissolution of precipitated metals results in zoned ore shell patterns in more peripheral locations and also decouples halite saturation from ore precipitation.

The epithermal Pirquitas Sn-Ag-Pb-Zn mine in NW Argentina is hosted in a domain of metamorphosed sediments without geological evidence for volcanic activity within a distance of about 10 km from the deposit. However, recent geochemical studies of ore-stage fluid inclusions indicate a significant contribution of magmatic volatiles. This study tested different formation models by applying an existing numerical process model for porphyry-epithermal systems with a magmatic intrusion located either at a distance of about 10 km underneath the nearest active volcano or hidden underneath the deposit. The results show that the migration of the ore fluid over a 10-km distance results in metal precipitation by cooling before the deposit site is reached. In contrast, simulations with a hidden magmatic intrusion beneath the Pirquitas deposit are in line with field observations, which include mineralized hydrothermal breccias in the deposit area.

Zusammenfassung

Magmatisch-hydrothermale Systeme bilden eine Vielzahl von Erzlagerstätten in unterschiedlicher Entfernung zu wasserhaltigen Magmakammern in der oberen Erdkruste, von der Greisenbildung in der Dachzone der Intrusion über die Porphyrmineralisierung in mittleren Tiefen bis hin zu epithermalen Ganglagerstätten nahe der Erdoberfläche. Die physikalischen Transportprozesse und chemischen Ausfällungsmechanismen variieren zwischen den verschiedenen Lagerstättentypen und werden immer noch häufig diskutiert.

Die meisten magmatisch-hydrothermalen Erzlagerstätten befinden sich entlang des Pazifischen Feuerrings, dessen östlicher Teil durch die mesozoischen bis känozoischen orogenen Gürtel des westlichen Nord- und Südamerikas, zusammen die Amerikanische Kordillere, vertreten ist. Zu den wichtigsten magmatisch-hydrothermalen Erzlagerstätten entlang der Amerikanischen Kordillere gehören (i) Cu(-Mo-Au)-Porphyrlagerstätten (entlang der westlichen Kordilleren Mexikos, der westlichen USA, Kanadas, Chiles, Perus und Argentiniens); (ii) Mo-Lagerstätten vom Climax- (und Sub-)Typ (Colorado Mineral Belt und nördliches New Mexico); und (iii) porphyrische und epithermale Sn(-W-Ag)-Lagerstätten vom IS-Typ des Zentralandinen-Zinngürtels (Bolivien, Peru und Nordargentinien).

Die einzelnen Studien dieser Arbeit konzentrieren sich in erster Linie auf die Bildung verschiedener Vererzungsstypen, die sich in unterschiedlicher Entfernung zur Intrusion in magmatisch-hydrothermalen Systemen entlang der amerikanischen Kordillere befinden. Dazu gehören (i) zwei geochemische Einzelstudien über die Sweet Home-Mine im Colorado Mineral Belt (potenzielles Endglied der peripheren Mineralisierung des Climax-Typs); (ii) eine numerische Modellierungsstudie in einem generischen Cu-Porphyr-Setup; und (iii) eine numerische Modellierungsstudie über die Pirquitas-Mine des Zentralandinen-Zinn-Typs in Nordwest-Argentinien.

Mikrothermometrische Daten von Fluideinschlüssen, die in Greisenquarz und -fluorit aus der Sweet Home-Mine (Detroit City Portal) eingeschlossen sind, deuten darauf hin, dass die Mineralisierung im Frühstadium aus CO_2-haltigen Fluiden mit niedrigem bis mittlerem Salzgehalt (1,5-11,5 Gew.-% NaCl-Äquivalent) bei Temperaturen zwischen 360 und 415 °C und in einer Tiefe von mindestens 3,5 km ausgefällt wurde. Daten zu stabilen Isotopen und Edelgasisotopen zeigen, dass die Greisenbildung und die Buntmetallvererzung in der Sweet Home-Mine mit Fluiden unterschiedlichen Ursprungs in Verbindung stehen. Frühe magmatische Fluide waren die Hauptquelle für aus dem Mantel stammende Volatile (CO_2, H_2S/SO_2, Edelgase), die sich anschließend mit erheblichen Mengen erhitzten meteorischen Wassers vermischten. Die Vermischung von magmatischen Fluiden mit meteorischem Wasser wird durch die Zusammenhänge von δ^2H_w-$\delta^{18}O_w$ der Fluideinschlüsse belegt. Die tiefe hydrothermale Vererzung in der Sweet Home-Mine weist ähnliche Merkmale auf wie die tiefe hydrothermale Gangvererzung in Mo-Lagerstätten vom Climax-Typ oder in deren Peripherie. Dies deutet darauf hin, dass die Fluidmigration und die Ausfällung von Erz und Gangmineralen in der Sweet Home-Mine durch eine tief sitzende magmatische Intrusion angeregt wurde.

Die zweite Studie über die Sweet Home Mine präsentiert ein Re-Os-Molybdänit-Alter von 65,86±0,30 Ma aus einer Mo-vererzten Abschiebung, namentlich der Contact Structure, und ein multimineralisches Rb-Sr-Isochronen-Alter von 26,26±0,38 Ma und 25,3±3,0 Ma von Gangmineralen in Greisenvergesellschaftungen. Die Altersdaten deuten darauf hin, dass die Vererzungen in der Sweet Home Mine während zweier separater Ereignisse entstand: In der späten Kreidezeit (im Zusammenhang mit der Laramidischen Orogenese) und im Oligozän (im

Zusammenhang mit dem Rio Grande Rift). Das Alter der Mo-Vererzung in der Sweet Home Mine liegt demnach eindeutig vor dem der oligozänen Climax-Lagerstätten anderswo im Colorado Mineral Belt. Die Re-Os- und Rb-Sr-Alter grenzen auch das Alter der jüngsten Deformation entlang der Contact Structure, die von spätkreidezeitlichen und oligozänen Fluiden genutzt und/oder geschnitten wurde, auf 62,77±0,50 Ma und 26,26±0,38 Ma ein. Entlang der Contact Structure ist spätkreidezeitlicher Molybdänit räumlich mit Mineralen aus dem Oligozän in demselben Gangsystem vergesellschaftet, was eine Rekristallisierung oder Ausfällung von Molybdänit durch oligozäne Fluide ausschließt.

Die Erzausfällung in porphyrischen Kupfersystemen ist im Allgemeinen durch eine Metallzonierung (Cu-Mo bis Zn-Pb-Ag) gekennzeichnet, die vermutlich mit der Abnahme der Löslichkeit während der Fluidabkühlung, den Wechselwirkungen zwischen Fluid und Gestein, der Partitionierung während der Phasenseparation des Fluids und der Mischung mit externen Fluiden in Zusammenhang steht. Die numerische Modellierung, die in einer generischen Porphyr-Cu-Umgebung durchgeführt wurde, stellt neue Fortschritte eines numerischen Prozessmodells dar, indem sie veröffentlichte Randbedingungen für die temperatur- und salinitätsabhängige Löslichkeit von Cu, Pb und Zn im Erzfluid berücksichtigt. Diese Studie untersucht die Rolle der Dampf-Sole-Separation, der Halitsättigung, des anfänglichen Metallgehalts, der Fluidmischung und der Remobilisierung als Einflussfaktoren erster Ordnung der physikalischen Hydrologie auf die Erzbildung. Die Ergebnisse zeigen, dass die magmatischen Dampf- und Solephasen mit unterschiedlichen Verweilzeiten, aber als mischbare Fluide aufsteigen, wobei eine Erhöhung des Salzgehalts zu einem metall-ungesättigten Gesamtfluid führt. Die Freisetzungsraten der magmatischen Fluide wirken sich auf die Lage der thermohalinen Fronten aus, was zu widersprüchlichen Mechanismen für die Erzausfällung führt: Höhere Raten führen zu einer Halitsättigung ohne signifikante Metallzonierung, niedrigere Raten erzeugen zonierte Erzschalen aufgrund der Mischung mit meteorischem Wasser. Unterschiedliche Metallgehalte können sich auf die Reihenfolge der endgültigen Metallausfällung auswirken. Die Wiederauflösung bereits ausgefällter Metalle führt zu zonierten Erzschalenmustern in periphereren Bereichen und entkoppelt auch die Halitsättigung von der Erzausfällung.

Die epithermale Pirquitas Sn-Ag-Pb-Zn-Mine im Nordwesten Argentiniens befindet sich in einem Bereich metamorphisierter Sedimente ohne geologische Hinweise auf vulkanische Aktivitäten in einer Entfernung von etwa 10 km zur Lagerstätte. Jüngste geochemische Untersuchungen von Fluideinschlüssen im Erzstadium deuten jedoch auf einen bedeutenden Beitrag von magmatischen Volatilen hin. In dieser Studie wurden verschiedene Entstehungsmodelle getestet, indem ein bestehendes numerisches Prozessmodell für porphyrisch-epithermale Systeme mit einer magmatischen Intrusion angewandt wurde, die sich entweder in einer Entfernung von etwa 10 km unterhalb des nächstgelegenen aktiven Vulkans oder verborgen unterhalb der Lagerstätte befindet. Die Ergebnisse zeigen, dass die Migration der Erzflüssigkeit über eine Entfernung von 10 km zu einer Metallausfällung durch Abkühlung führt, bevor die Lagerstätte erreicht wird. Im Gegensatz dazu stimmen die Simulationen mit einer verborgenen magmatischen Intrusion unter der Pirquitas-Lagerstätte mit den Feldbeobachtungen überein, die mineralisierte hydrothermale Brekzien im Lagerstättenbereich umfassen.

Preface

This thesis entitled *"Magmatic-Hydrothermal Processes along the Porphyry to Epithermal Transition"* is comprised of six chapters, which all individually concern processes along the transition from rather deep porphyry to rather shallow epithermal mineralization. Chapters 2, 3, and 4 are designed to serve as independent publications and chapter 5 as peer-reviewed extended abstract; therefore, introductory information may be restated in the individual chapters. This preface includes a brief summary for each chapter and a statement of the personal contribution made by the author, co-authors and others who contributed to the individual chapters.

Chapter 1 provides the reader with a general introduction to magmatic-hydrothermal systems, the various ore deposits that may occur in this setting, and their characteristics and relevance to the American Cordillera. In addition, this chapter introduces the study areas and their possible location along the porphyry-epithermal transition. Finally, the reader is presented with the research focus and motivation of this thesis as well as the methods used to address the research questions.

Chapter 2: *"A geochemical study of the Sweet Home mine, Colorado Mineral Belt, USA: Formation of deep hydrothermal vein-type molybdenum greisen and base metal mineralization"* has been published in *Mineralium Deposita* with V. Lüders, S. de Graaf, and S. Niedermann as co-authors. This chapter shows the importance of conventional fluid inclusion microthermometry as well as more sophisticated analytic approaches, including fluid inclusion stable and noble gas isotopes, to decipher the evolution of the fluid system, which formed the Sweet Home Mine.

The samples were provided by D. Misantoni (chief geologist at the Sweet Home Mine, owned by The Collector's Edge Minerals Inc.). Petrographic observations and sample selection were carried out by the author supported by discussions with V. Lüders and P. Weis. Thin section and mount preparation were carried out by C. Fischer at the University of Potsdam, U. Dittmann at GFZ Potsdam, and the author. Fluid inclusion microthermometry and Laser Raman spectroscopy was done by the author with technical guidance from V. Lüders, M. Sosnicka, and M. Korges at GFZ Potsdam. Cathodoluminescence (CL) petrography was carried out by the author with technical guidance from C. Kusebauch. Hydrogen and oxygen isotope analysis of fluid inclusions and carbon and oxygen isotopic compositions of rhodochrosite were analyzed by S. de Graaf at the Vrije Universiteit Amsterdam (Netherlands) and at the Max Planck Institute for Chemistry (Mainz). Carbon and nitrogen isotopic compositions of fluid inclusions were analyzed by V. Lüders at GFZ Potsdam. Noble gas analyses of fluid inclusions were carried out by E. Schnabel in the laboratory of S. Niedermann at GFZ Potsdam. Sulfur isotopic compositions of sulfides and sulfosalts were measured by H. Strauß at the University of Münster. Data processing and interpretation was carried out by the author in collaboration with V. Lüders, S. de Graaf, and S. Niedermann.

Chapter 3: *"The role of the Laramide orogeny in the formation of Climax-type molybdenite mineralization: constraints from Re-Os and Rb-Sr isotope systematics"* has been prepared for submission in *Mineralium Deposita* with R. L. Romer, J. Glodny, Michael Brauns, and J. M. Kärstens as co-authors. This chapter presents Late Cretaceous Re-Os molybdenite ages and Oligocene multimineral Rb-Sr isochron ages for gangue minerals from Sweet Home mineral assemblages. These age data imply that the mineralization at the SHM formed by two separate, unrelated events: Laramide-related and Rio Grande Rift-related.

The samples were provided by D. Misantoni. Petrographic observations and sample selection were carried out by the author and J. M. Kärstens supported by discussions with R. L.

Romer, J. Glodny and V. Lüders. Thin section and mount preparation were carried out by C. Fischer and J. M. Kärstens at the University of Potsdam. Sample preparation for radiogenic isotope analyses, including elaborate mechanical and heavy liquid mineral separation, and mineral dissolution techniques, were performed by J. Glodny, R. L. Romer, M. Brauns, and the author. Radiogenic isotope ratios were measured by J. Glodny (Rb-Sr), R. L. Romer (Rb-Sr), M. Brauns (Re-Os), and the author (Rb-Sr).

The appendix of this chapter furthermore contains EPMA data of ore minerals from the Sweet Home Mine analyzed by J. M. Kärstens during his Master thesis guided by P. Weis and V. Lüders, and the author. Data processing and interpretation was carried out by the author in collaboration with R. L. Romer, J. Glodny, and M. Brauns. R. L. Romer and J. Glodny supported the author with scientific discussions and guidance, as well as with editing of the manuscript.

Chapter 4: *"Hydrological controls on base metal precipitation and zoning at the porphyry-epithermal transition constrained by numerical modeling"* has been published in *Scientific Reports* with P. Weis and M. Korges. This chapter presents constrains for the role of phase separation and fluid mixing on precipitation mechanisms and zoning of base metals in porphyry Cu systems by numerical modeling. The simulations consider base metal transport, precipitation, and remobilization using published metal solubilities as a function of fluid temperature and salinity.

New functionalities added in the CSMP++ code were written by P. Weis and supported by M. Korges, and the author. P. Weis also edited other parts of the code for this specific setup. Temperature- and salinity-dependent solubility parametrizations were derived by M. Korges for data supplied by K. Kouzmanov and G. Pokrovski. The author has designed and set up the simulation scenarios in the CSMP++ environment. Data evaluation and interpretation was carried out by the author in collaboration with P. Weis and M. Korges. The author has created the figures and written the manuscript, the latter was edited by the author and co-authors.

Chapter 5: *"Numerical constraints on the magmatic-hydrothermal fluid evolution forming the Pirquitas Sn-Ag-Pb-Zn deposit in NW Argentina"* has been submitted as a peer-reviewed extended abstract for presentation at the *17th SGA Biennial Meeting* in Zurich (Switzerland) with P. Weis and M. Korges. In this chapter we tested different formation models of the Pirquitas Sn-Ag-Pb-Zn mine in NW Argentina by applying an existing numerical process model for porphyry-epithermal systems with a magmatic intrusion located either at a distance of about 10 km underneath the nearest active volcano or hidden underneath the deposit.

P. Weis edited the code in the CSMP++ environment for the numerical simulations of the Pirquitas mineral system. The author has created the geometry for, and set up the, simulation runs in the CSMP++ environment, using published geological constraints from Pirquitas. Data evaluation and interpretation was carried out by the author, P. Weis, and M. Korges. The author has created the figures and written this chapter, the latter was edited by P. Weis and M. Korges.

Chapter 6 provides the reader with overall conclusions of this thesis emphasizing the fluid origin and evolution, dating, and numerical modeling of ore-forming processes in magmatic-hydrothermal systems, and the position of the studied mineralization along the porphyry-epithermal transition. Finally, this chapter provides an outlook on themes of future research related to the individual chapters.

Appendix: Among figures and tables, which have not been considered for the main text, the appendix further includes the report *"Constraining the magmatic-hydrothermal fluid evolution from proximal to distal settings forming Sn-Ag-Pb-Zn deposits in NW Argentina"* addressing the original NW-Argentina-related layout of this PhD thesis, why early plans had to be paused due to the COVID19 pandemic, and what has been done already and could be done for a successful completion.

Contents

Figures and tables

1 Introduction

The Earth's continental crust is made of ~99.6% of O, Si, Al, Fe, Ca, Mg, K, Ti, and H (Rudnick and Gao 2003). This means that most industrially significant elements are part of the remaining 0.4%. In this sense, elements, such as Cu, Mo, Sn, Au, Ag, Pb, and Zn, can be considered scarce, and yet they are found enriched in certain places on this planet. When they can be mined economically, they are called ore deposits (Skinner 1997). Kesler (1994) illustrated three principal processes involved in selective element enrichment and formation of ore deposits, which are: (i) sedimentary/surficial processes; (ii) igneous processes; and (iii) hydrothermal processes, the latter including, given the presence of magmatic volatiles, magmatic-hydrothermal processes.

1.1 Characteristics of magmatic-hydrothermal systems

Magmatic-hydrothermal systems can host various deposit types, whose mineralization styles depend on their distance to, and the composition of, the associated intrusion(s), and the composition of host rocks the ore fluids may interact with (e.g., Hedenquist and Lowenstern 1994; Giggenbach 1997). Typical examples of these ore deposits are greisen deposits in the roof zone of the intrusion, porphyry mineralization at intermediate depths, proximal and distal skarn as well as carbonate-replacement ore deposits, and high-, intermediate-, and low-sulfidation (sub−)epithermal vein deposits in shallower crustal domains (Fig. 1) (e.g., Sillitoe 2010).

It is generally agreed that magmatic-hydrothermal systems are initiated by the emplacement of magma in the upper crust (5-15 km), which is derived from large underlying magma reservoirs and is saturated in sulfur and metal-rich aqueous fluids (Fig. 1) (e.g., Burnham 1979; Hedenquist and Lowenstern 1994; Richards 2003). Depending on the parental magma composition and depth of fluid exsolution, the primary magmatic fluid may be enriched in certain metals, which are transported as metal-ligand complexes (e.g., with Cl^-, HS^-, OH^-), and significant amounts of CO_2, with minor other volatiles, such as SO_2/H_2S, H_2, N_2, and noble gases (Candela 1989; Giggenbach 1992; Hedenquist 1995; Giggenbach 1997).

Porphyry Cu mineralization is predominantly formed at relatively shallow depths (~4 km) related to two-phase fluids, including a hypersaline liquid (brine) and a low-density vapor phase (Burnham 1979; Fournier 1999; Sillitoe 2010). Early copper precipitation in porphyry systems

has been associated with cooling of the ore fluid from ~700 to 550°C and thereby causing potassic alteration (Fig. 2) (Bodnar 1995; Ulrich and Heinrich 2002). The majority of Cu (and Au) mineralization in porphyry systems, however, is suggested to have formed at fluid temperatures between ~550 to 350°C (e.g., Landtwing et al. 2005; Klemm et al. 2007; Sillitoe 2010). The temporal and spatial position of Mo in primary porphyry mineralization is a topic of debate, which includes, among others, that molybdenum has a longer residence time in the melt and thus tends to precipitate later than Cu (and Au), albeit near the intrusion (Fig. 2) (Candela and Holland 1986).
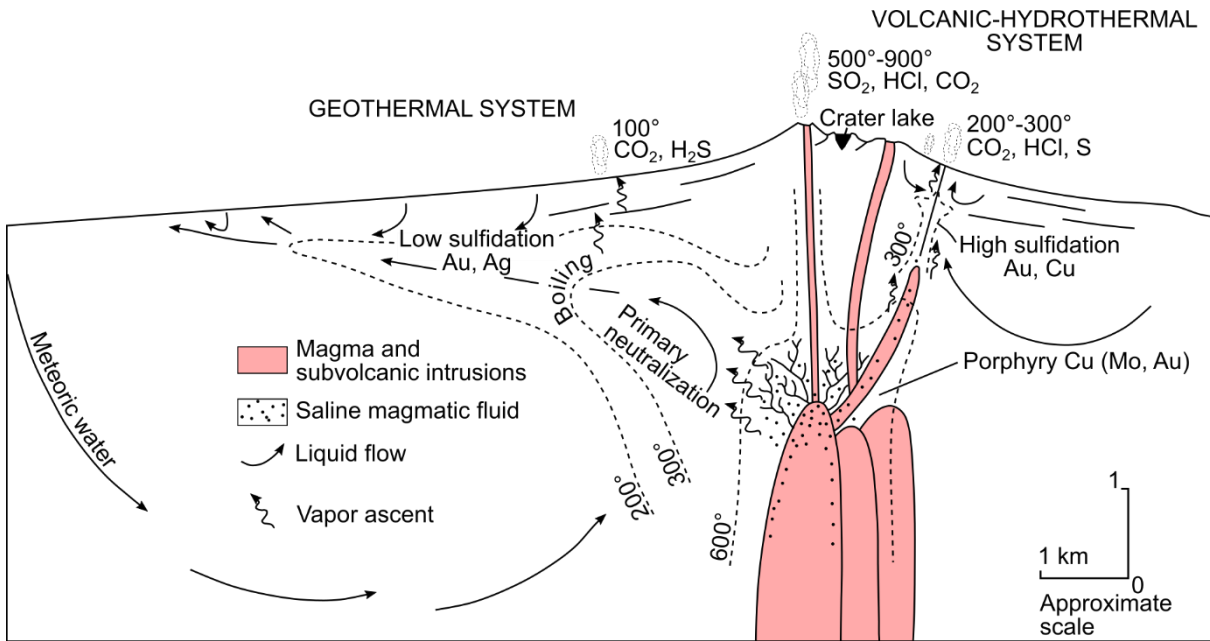
Figure 1 Schematic cross-section of a magmatic-hydrothermal system showing shallow subvolcanic intrusions beneath an associated stratovolcano and the hydrological conditions for the formation of porphyry copper and high- and low-sulfidation epithermal ore deposits. The fluid system extends from degassing magma to fumaroles and acid springs, including pH-neutral water that forms low-sulfidation mineralization and can emerge as hot springs. Modified from Hedenquist and Lowenstern (1994).

The porphyry ore formation is suggested to take place at the transition from lithostatic to hydrostatic pressure conditions and may be accompanied by hydraulic fracturing of the surrounding host rock(s) and the generation of pervasive stockwork veins (Fig. 1) (e.g., Burnham 1979; Sillitoe 2010). During fluid ascent, metal precipitation may be accompanied by pressure decrease, phase separation, cooling, fluid-rock interaction, and mixing with externally-derived fluids (Fig. 1) (e.g., Sheppard et al. 1971; Sillitoe 2010; Cooke et al. 2014). During ore formation the pressure regime may fluctuate between lithostatic and hydrostatic according to either repeating fracture opening and sealing, and/or surface degradation (e.g. caldera collapse) (Ulrich and Heinrich 2002; Klemm et al. 2007; Rusk et al. 2008). This may already induce metal remobilization and reprecipitation.

The decline of the magmatic fluid plume is accompanied by cooling of the system below 400°C, which enables brittle rock fracturing in a hydrostatic-dominant pressure regime and favors

the formation of sericitic±chlorite-sericite alteration zones from a deeply-derived, single-phase fluid (Fig. 2) (Hedenquist et al. 1998; Fournier 1999; Heinrich et al. 2004). Further ascent of the same fluid to the advanced argillic lithocap area may favor the formation of high-sulfidation (HS) Au-Cu epithermal mineralization (Figs. 1, 2) and under neutralization outside the lithocap, intermediate-sulfidation (IS) (Fig. 1) (Hedenquist et al. 1998; Heinrich 2005; Sillitoe and Hedenquist 2005).
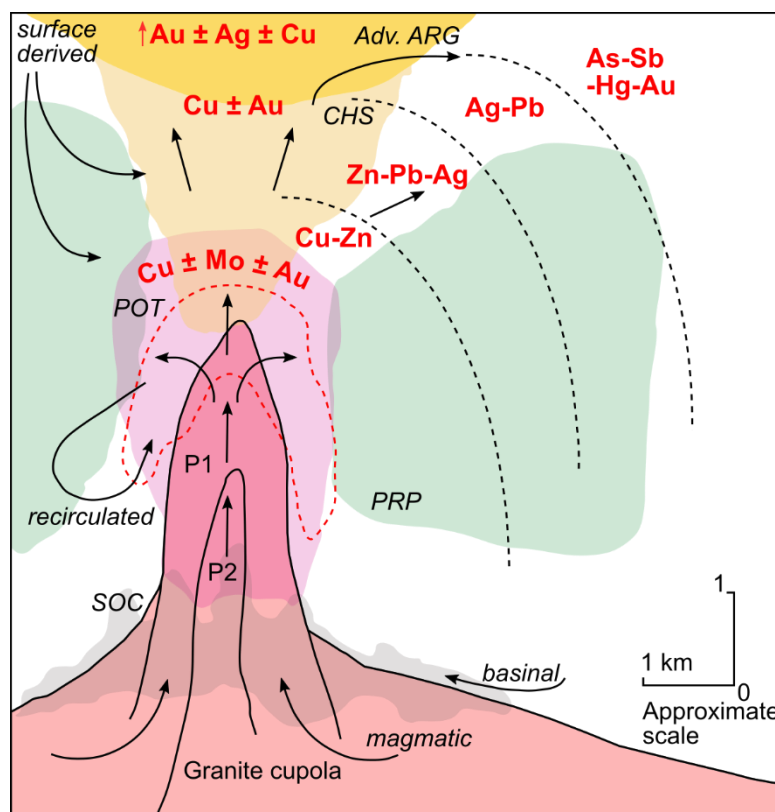
Figure 2 Generalized scheme of metal zonation, alteration patterns, and fluid pathways in a porphyry-centered system. The Cu±Au±Mo ore shell is centered above and surrounding the porphyry intrusion and extends to the wall rocks. The outer base metal zone includes, in order of increasing distance from the porphyry: Cu-Zn, Zn-Pb-Ag, Pb-Ag and As-Sb-Hg-Au zones (see Fig. 1 for associated deposit types). High-sulfidation epithermal mineralization may form in the upflow zone above the porphyry center. During the evolution of the magmatic-hydrothermal system, primary magmatic fluids may mix with fluids of non-magmatic origin, such as meteoric water, or with recycled magmatic fluids. P1 = porphyry 1, P2 = porphyry 2, *SOC* = sodic-calcic alteration, *PRP* = propylitic alteration, *POT* = potassic alteration, *CHS* = chlorite-sericite alteration, *Adv. ARG* = advanced argillic alteration, arrows indicate fluid flow. Modified from Kouzmanov and Pokrovski (2012).

During the evolution of the hydrothermal system, the incursion of meteoric water may cause propylitic alteration peripheral to the intrusion and at moderate temperatures (200-300°C; Fig. 2) (Hemley et al. 1967). The heat derived from the underlying intrusion is suggested to trigger the circulation of meteoric water through the permeable crust (Cathles 1977). When this circulating water gets in contact with the metal-enriched hypersaline liquid, fluid cooling and neutralization may cause a rapid increase in metal saturation and thus precipitation of Zn, Pb, Ag (and Mn) in the propylitic halo (Figs. 1, 2) (Hemley and Hunt 1992).

In the most distal and shallowest parts, low-sulfidation (LS) Au (-Ag) epithermal mineralization is suggested to have formed from the interaction of the low-density vapor with significant amounts of meteoric water in a pH-neutral, low-salinity, and low-temperature (50-200°C; Fig. 1) (e.g., Hedenquist and Lowenstern 1994).

Figure 2 shows a generalized zonation pattern of precipitated metals in a porphyry-centered environment. Whereas Cu-Au-Mo ore shells are centered on the porphyry intrusion, high sulfidation Cu-Au mineralization might be formed in the upflow zone over the porphyry center. Outward base metal zonation peripheral to the intrusion and into epithermal environments is characterized by the precipitation of Cu-Pb-Zn-Ag (and As-Sb-Hg-Au in the most distal areas) and its style depends on changes in fluid compositions as well as metal transport and precipitation mechanisms (e.g., Kouzmanov and Pokrovski 2012).

Due to its low density, the voluminous vapor phase rises and can cause several features: (i) it may cause co-precipitation of Cu and Au in shallower settings due to decompression (Fig. 2); (ii) it condenses into ground water generating extremely low pH and causes mostly barren advanced argillic alteration (Fig. 2); and (iii) it may be discharged at the surface as fumaroles (Fig. 1) (Giggenbach 1992; Hedenquist and Lowenstern 1994; Fournier 1999; Williams-Jones and Heinrich 2005; Monecke et al. 2018; Schirra et al. 2022).

1.2 Magmatic-hydrothermal systems along the American Cordillera

The majority of magmatic-hydrothermal ore deposits are located along the Pacific Ring of Fire, which is characterized by active subduction zones (Sinclair 2007). The eastern part of the ring includes the Mesozoic to Cenozoic orogenic belts of the western North and South Americas (American Cordillera) (Fig. 3). The major ore deposit type along the American Cordillera is the porphyry type (with related HS-, IS-, LS-, and Cordilleran-epithermal mineralization), which can be subdivided into (i) porphyry Cu(-Mo-Au) deposits predominantly located in the Basin and Range province of Mexico and the western U.S. and extending into Canada, and by the Coastal Areas and Western Cordillera of Chile, Peru, and Argentina (Fig. 3) (e.g., Singer 1995; Mlynarczyk and Williams-Jones 2005; Singer et al. 2008; Fontboté 2018); (ii) porphyry Mo deposits of the Climax- (and sub−) type predominantly hosted by the Colorado Mineral Belt and northern New Mexico in the eastern Rocky Mountains (Fig. 3) (Wallace 1995); and (iii) porphyry and IS-type epithermal Sn(-W-Ag) deposits predominantly hosted by the Central Andean Tin Belt (CATB) in

Bolivia, Peru and northern Argentina (Fig. 3) (Turneaure 1971; Sillitoe et al. 1975; Fontboté 2018).
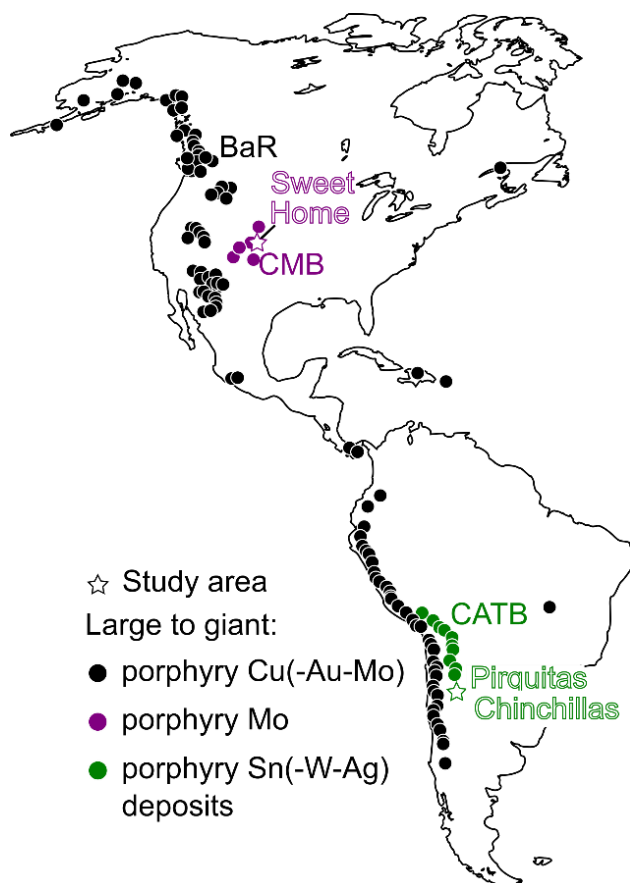
Figure 3 Overview map showing the major ore provinces and the location of large to giant magmatic-hydrothermal Cu, Mo, and Sn deposits along the American Cordillera. Data from Singer (1995), Wallace (1995), Mlynarczyk and Williams-Jones (2005), Singer et al. (2008), and Fontboté (2018).

Major differences in the mineralization style of the porphyry deposits may be attributed to the differences in the tectonomagmatic settings. In general, (i) porphyry Cu deposits are related to calc-alkaline-alkaline arc magmatism from subduction zones (e.g., Sillitoe 2010); (ii) porphyry Mo deposits, i.e. of the Climax type, are related to a continental extensional setting, which is characterized by intrusions of high-silica, high-fluorine rhyolitic, and locally occurring mantle melts (e.g., Audétat and Li 2017), and (iii) porphyry Sn and epithermal varieties in the CATB are related to melting of passive margin sedimentary rocks by peraluminous granitic magmatism during flat-slab subduction (e.g., Fontboté 2018).

1.3 Significance of the porphyry-epithermal transition

Among magmatic-hydrothermal systems, porphyry deposits, located rather proximal to the intrusion, are the economically most relevant (e.g., Hedenquist and Lowenstern 1994; Sinclair 2007). However, the full range of possibly occurring intrusion-related deposits in an individual district (as described above) is rarely developed, partly eroded, or still buried. In some cases, only lithocaps are exposed, in others sub-economic veins. However, recognizing even weakly developed mineralization of a single type can contribute to exploration for potentially economic mineralization elsewhere in the system (Sillitoe 2010). In general, as discoveries of near-surface

mineral deposits have diminished over the past few decades, the importance of constraining genetic models is growing to explore deeper, currently hidden deposits to meet future metal demand (Schodde 2017).

The individual studies presented in this thesis primarily focus on the formation of different styles of mineralization located at different proximities to the intrusion in magmatic-hydrothermal systems along the American Cordillera. This includes (i) two individual geochemical studies on the Sweet Home mine in the Colorado Mineral Belt (USA), which is suggested to be an endmember of peripheral Climax-type Mo porphyry mineralization (Fig. 3) (Misantoni et al. 1998; Lüders et al. 2009); (ii) one numerical modeling study setup in a generic porphyry Cu-environment; and (iii) a numerical modeling study on the Pirquitas mine in NW Argentina (Fig. 3), which has been related to Miocene CATB-mineralization, however, without direct association to Miocene magmatism (Malvicini 1978; Desanois et al. 2019).

1.4 Potential of the study areas with respect to future economic discoveries

The (Mo-)W-Pb-Zn-Ag-rhodochrosite mineralization found at Sweet Home mine in the Colorado Mineral Belt (USA) has been related to peripheral mineralization of Climax-type porphyry Mo deposits (Misantoni et al. 1998; Lüders et al. 2009). Whereas Climax-type deposits are located above felsic porphyry intrusions, the Sweet Home mine lacks a direct magmatic link, however, the existence of a hypothesized deeper-seated porphyry intrusion feeding the Sweet Home mineral system has been proposed (Lüders et al. 2009). Constraining the magmatic-hydrothermal system, which formed the Sweet Home mine by applying geochemical techniques, may provide new insights into the location of the intrusion and thus potential higher-grade mineralization.

The Sn-Ag-Pb-Zn Pirquitas Mine is suggested to be the southernmost of the Sn-Ag-polymetallic IS-type mineral deposits of the CATB (Fig. 3) (e.g., Malvicini 1978; Paar et al. 2000; Desanois et al. 2019; Passamani et al. 2020). However, while the Bolivian deposits of the CATB have a clear association with Miocene magmatism (e.g., Grant et al. 1979), Pirquitas lacks a direct connection to magmatic intrusions so far. Contrasting formation models of the Pirquitas deposit include the origins of the ore-forming fluid both from a magmatic intrusion at a distance of at least 10 km or directly beneath/ adjacent to the mineralization (Desanois et al. 2019; Passamani et al. 2020; Slater et al. 2021). Numerical simulations testing the impact of different locations of the

magmatic intrusion on the hydrology may identify the mineralization-related intrusion, if existing, and therefore the location of other potential high-grade mineralizations.

1.5 Thesis objectives and methods

This thesis has three main objectives to gain a more thorough knowledge of processes along the porphyry to epithermal transition in order to draw conclusions about the potential existence and location of high-grade mineralization elsewhere in the fluid system: These are (1) to constrain the fluid origin and evolution in magmatic-hydrothermal systems performing various (fluid inclusion) geochemical techniques and to quantify the processes accompanying the fluid evolution via (2) mineral geochronology and (3) numerical modeling.

(1) The first geochemical study of the Sweet Home Mine aims to decipher the evolution of the magmatic-hydrothermal fluid system that forms the mineralization and find further evidence of a hidden, associated intrusion.

(i) Fluid inclusion microthermometry and laser Raman spectroscopy can provide a constraint on the PVTX (pressure, volume, temperature, composition) parameters of the ore fluid.

(ii) Isotopic analyses of fluid inclusion water (H, O isotopes) and gases (CO_2 and noble gases) may constrain the origin of the ore fluid (e.g., magmatic vs. meteoric, crustal vs. mantle).

(iii) Stable C, O, and S isotope analyses of carbonates and sulfides may constrain the origin of sulfur, carbon, and oxygen (e.g., igneous vs. sedimentary, juvenile vs. crustal).

(2) The second geochemical study aims to constrain the timing of the mineralization and the age of the latest deformation along major structural features found at the Sweet Home Mine.

(iv) Molybdenite Re-Os dating is applied to constrain the origin and age of molybdenite in the Sweet Home Mine to conclude on potential future Mo discoveries.

(v) Rb-Sr geochronology is applied to date gangue minerals of individual mineral assemblages and to support and confirm molybdenite Re-Os age data from the Sweet Home Mine.

(3) Numerical process models presented in this thesis allow the quantification of the dynamic behavior of mass and heat exchange in porphyry systems in a given time frame run on the Complex System Modeling Platform (CSMP++ software). Numerical simulations were set up both for a generic and Pirquitas-related geometry and parametrization.

(vi) The Generic modeling environment was chosen to test code updates and new parametrizations addressing the roles of vapor-brine separation, halite saturation, initial metal contents, fluid mixing, and remobilization as first-order controls of the physical

hydrology on ore formation. The metals Pb and Zn were added to provide a further constraint for the hydrology at the porphyry-epithermal transition.

(vii)   The Pirquitas-related geometry was applied to test different published ore deposit genesis models including the development of a Pirquitas-forming magmatic-hydrothermal system both proximal and distal to the associated intrusion.

The individual studies are presented in Chapters 2, 3, 4, and 5, and followed by the overall conclusions of this thesis and an outlook in Chapter 6. The appendix includes a report on the original work plan on the Pirquitas and Chinchillas deposits, which had to be abandoned during this PhD project due to the COVID19 pandemic.

2 A geochemical study of the Sweet Home mine, Colorado Mineral Belt, USA: formation of deep hydrothermal vein–type molybdenum greisen and base metal mineralization

Stoltnow M.[1,2], Lüders V.[2], de Graaf S.[3], Niedermann S. [2]

[1]Institute of Geosciences, University of Potsdam, Karl-Liebknecht-Straße 24/25, 14476 Potsdam, Germany
[2]GFZ German Research Centre for Geosciences, 14473 Telegrafenberg, Germany
[3]Max Planck Institute for Chemistry, Hahn-Meitner-Weg 1, 55218 Mainz, Germany

Abstract

Deep hydrothermal Mo, W, and base metal mineralization at the Sweet Home mine (Detroit City portal) formed in response to magmatic activity during the Oligocene. Microthermometric data of fluid inclusions trapped in greisen quartz and fluorite suggest that the early-stage mineralization at the Sweet Home mine precipitated from low- to medium-salinity (1.5-11.5 wt.% equiv. NaCl), CO_2-bearing fluids at temperatures between 360 and 415°C and at depths of at least 3.5 km. Stable isotope and noble gas isotope data indicate that greisen formation and base metal mineralization at the Sweet Home mine was related to fluids of different origins. Early magmatic fluids were the principal source for mantle-derived volatiles (CO_2, H_2S/SO_2, noble gases), which subsequently mixed with significant amounts of heated meteoric water. Mixing of magmatic fluids with meteoric water is constrained by δ^2H_w-$\delta^{18}O_w$ relationships of fluid inclusions. The deep hydrothermal mineralization at the Sweet Home mine shows features similar to deep hydrothermal vein mineralization at Climax-type Mo deposits or on their periphery. This suggests that fluid migration and the deposition of ore and gangue minerals in the Sweet Home mine was triggered by a deep-seated magmatic intrusion. The findings of this study are in good agreement with the results of previous fluid inclusion studies of the mineralization of the Sweet Home mine and from Climax-type Mo porphyry deposits in the Colorado Mineral Belt.

2.1 Introduction

The Colorado Mineral Belt (CMB) hosts a number of economic molybdenum porphyry deposits, such as the world-class Climax and Urad-Henderson deposits (Fig. 4). The formation of Climax-type Mo deposits in the CMB is related to the emplacement of highly evolved calc-alkaline granitic and subvolcanic rhyolite porphyry melts (e.g. Wallace 1995; Ludington and Plumlee 2009; Audétat and Li 2017), which are part of bimodal magmatism related to crustal extension during the Mid- to Late Cenozoic (e.g. Lipman and Mehnert 1975; Westra and Keith 1981; White et al. 1981; Bookstrom et al. 1988; Carten et al. 1993; Keith et al. 1993; Russell and Snelson 1994; Ludington and Plumlee 2009; Audétat 2010; Audétat et al. 2011; Mercer et al. 2015).

Climax-type deposits have high Mo and little Cu enrichment. The ore is concentrated in ore shells that consist of stockwork vein and greisen molybdenite–fluorite–quartz–pyrite–topaz–sericite mineralization accompanied by intense host rock alteration (Appendix Fig. 3) (e.g., Audétat and Li 2017 and references therein). The main Mo mineralization occurs at the flanks and apical parts of small porphyry stocks. Multiple intrusions lead to different overlapping ore shells

and individual Climax-type deposits (Wallace et al. 1968; Mutschler et al. 1981; White et al. 1981; Bookstrom 1989; Carten et al. 1993; Wallace 1995; Ludington and Plumlee 2009). Peripheral base metal- and rhodochrosite vein mineralization extends from porphyritic rocks into crystalline country rocks and postdates the Mo mineralization (e.g., Bookstrom 1989; Seedorff and Einaudi 2004a). Molybdenum mineralization is assumed to have formed from magmatic fluids that were expelled from the parental magma at temperatures of 710–750°C and pressures of 2000–3000 bar, as evidenced by studies of melt inclusions (Lowenstern 1994; Audétat 2015; Mercer et al. 2015). Besides Mo, the melts are enriched in W, Pb, Zn, Cu, Bi, Ag, and Mn, as well as in the volatile components H_2O, CO_2, F, and Cl (Lowenstern 1994; Audétat 2015; Mercer et al. 2015).
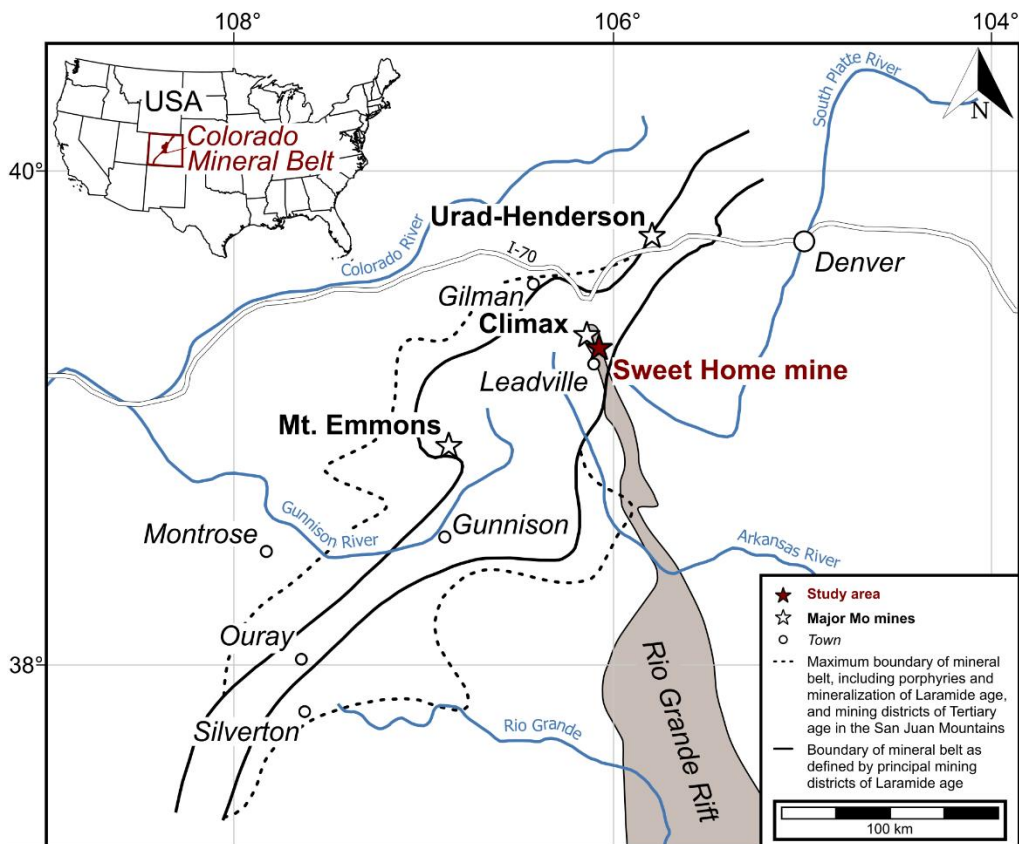
Figure 4 Location of the Sweet Home mine and major Mo deposits in the Colorado mineral belt. Modified after Tweto and Sims (1963) and White et al. (1981).

The change of mineralization style from early quartz-molybdenite stockwork veins to later tungsten-bearing greisen as well as silver- and base metal-bearing assemblages in ore shells and distal veins above the Mo porphyry ore shells likely resulted from simple cooling of the magmatic-hydrothermal fluid (Wallace et al. 1978; Mutschler et al. 1981; Westra and Keith 1981; White et al. 1981; Stein and Hannah 1985; Stein 1988; Bookstrom 1989; Keith et al. 1993; Wallace 1995; Seedorff and Einaudi 2004a; 2004b; Ludington and Plumlee 2009; Audétat 2010; Mercer et al. 2015). A magmatic origin has also been suggested for sulfur, but it is unclear whether sulfur was derived by mantle degassing (e.g. Wallace 1995; Mercer et al. 2015) or directly from the rhyolitic melts (Stein and Hannah 1985; Lowenstern 1994; Audétat 2015).

In contrast, mixing of magmatic and meteoric fluids was suggested for the formation of Climax-type mineralization, based on fluid inclusion studies (Hall et al. 1974; Bloom 1981; Smith 1983; Rowe 2012). Fluid mixing models were also proposed for the formation of distal vein mineralization related to Climax-type porphyry intrusions (Bartos et al. 2007). Lüders et al. (2009) studied the polymetallic vein-type mineralization of the Sweet Home mine (SHM) in Alma, Colorado (Fig. 5). The authors proposed that the mineralization represents the peripheral hydrothermal endmember of a Climax-type porphyry system above an inferred granite cupola (Lüders et al. 2009). Based on fluid inclusions and stable and radiogenic isotope data, they concluded that mineralization at the SHM was formed by mixing of a small proportion of ascending magmatic fluids with larger amounts of externally-derived fluids, which interacted intensively with the country rocks (Lüders et al. 2009).
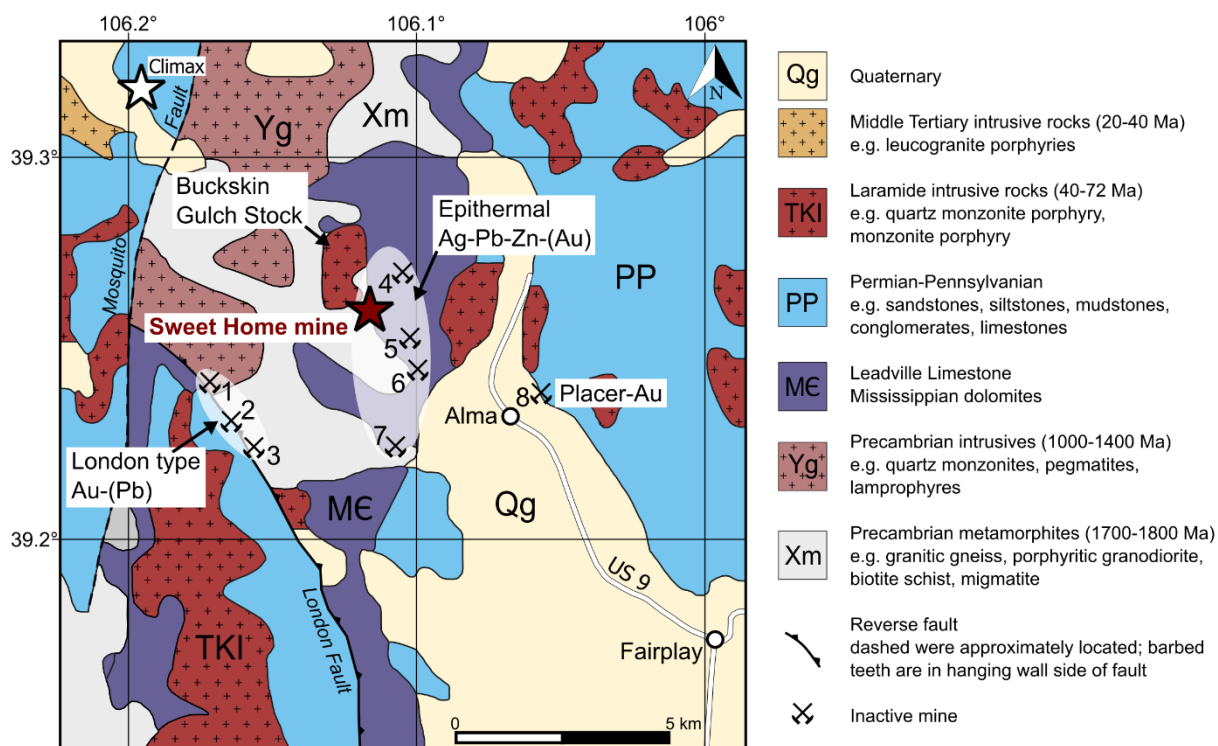
Figure 5 Geological map of the Mosquito range (Colorado) showing the location of the Sweet Home mine, the Climax Mo deposit, and other historical mining locations. 1 = North London mine, 2 = South London mine, 3 = American mine, 4 = Dolly Varden mine, 5 = Paris mine, 6 = Phillips mine, 7 = Hock Hocking mine, 8 = Richards Placer (Misantoni et al. 1998). Strike and dip directions are shown in the detailed geologic maps of the Climax (McCalpin et al. 2012) and Alma quadrangles (Widmann et al. 2004).

The vein-type mineralization at the Detroit City portal (DCP) of the SHM studied here is located approximately 60 m above the uppermost SHM workings that were accessible via the Sweet Home portal. The DCP is thus the vertical extension of the SHM (Figs. 6a, b).
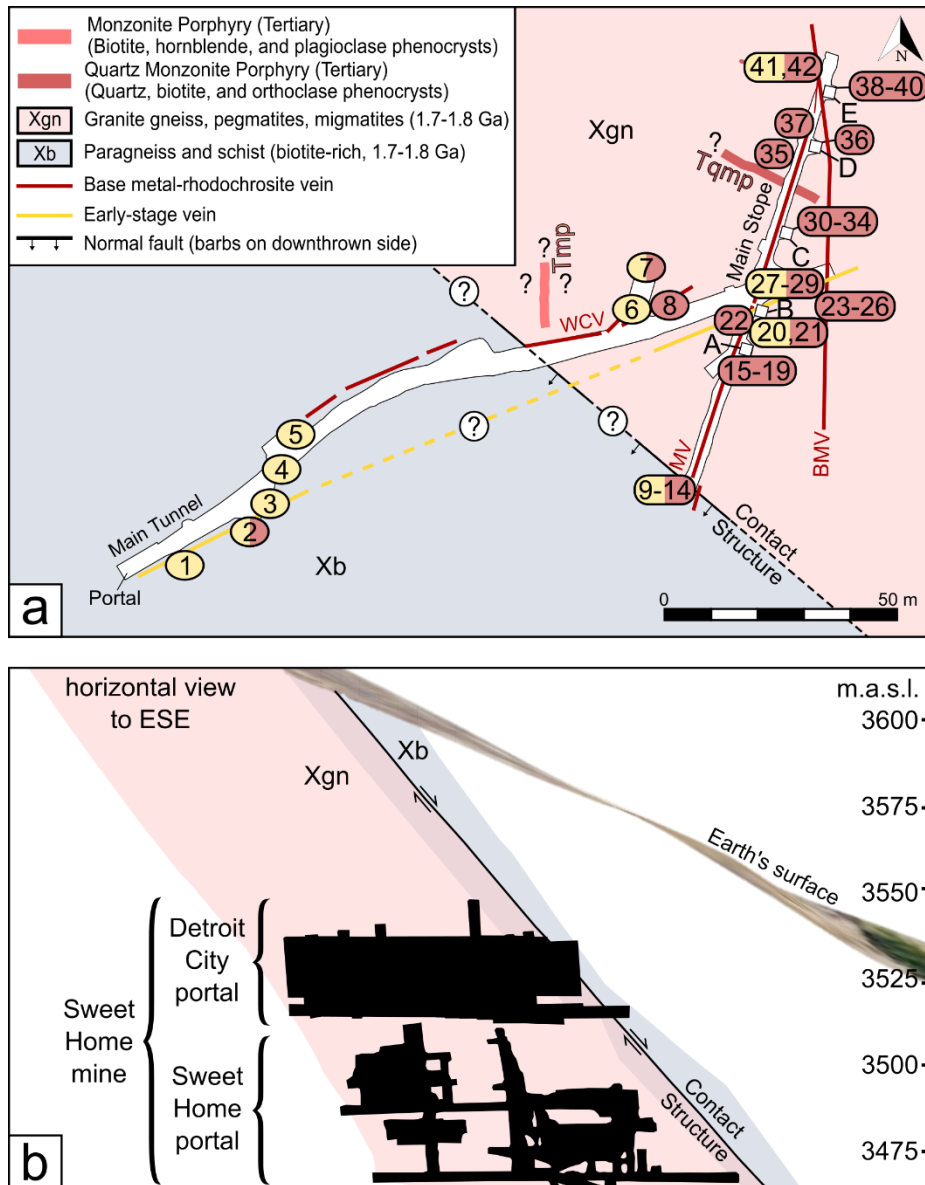
Figure 6 (a) Simplified geological map of the Detroit City portal (by courtesy of D. Misantoni). Sample suites marked in yellow contain minerals of the early stage; sample suites in pink contain minerals from the main sulfide stage. Molybdenite occurs at the crosscut of the main vein with the Contact Structure. Sample fields showing more than one number identify different samples from the same locality. MV = Main vein, WCV = Watercourse vein, BMV = Blue Mud vein, TV = Tetrahedrite vein, PV = Pyrite vein. (b) Projection onto cross-section of the Sweet Home mine with the former SHP workings at the bottom and the DCP workings above with horizontal view at the Main vein stopes. It is noteworthy that the Contact Structure is only intersected by the DCP workings (by courtesy of S. Bourque).

The SHM was formerly operated as the most productive part of a Ag-base metal vein swarm in the Alma mining district, which extends to the NE through the Red Amphitheater and into Mt. Bross, and to the SW across the Buckskin Creek (Appendix Fig. 4). Some features of polymetallic vein-type mineralization at the SHM are similar to those of peripheral veins at the Climax Mo deposit, which is located ~8 km to the NW, and of the far distal Urad-Henderson Mo deposit (Fig. 4). The similarities include: i) the age of mineralization between 26.0 and 24.8 Ma (Misantoni et al. 1998; Barbá et al. 2005; Romer and Lüders 2006), ii) the presence of Tertiary

porphyry rhyolite dikes and molybdenite-bearing pegmatites (Misantoni et al. 1998), and iii) the occurrence of a pebble dike (7.5 m thick), which contains rounded clasts of Precambrian rocks in a matrix of quartz, fluorite, and pyrite (Bookstrom 1989). Recent observations of geological features at the SHM support a genetic relationship to a Climax-type Mo porphyry system. In the past years of mining, several greisen veins were exposed at the DCP, which are commonly reported from ore shells in the apical parts of underlying porphyry stocks of Climax-type Mo deposits (Appendix Fig. 3). Recent tunneling at the DCP crosscut a major fault known as the Contact Structure (D. Misantoni, pers. commun.), which separates Precambrian biotite-rich metamorphic rocks (Xb; gneiss, schist) from granitic rocks (Xgn; e.g. granite gneiss, pegmatite, migmatite). Outcrops along this structure expose molybdenum-bearing mineralization in the form of molybdenite-quartz-fluorite-pyrite veins and fault gouge.

This study aimed to decipher the evolution of the magmatic-hydrothermal system of the SHM in the Alma district and to test a possible relationship of the mineralization to a hypothesized deeper-seated porphyry intrusion, as proposed by Lüders et al. (2009). The minerals from the main sulfide-stage and late-stage mineralization have already been characterized (Lüders et al. 2009), therefore this study focuses on samples from the Contact Structure and the early-stage (greisen) mineralization. We conducted fluid inclusion microthermometry and laser Raman analyses as well as analyses of fluid inclusion water and gases (CO_2 and noble gases). In addition, stable C, O, and S isotope analyses of carbonates and sulfides were performed.

2.2 Geological setting

2.2.1 Regional geology

The Colorado Mineral Belt (CMB) extends ~400 km throughout the present state of Colorado (Fig. 4). It comprises several magmatic intrusions of different age and composition that were emplaced during various tectonic events. The first of these (75-43 Ma) was during the Laramide orogeny and characterized by episodic emplacements of monzonites and granodiorites (Bookstrom 1989). The second event occurred towards the end of Laramide compression (43-37 Ma), where flat slab rollback led to intrusions of quartz monzonites and created pathways for fluid migration (Chapin 2012 and references therein). This episode is characterized by Zn-Pb-Ag-Au sulfide replacement ores at Leadville (Figs. 4, 5) and by Gilman and Sherman-type Ag-Pb-Zn-Ba ores in karst zones in Leadville limestones (Behre 1953; Johansing et al. 1990; Thompson and

Arehart 1990). After a short period of tectonic inactivity, the Rio Grande Rift system started to develop at ca. 33 Ma (Fig. 4), which was accompanied by the third period of intrusive magmatism (until ~25 Ma), involving both highly evolved silica-rich magmas and minor mafic alkaline magmas (Bookstrom 1981; Bookstrom et al. 1988; Bookstrom 1989; Shannon et al. 2004; Ludington and Plumlee 2009). The reactivation of older fault zones and structural lineaments facilitated the ascent of these bimodal magmas and the migration of fluids, enabling the formation of Climax-type Mo porphyry deposits (Lipman and Mehnert 1975; Westra and Keith 1981; White et al. 1981; Bookstrom et al. 1988; Bookstrom 1989; Geissman et al. 1992; Carten et al. 1993; Keith et al. 1993; Wallace and Bookstrom 1993; Russell and Snelson 1994; Shannon et al. 2004; Markey et al. 2007; Ludington and Plumlee 2009; Audétat 2010; Audétat et al. 2011; Mercer et al. 2015) and peripheral Au ± Ag ± Mo ± base metal lodes (Bookstrom 1989; Wallace and Bookstrom 1993; Misantoni et al. 1998; Barbá et al. 2005; Romer and Lüders 2006). The upper parts of the porphyry Mo orebodies exhibit phyllic alteration assemblages of quartz–pyrite–sericite accompanied by greisen quartz–pyrite–topaz–huebnerite-bearing veinlets (e.g., White et al. 1981; Bookstrom 1989). Late peripheral veins contain Ag–Pb–Zn–polymetallic sulfides in a gangue of quartz, fluorite, rhodochrosite, calcite, and/or barite (Bookstrom 1989). In both the Climax and Urad-Henderson areas, Precambrian molybdenum- and tungsten-rich pegmatites, granites, and schists occur (Tweto 1960; Theobald et al. 1983; Wallace 1995), which may be possible metal sources for younger ore mineralization.

2.2.2 Local geology

Detailed geological descriptions of the Alma district and the Sweet Home mine (SHM) are provided by Misantoni et al. (1998), Widmann et al. (2004), and Bartos et al. (2007) and are briefly summarized here. Geological features, mineralization types, and mining locations are shown in Fig. 5. The Alma mining district hosts different types of ore deposits of former economic interest: i) Au-bearing polymetallic veins in the London sub-district, ii) placer gold in glacial, colluvial, and alluvial gravels, and iii) Ag-bearing polymetallic veins that were mined at the SHM (Misantoni et al. 1998). The SHM was the most productive silver mine among several ones located along a NE–SW to E–W-trending swarm of veins with Pb-Zn-Cu-Ag-W mineralization (Appendix Fig. 4). Besides the aforementioned mineralization types, the Alma mining district also hosts minor molybdenum-bearing quartz(±fluorite±pyrite) veins. Bookstrom et al. (1987; 1988) related the latter to the last pulse of hydrothermal fluids from the underlying Alma Batholith at ca. 26 Ma, which may have occurred coevally with the final stage of ore deposition at Climax.

Five main veins are recognized at the SHM, namely, the Main, the Tetrahedrite, the Watercourse, the Blaine, and the Blue Mud veins (Misantoni et al. 1998). The locations of these veins in the Detroit City portal are shown in Fig. 6a, along with recently exposed Pyrite veins (D. Misantoni, pers. commun.). The vertical extension of the mine workings is shown in Fig. 6b. The veins are hosted by Precambrian biotite schist (Fig. 7a), granitic gneisses and granodiorite. These Precambrian units were intruded by Tertiary quartz-monzonite and monzonite porphyries and molybdenite-bearing quartz-orthoclase pegmatites of possibly Tertiary age (Misantoni et al. 1998).

The rock units were altered and mineralized during multiple events of fluid migration. Propylitic (epidote–chlorite–hematite–pyrite) alteration is ubiquitous, although not directly related to vein mineralization at the SHM. Local potassic alteration of gneisses occurs in the form of plagioclase replacement by K-feldspar, and replacement of coarse metamorphic biotite by fine biotite flakes in the central part of the tetrahedrite vein from the former SHM workings (Bartos et al. 2007). There are rare showings of 1-2 cm wide pinkish K-feldspar veinlets in the same area, which are intersected by base metal sulfide-rhodochrosite veins (Barbá et al. 2005). Phyllic (quartz–pyrite–sericite) and greisen alteration of the host rock are related to emplacement of early-stage greisen veins, pyrite±huebnerite±sphalerite veins with quartz and fluorite gangue, and muscovite/sericite or quartz–pyrite–sericite veins (Misantoni et al. 1998; Bartos et al. 2007) (Figs. 7b, 8). Whereas fluorite of the early stage shows strong zonation under hot cathode cathodoluminescence (CL), milky and euhedral quartz do not show CL colors (Fig. 7c). This early-stage vein mineralization locally also contains black sphalerite and huebnerite, the latter yielding a U-Pb age of 25.7 ± 0.3 Ma (Romer and Lüders 2006). The early-stage mineralization also locally contains isolated, thin, quartz-pyrite-molybdenite veins (Figs. 7d, e) and molybdenite coatings on fractures, which exclusively occur at the crosscut of the main vein with the Contact Structure (Figs. 6a, 7a). The phyllic and greisen alteration was rarely observed in the former SHM workings, but is abundant in the DCP (Fig. 7b). This is due to the orientation of the Contact Structure, which intersects just a small part of the Sweet Home portal (SHP) but larger parts of the DCP workings (Fig. 6b).

Tectonic movements along N-S and NE-trending faults enabled the opening of void spaces and the migration of ore fluids, resulting in precipitation of base metal sulfides and gemmy rhodochrosite during the main sulfide stage. Subsequently, rhodochrosite and fluorite precipitated in the late stage, the latter predominantly along NE-trending veins (Misantoni et al. 1998)(Figure 8). The main sulfide stage is characterized by galena, chalcopyrite, sphalerite, bornite, and sulfosalts (tetrahedrite/tennantite) with quartz, gemmy and murky rhodochrosite and minor purple fluorite as gangue minerals (Fig. 8). The late-stage mineralization is made up of pinkish rhodochrosite, purple fluorite, calcite, barite, and apatite (Fig. 8). Late-stage apatite

yielded a U-Pb age of 24.8 ± 0.5 Ma (Romer and Lüders 2006). Some of the main sulfide-stage and late-stage veins are superimposed on the early-stage veins.
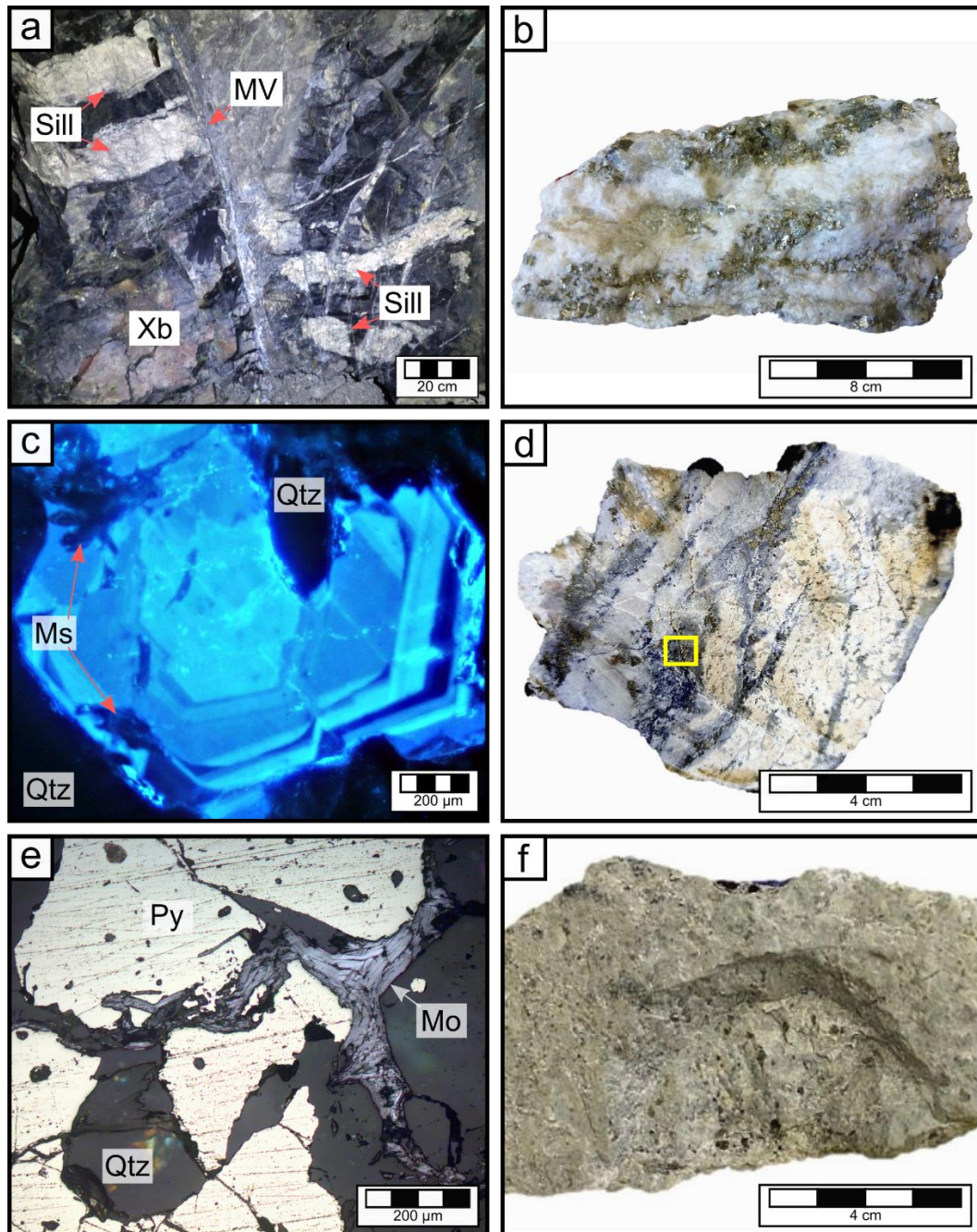
Figure 7 (a) Underground outcrop showing the crosscut of the Main vein (MV) and the Contact Structure. The offset of the Precambrian rocks (Xb) is indicated by the displaced (white rhyolite) sills. (b) Sample from a pyrite vein showing greisen assemblages: pyrite, quartz, fluorite, and sericite (Sample 6, see Fig. 6a for location). (c) CL image showing fluorite in blue CL colors and strong zonation. Note that fluid inclusions are hosted within the zonation layers and do not crosscut grain boundaries. Muscovite (Ms) and quartz (Qtz) are present but do not show CL colors. (d) Sample 14: Molybdenite vein in a greisen assemblage of pyrite, quartz, and fluorite hosted by altered granite gneiss from the Contact Structure area. The yellow box refers to enlargement in Fig. 7d. (e) Photomicrograph showing molybdenite aggregates (Mo) replacing pyrite and quartz (Qtz) crystals (Sample 14). (f) White porphyry sample from the Contact Structure area.

The emplacement of intrusive rocks in the area of the SHM was structurally controlled (Misantoni et al. 1998). Three major structural trends are present: (i) an early NW–SE to E–W fault and fracture trend that is parallel to foliation and banding in the Precambrian gneiss, (ii) a NE–SW fault trend that contains the majority of the productive veins, and (iii) a late, N–S-trending fault and fracture zone. All three trends contain porphyry intrusions that are hydrothermally altered and mineralized. Several other tectonic features were observed since the opening of the DCP in 2017. The most important one is a NW–SE-trending and SW-dipping fault, known as the Contact Structure (D. Misantoni, pers. commun.). This fault is likely Precambrian in age, and it forms the contact between Precambrian gneiss to the NE and biotite schist to the SW (Figs. 6a, b). The Contact Structure in the DCP was intruded by a white porphyry dike with similar mineralogical features (e.g. alteration style, pyramidal quartz phenocrysts, Fig. 7f) as the porphyry stocks found at Climax. Most of the molybdenite-bearing samples found at the DCP so far were retrieved from outcrops along the Contact Structure (Fig. 6a).

	Early stage: Greisen veins, greisen / phyllic alteration	Main sulfide stage	Late stage
Gangue minerals			
Milky quartz	▬		
Euhedral quartz	▬	▬	
Fluorite	*orange, green, transparent* ▬	*purple* ▬	*purple* ▬
Muscovite	▬		
Rhodochrosite		*gemmy, murky* ▬	*pink* ▬
Calcite			▬
Apatite			▬
Barite			▬
Ore minerals			
Huebnerite	▬		
Pyrite	▬	▬	
Molybdenite	▬		
Sphalerite	▬	▬	
Tetrahedrite/Tennantite		▬	
Galena		▬	
Chalcopyrite		▬	
Bornite		▬	

Figure 8 Simplified paragenetic scheme of the mineralization at the Sweet Home mine.

2.3 Samples and analytical methods

2.3.1 Sampling and petrography

The samples studied here originate from the DCP (Figs. 6a, b) and were collected to represent early-stage mineralization consisting mostly of milky quartz, fluorite, muscovite and pyrite, locally also huebnerite and/or sphalerite. Some early-stage assemblages contain molybdenite vein fillings, which has not been reported from the former Sweet Home workings at all. A detailed description of the samples is shown in **Fehler! Verweisquelle konnte nicht gefunden werden.**. The Appendix Table 1 provides an overview of the methods used, which are briefly described below.

Doubly-polished thick sections of ore and gangue minerals were prepared at the Institute of Geosciences, University of Potsdam (Germany) for transmitted and reflected light microscopy, fluid inclusion (FI) microthermometry and laser Raman spectroscopy. Following the recommendation by Lüders and Ziemann (1999), the thickness of pyrite sections for microscopic observations in near infrafred (IR) light was 90 µm. All other thick sections have a thickness of ca. 180 µm. Moreover, representative samples were selected for cathodoluminescence (CL) petrography. The hot-cathode optical CL system was operated at 14 keV and 0.10-0.20 mA. Exposure times were varied to capture zonation and differences in luminescence.

2.3.2 Microthermometry

Fluid inclusions in transparent minerals (quartz, fluorite, sphalerite, huebnerite) were measured by conventional microthermometry using a FLUID INC-adapted U.S.G.S. gas-flow heating/freezing system mounted on an Olympus BX50 microscope with a long-distance 40× objective with coverslip correction. Fluid inclusions in pyrite were measured using a Linkam THMS 600 heating/freezing system on an Olympus BHSM-IR microscope with a 50× IR objective and a QCam infrared InGaAs camera, which allows observation in the wavelength range between λ=800 and 1800 nm at low IR light intensity (Lüders 2017). Some samples of huebnerite and sphalerite, which showed highly variable transmittance, were either studied in transmitted light or in near IR light. Both approaches using a Linkam and a U.S.G.S. system are operated at the German Research Centre for Geosciences (Potsdam, Germany).

Table 1 Sample origin and description

Sample number[1]	Approximate Elevation (m.a.s.l.)[2]	Stage[3]	Assemblage[3,4]
1	3515	Early stage	Qtz-Ms-Py vein with orange and green Fl in pores
2	3515	Early stage, Main sulfide stage	Qtz-Py-Hub-Fl overgrown by euhedral Qtz and base metal sulfides
3	3515	Early stage, Main sulfide stage	Disseminated Py in altered Xb, overgrown by euhedral early-stage Sp and violet Fl
4	3515	Early stage	Qtz-Py-Ms-orange Fl with more orange Fl and euhedral Sp in pores
5	3515	Early stage	Qtz-Fl-Ms-Py vein
6	3515	Early stage	Qtz-Ms-Py-Hub vein
7	3515	Early stage, Main sulfide stage	Qtz-Py vein replaced by base metal sulfides
8	3515	Early stage, Late stage	Qtz-Py-Hub vein with minor pink Rds and late violet-Fl
9	3515	Early stage, Main sulfide stage	Py in a massive sulfide matrix (Tet/Ttn, Gn, Sp) with minor Qtz and murky Rds
10	3530	Early stage, Main sulfide stage	Py in a massive sulfide matrix (Ccp, Sp)
11	3525	Early stage, Main sulfide stage	Qtz-Py vein with minor Hub, Sp and main sulfide-stage base metals
12	3515	Early stage	Disseminated Py in altered Xgn with Mol coating
13	3515	Early stage	Disseminated Py in altered Xgn with Mol coating
14	3525	Early stage	Disseminated Py in altered Xgn cut by Qtz-Fl-Py-Mol vein
15	3520	Early stage, Main sulfide stage	Disseminated Qtz and Py in altered Xgn bordering a massive base metal sulfide-murky Rds vein
16	3525	Main sulfide stage, Late stage	Massive base metal sulfide vein together with late violet fluorite
17	3515	Main sulfide stage, Late stage	Massive base metal sulfide together with late violet fluorite
18	3515	Main sulfide stage	Massive base metal sulfide
19	3515	Main sulfide stage, Late stage	Pink Rds crystals growing on base metal sulfides
20	3520	Early stage, Main sulfide stage	Disseminated Qtz and Py in altered Xgn bordering a massive base metal sulfide-murky Rds vein
21	3525	Early stage, Main sulfide stage	Py in a massive sulfide matrix with minor Qtz and murky Rds
22	3515	Main sulfide stage	Base metal sulfides in a gangue of murky Rds and differentially colored Fl
23	3515	Late stage	Pink Rds crystals
24	3515	Late stage	Pink Rds together with euhedral Qtz, Ap and clay
25	3515	Late stage	Pink Rds and minor violet Fl crystals

2 A geochemical study of the Sweet Home mine, Colorado Mineral Belt, USA

26	3515	Late stage	Pink Rds and minor Ap crystals
27	3515	Early stage	Qtz-Py-Hub vein
28	3515	Early stage	Qtz-Ms-Py-Sp-Hub overgrown by euhedral Qz, base metal sulfides and Rds
29	3515	Early stage	Qtz-Py-Hub-Sp growing in open space
30	3515	Late stage	Pink Rds and violet Fl crystals on Tet/Ttn
31	3515	Late stage	Pink Rds crystals
32	3515	Early stage, Main sulfide stage	Disseminated Py in altered Xgn bordering a massive base metal sulfide-murky Rds vein
33	3515	Main sulfide stage, Late stage	Euhedral Qtz and pink Rds growing on massive base metal sulfides
34	3515	Late stage	Rds crystals
35	3515	Early stage, Main sulfide stage	Remnants of early-stage Py in a vein of Qtz-base metal sulfide-violet Fl
36	3515	Late stage	Pink Rds and violet Fl crystals
37	3515	Main sulfide stage, Late stage	Altered Xgn bordered by Qtz-base metal sulfides-pink Rds together with late violet Fl and Ap
38	3515	Main sulfide stage, Late stage	Pink Rds crystals growing on Tet/Ttn
39	3515	Main sulfide stage, Late stage	Pink Rds together with euhedral Qtz, base metals sulfides and violet Fl
40	3515	Main sulfide stage, Late stage	Pink Rds growing on massive base metal sulfides
41	3525	Early stage, Main sulfide stage	Py in a massive sulfide matrix with minor Qtz
42	3520	Early stage, Main sulfide stage	Coarse-grained massive sulfide-murky Rds sample with remnants of early Qtz-Py-Sp
43	dump	Early stage	Qtz-Hub vein

[1] Sample locations are shown in Fig. 6a

[2] Vertical extension of the mine workings are shown in Fig. 6b

[3] Relative timing of mineralization stages and mineral assemblages are displayed in Fig. 8

[4] Qtz = quartz, Ms = muscovite, Py = pyrite, Hub = hubnerite, Fl = fluorite, Sp = sphalerite, Rds = rhodochrosite, Tet = tetrahedrite, Ttn = tennantite, Gn = galena, Ccp = chalcopyrite, Mol = molybdenite, Ap = apatite, Xb = Biotite schist, Xgn = Granite gneiss

The Linkam and U.S.G.S. heating-freezing stages were calibrated with Synflinc synthetic inclusions (Sterner and Bodnar 1984). The measurement precision is ±0.1°C for ice melting temperatures (T_m) and ±1°C for homogenization temperatures. Salinity in equivalent weight percent NaCl (wt.% equiv. NaCl) was calculated from low-temperature phase changes using the HokieFlincs_H_2O-NaCl spreadsheet (Bodnar 1993; Steele-MacInnis et al. 2012). The salinity of CO_2-bearing inclusions was calculated via clathrate melting temperatures using the equations from Darling (1991) and Barton and Chou (1993).

2.3.3 Laser Raman spectroscopy

The gas contents in vapor-rich inclusions and vapor bubbles of aqueous two-phase fluid inclusions as well as trapped solid phases were analyzed using a Jobin-Yvon LabRam confocal laser Raman microspectrometer paired with an Olympus optical microscope at the German Research Centre for Geosciences (Potsdam, Germany). All measurements were taken with an MPlan 100×/0.90 objective lens. The excitation radiation was from a 532.6 nm Nd-YAG laser (100 mW). Silicon (520 cm^{-1}) and diamond (1332 cm^{-1}) were used for internal calibration. Raman spectra were collected in the spectral range between 100 and 1300 cm^{-1} for gas-rich and aqueous inclusions and between 1200 and 2950 cm^{-1} for trapped solids. Acquisition times were 2 x 30 s for gas-rich and aqueous inclusions and 2 x 60 s for solids.

2.3.4 Hydrogen and oxygen isotope analysis of fluid inclusions

Isotope analysis of fluid inclusion water was made on selected ore and gangue minerals from the early greisen stage, as well as from the main sulfide and late stage, at the Max Planck Institute for Chemistry (Mainz, Germany). Bulk analyses of fluid inclusion hydrogen and oxygen isotope ratios were performed using two different continuous-flow techniques designed for online analysis of mineral samples of up to 2 g (de Graaf et al. 2020a). One technique couples a mechanical crusher unit to a continuous-flow isotope ratio mass spectrometry (IRMS) instrument (Thermo Scientific Delta V). The crusher unit is maintained at a temperature of 120°C to achieve complete evaporation of fluid inclusion water upon sample crushing. The released water vapor is collected in a cryogenic trap that can be heated to generate a water pulse long enough to be analyzed. After leaving the cryogenic trap, the water vapor is guided to a continuous-flow

pyrolysis furnace (Thermo Scientific TC-EA), which produces H_2 and CO gas as a result of reaction with glassy carbon at 1400°C. The H_2 and CO are subsequently introduced to the IRMS instrument where a rapid magnet peak jump allows for analysis of both hydrogen and oxygen isotopes from a single water release. Isotope values of fluid inclusion water are reported as δ^2H_w and $\delta^{18}O_w$ ratios relative to VSMOW. Samples measured following the analytical protocol are typically reproducible (1σ) within 0.4‰ for $\delta^{18}O_w$ and 2.0‰ for δ^2H_w.

The second technique makes use of a cavity ring-down spectroscopy (CRDS) instrument (Picarro L2140-i) connected to a crusher unit at 120°C. The N_2 carrier gas in the system is continuously moisturized to create a stable water vapor background and eliminate memory effects in the analyzer. Mineral samples are crushed to liberate fluid inclusion water and generate a peak addition to the steady water background. Oxygen and hydrogen isotope values of the fluid inclusion water can be calculated by subtracting the background from the sample peak. Reproducibility of mineral crushes on the CRDS system is within 0.3‰ for $\delta^{18}O_w$ and 1.1‰ for δ^2H_w. Both the IRMS and CRDS setup produce accurate fluid inclusion isotope data as shown in a comparison experiment for these two techniques reported by de Graaf et al. (2020a).

2.3.5 Carbon and nitrogen isotope analysis of fluid inclusions

The carbon isotopic composition of carbon dioxide and methane as well as the nitrogen isotopic composition of fluid inclusions hosted in fluorite and quartz was analyzed using a sample crusher connected via a GC-column to an elemental analyzer (EA)-IRMS system at the German Research Centre for Geosciences (Potsdam, Germany). The system uses a continuous flow of He carrier gas (purity 5.0) at a stable rate of 300 ml/min. After crushing of 0.2-0.5 g sample chips, the He–gas mixture passes through a molecular sieve where N_2, CH_4 (if present), and CO_2 are separated from each other. The gas species enter the oxidation column of the EA, where CH_4 (if present) is oxidized to CO_2 with simultaneous injection of O_2 at 960°C. After passing the reduction column and water trap, the gas species N_2, CO_2 from CH_4 oxidation, and original CO_2 from inclusions are separated in a second molecular sieve and enter the IRMS via a Conflo III interface. The isotopic ratios of nitrogen and carbon dioxide were measured online and compared to reference gases calibrated against IAEA-N1 for N_2 and NBS19 for CO_2. Reproducibility of the $\delta^{15}N$ (N_2) and $\delta^{13}C$ (CO_2, CH_4) values of fluid inclusion gases are at or below 1.1‰. For details see Plessen and Lüders (2012).

2.3.6 Carbon and oxygen isotope analysis of rhodochrosite

Crushed rhodochrosite samples were analyzed for carbon and oxygen isotopes on a Thermo Scientific Delta V Advantage mass spectrometer equipped with a Gasbench II gas preparation unit (Thermo Scientific) at the Department of Earth Sciences, Vrije Universiteit Amsterdam (Netherlands). Around 10 μg of sample material was placed in a He-filled 12-ml exetainer vial for sample digestion in concentrated anhydrous H_3PO_4 at a temperature of 45 °C. The generated CO_2–He gas mixture was transported into the Gasbench II in a He carrier flow. In the Gasbench II, water was removed through Nafion tubing, and CO_2 was analyzed in the mass spectrometer after extraction of residual gases in a GC column. Raw data were calibrated against the calcite Vrije Universiteit Amsterdam-Internal Carbonate Standard (VICS; 1.45‰ for $\delta^{13}C$ and -5.44‰ for $\delta^{18}O$). This introduces no bias since rhodochrosite and calcite have a similar phosphoric acid fractionation factor. The isotope ratios are reported as $\delta^{13}C_{Rds}$ and $\delta^{18}O_{Rds}$ ratios relative to VPDB. The typical reproducibility (1σ) of routinely analyzed carbonate standards is better than 0.1‰ for both $\delta^{13}C$ and $\delta^{18}O$.

2.3.7 Noble gas analysis of fluid inclusions

Noble gas analyses were performed on 0.2 to 1.0 g of hand-picked separates of ore and gangue minerals from the early and main sulfide stages at the German Research Centre for Geosciences (Potsdam, Germany). The samples were loaded into an ultrahigh-vacuum spindle crusher, which was pumped at room temperature for 24 h to remove atmospheric gases adsorbed on grain surfaces. For gas extraction, the samples were crushed under vacuum, and the gases released were admitted to the preparation line. Water was frozen in a dry ice-cooled trap and other chemically active species were removed in Ti sponge and ZrAl getters. The noble gases were then separated from each other in a cryogenic adsorber, and noble gas concentrations and isotopic compositions were determined in a VG5400 noble gas mass spectrometer according to procedures described by Niedermann et al. (1997). Total analytical blanks (determined prior to each crushing extraction, in cm^3 STP) were $(1-4) \times 10^{-12}$ for ^4He, $(0.5-2.3) \times 10^{-12}$ for ^{20}Ne, $(4-14) \times 10^{-10}$ for ^{40}Ar, $(3-15) \times 10^{-14}$ for both ^{84}Kr and ^{132}Xe, with atmospheric isotopic compositions.

2.3.8 Reliability of fluid inclusion bulk analysis

Bulk analysis of fluid inclusions extracted from minerals by crushing or heating inevitably provides data from all fluid inclusion populations (i.e., primary and secondary fluid inclusions) present in a sample. This is a major point of criticism against the reliability of bulk crush-leach or isotope analysis (see Chi et al. 2021 and references therein). However, the validity of bulk analysis can be increased considerably by carefully evaluating the fluid inclusion inventory and selecting samples that contain only one dominant fluid inclusion population. Plessen and Lüders (2012) tested the validity of fluid inclusion bulk analysis in a study using an online technique for carbon isotope analysis of CO_2 in fluid inclusions. The authors showed that variations in $\delta^{13}C_{CO2}$ values of quartz-hosted gas-rich fluid inclusion assemblages in previously studied quartz chips from the Ashanti gold mine (samples GH-172 and GH-151) gave excellent reproducibility in the range of 0.5 and 0.4‰, respectively. The same holds true for $\delta^{13}C$ values of CO_2 and CH_4 and $\delta^{15}N$ values of gas-rich inclusions hosted in different minerals in other case studies (e.g., Lüders et al. 2012; Plessen and Lüders 2012; Lüders and Plessen 2015). The results of these studies show that the influence of different fluid inclusion populations can be minimized by careful sample selection. Similarly, excellent reproducibility was found for online analysis of δ^2H and $\delta^{18}O$ of fluid inclusion water in various minerals from vein-type ore and fluorite from the Harz Mountains in Central Germany (de Graaf et al. 2020b). For this study, only samples that dominantly host one fluid inclusion population were chosen for bulk isotope analyses, thus we are confident that the results represent a single fluid event.

2.3.9 Sulfur isotope analysis

Sulfides and sulfosalts from the early greisen and main sulfide stages were measured via EA-IRMS (Elemental analyzer-isotope ratio mass spectrometer) using a Flash-EA Isolink CN interfaced to a ThermoScientific Delta V Advantage mass spectrometer at the Institute for Geology and Paleontology, University of Münster (Germany). Depending on the specific mineral, between 150 and 450 µg of hand-picked separates were homogeneously mixed with 200-600 µg of vanadium pentoxide and weighed in a tin capsule. Reference materials for sulfur isotope measurements were NBS-127, IAEA-S-1, IAEA-S-2, IAEA-S-3, and an in-house Ag_2S standard. External reproducibility as determined through replicate analyses of reference materials was better than ± 0.3 ‰ (1σ).

2.4 Results

2.4.1 Fluid inclusion petrography

The classification of fluid inclusions (FI) as primary, pseudosecondary, and secondary and the definition of fluid inclusion assemblages (FIA; coevally trapped fluid inclusions along features such as crystal planes, growth zones, or healed microfractures) followed the criteria suggested by Roedder (1984) and Goldstein and Reynolds (1994).

We identified three types of fluid inclusions hosted in gangue and ore minerals of the early-stage mineralization: type 1) vapor-rich aqueous carbonic, three-phase FIs in milky quartz and fluorite; type 2) vapor-rich, two-phase FIs in milky quartz and fluorite; and type 3) aqueous, two-phase FIs in milky quartz, fluorite, pyrite, huebnerite, and sphalerite (Table 2).

At room temperature, aqueous carbonic type 1 FIs contain a vapor bubble, liquid CO_2, and minor aqueous liquid (Figs. 9a, b). Coevally trapped FIAs of type 1, 2, and 3 inclusions were found in early-stage quartz and fluorite (Figs. 9a, b). Some type 2 and 3 FIs hosted in fluorite near muscovite (coarse and/or sericite) contain solid inclusions of calcite (Fig. 9c) or anhydrite (Fig. 9d). Additionally, fluorite hosts isolated primary type 1 and 3 FIs, which locally show negative crystal shapes (Fig. 9a). Quartz locally shows growth zones that are decorated with primary type 3 FIs (Fig. 9e).

Aqueous, two-phase type 3 FIs are most common in early-stage quartz, fluorite, and in the ore minerals sphalerite, huebnerite (Fig. 9f), and pyrite (Fig. 9g), where the inclusions occur in clusters or are arranged along trails.

Due to the great abundance of FIs in some inclusion trails and clusters a classification of primary, pseudosecondary or secondary is uncertain or even impossible. However, these trails and clusters are always found within growth zones, which are visible in fluorite under CL (Fig. 7c), or in individual crystals, where they do not cross grain boundaries. Therefore, the investigated FIs may be pseudosecondary rather than primary, but they are unlikely to be secondary and thus are valid for interpretation of mineralization conditions.

Generally, type 1 and 2 FIs can mostly be classified as primary, whereas type 3 FIs may be either of primary or secondary origin. However, secondary type 3 FIs in early-stage minerals are rare and commonly are arranged along trails crosscutting fluorite. The liquid-vapor ratios of secondary inclusions are considerably higher than those in primary and pseudosecondary type 3 FIs (Fig. 9h); they are not included in Fig. 10.

Table 2 Comparison of fluid inclusion types in minerals from the SHM with quartz-hosted fluid inclusions from Climax-type deposits

	Sweet Home mine[1]	Climax[2]	Henderson[3]	Questa[4]
Type 1 Aqueous carbonic three-phase FIs	Low- to intermediate-salinity (1-10 wt.% equiv. NaCl) T_h = 308-367°C	Rare T_h > 350°C	Not described	Low- to intermediate-salinity (0-9 wt.% equiv. NaCl) T_h = 130-260°C
Type 2 CO$_2$ vapor-rich FIs	Low- to intermediate-salinity (5-10 wt.% equiv. NaCl) T_h = 316-380°C	T_h > 350°C	Intermediate- to high-salinity (10-20 wt.% equiv. NaCl) T_h = 200-390°C	Low- to intermediate-salinity (1-8 wt.% equiv. NaCl) T_h = 380-410°C
Type 3 Liquid-rich FIs	Low- to high-salinity (2-11 wt.% equiv. NaCl) T_h = 259-362°C Solids: Cal, Anh	Low- to intermediate-salinity (0.7-12 wt.% equiv. NaCl) Solids: Anh, carbonates	Low- to intermediate-salinity (0-5 wt.% equiv. NaCl) T_h = 200-390°C	Low- to high-salinity (1-17 and 7-20 wt.% equiv. NaCl) T_h = 250-500°C (majority 350-450°C)
Type 4 Highly saline halite- bearing FIs	Not observed	37-42 wt.% equiv. NaCl T_h = 180-200°C Solids: Hl Rarely liquid CO$_2$	29-65 wt.% equiv. NaCl T_h = 310-530°C Solids: Hl, Mo, Hm, carbonates	30-50 and 45-65 wt.% equiv. NaCl T_h = 130-260 and 250-490°C Solids: Hl, Syl, Hm, Mo, Rarely liquid CO$_2$

[1] Reynolds 1998; Lüders et al. 2009; this study (Appendix Table 2)
[2] Hall et al. 1974
[3] White et al. 1981; Seedorff and Einaudi 2004b
[4] Bloom 1981; Smith 1983; Cline and Bodnar 1994; Klemm et al. 2008; Rowe 2012
Hl halite, *Syl* sylvite, *Cal* calcite, *Anh* Anhydrite, *Mo* molybdenite, *Hm* hematite
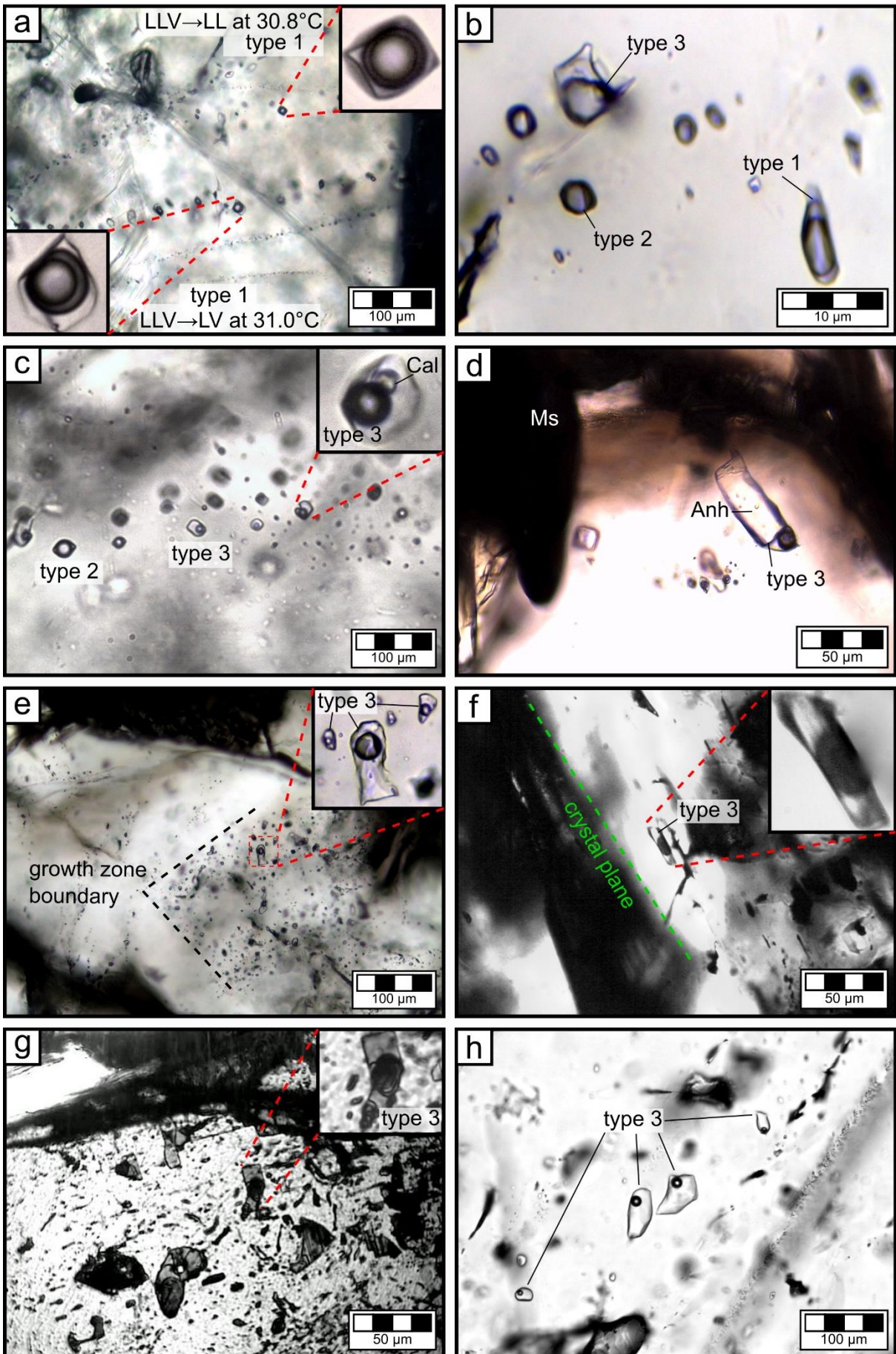
Figure 9 Photomicrographs of FIs hosted in early-stage greisen mineralization. (a) Trails of carbonic three-phase (type 1), vapor-rich (type 2), and aqueous, liquid-rich (type 3) FIs in fluorite showing negative crystal shape (Sample 1). Focused type 1 FIs show different carbonic homogenization behavior as the top right one homogenizes to the liquid phase at 30.8°C and the bottom left one to the vapor phase at 31.0°C. (b) A cluster of carbonic three-phase (type 1), vapor-rich (type 2), and low-carbonic, aqueous, liquid-rich (type 3) FIs in milky quartz (Sample 5). (c) Trail of vapor-rich (type 2) and low-carbonic, aqueous, liquid-rich (type 3) FIs in fluorite. The focused FI shows an inherited calcite crystal (Sample 5). (d) Low-carbonic, aqueous, liquid-rich (type 3) FIs in fluorite showing an inherited anhydrite crystal (Sample 14). (e) Quartz showing growth zone boundaries and focused low-carbonic, aqueous, liquid-rich (type 3) FIs (Sample 11). (f) Aqueous, liquid-rich type 3 FIs in huebnerite (Sample 8). (g) Infrared photomicrograph of a cluster of irregularly shaped aqueous, liquid-rich type 3 FIs in pyrite (Sample 27). (h) Aqueous, liquid-rich type 3 FIs in fluorite showing high liquid to vapor ratio (Sample 16).

2.4.2 Fluid inclusion microthermometry

Microthermometric measurements of FIs were performed on early-stage quartz, fluorite, huebnerite, pyrite, and sphalerite samples from six different locations in the DCP (1, 5, 8, 14, 27, and 29 in Fig. 6a). The results are shown in Fig. 10 and Appendix Table 2. In general, type 1 FIs (e.g., Fig. 9a) show homogenization of CO_2 followed by total homogenization to the liquid phase or to the vapor phase. In contrast, type 2 FIs always show homogenization to vapor. It was commonly impossible to measure the final homogenization temperatures (T_h) in vapor-rich type 1 and 2 FIs due to decrepitation. Type 3 FIs always showed vapor to liquid homogenization during heating runs. A first melting temperature (T_e) was only observed in a few FIs hosted in fluorite and sphalerite. The T_e values for fluorite-hosted inclusions are between -28 and -26°C, lower than those measured in FIs hosted in sphalerite (-25.5 to -17.5°C). Melting of clathrate was observed in type 1 FIs, whereas in type 2 and in most of the type 3 FIs, either melting of ice or clathrate was observed. Both ice and clathrate melting temperatures, could be observed only in some type 3 FIs hosted in sphalerite.

Fluorite associated with molybdenite in fracture-fill mineralization (sample 14, Fig. 10) dominantly contains CO_2-bearing type 3 FIs as indicated by frequently observed melting of clathrate and the presence of CO_2 peaks in Raman spectra. The salinity varies between 5.8 and 10.4 wt.% equiv. NaCl. Values of T_h for primary FIs hosted in fluorite that is directly intergrown with molybdenite range between 320 and 337°C, whereas primary FIs in fluorite from the outer rim of the sample (i.e., distal from the molybdenite) show lower T_h values between 271 and 299°C (Fig. 10 and Appendix Table 2).

Only one FIA was measured in fluorite of sample 1 (Fig. 10). Type 1 FIs in this sample (T_h and salinities of 316-338°C and 1.6 wt.% equiv. NaCl, respectively) show both CO_2 homogenization of the liquid to the vapor phase, as well as vice versa, at temperatures between 30.3 and 30.5°C, which is close to the critical temperature of CO_2 (Fig. 9 a).
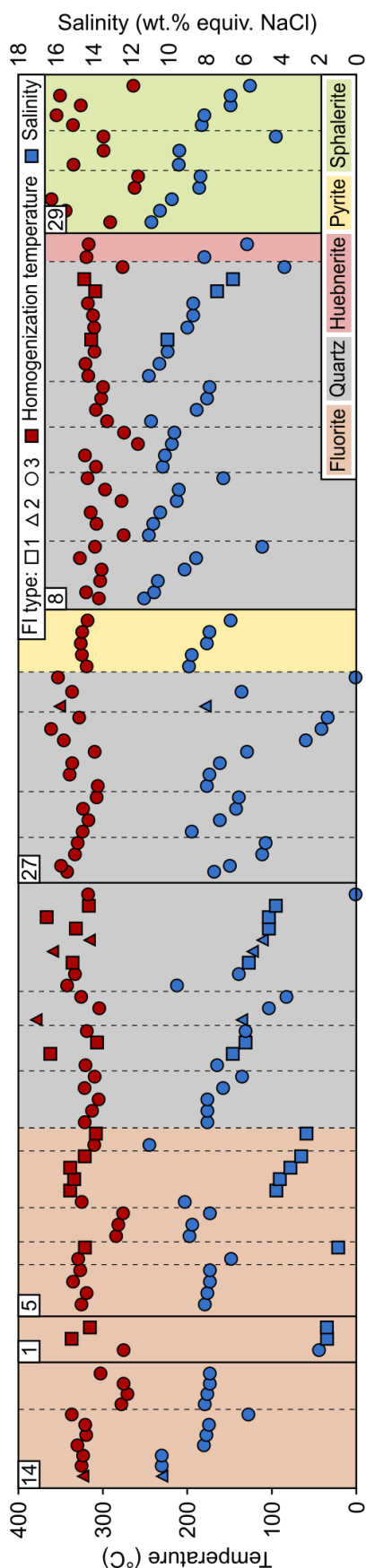
Figure 10 Homogenization temperatures (red symbols) and salinities (blue symbols) of fluid inclusions in different ore and gangue minerals from the Detroit City portal of the Sweet Home mine, Colorado. Numbers refer to individual samples (locations of the samples 1, 5, 8, 14, 27, and 29 are shown in Fig. 6a). FIAs in different minerals are separated by dashed lines. Color codes refer to different minerals and symbols to FI types. For each assemblage, data are plotted in order of decreasing salinity to the right.

Similar observations were made in sample 5, where nine FIAs in total were measured in fluorite and cogenetic quartz (Fig. 10). The fourth FIA in quartz of sample 5 shown in Fig. 10 is the only one that includes cogenetic type 1, 2, and 3 FIs (the latter commonly showing clathrate melting). In this assemblage, T_h values vary between 315 and 367°C and salinities range between 4.3 and 9.6 wt.% equiv. NaCl.

Sample 27 contains FIAs in cogenetic quartz and pyrite. In general, T_h values (307-362°C) and salinities (mainly between 4.9 and 9.0 wt.% equiv. NaCl) are similar in both minerals. The same holds for FIs in sample 8, where FIs in cogenetic quartz and huebnerite mostly show T_h values between 296 and 328°C and salinities between 5.1 and 11.3 wt.% equiv. NaCl (Fig. 10). The microthermometric data of FIs in sphalerite (sample 29) are more variable than in the other minerals. Values of T_h range between 260 and 361°C and salinities vary from 4.3 to 11.0 wt.% equiv. NaCl. The CO_2 contents of these FIs are also variable, as some show clathrate melting, whereas others do not. It is noteworthy that sphalerite is the only studied mineral where both melting of ice and clathrate were observed in individual FIs.

In summary, there are no systematic differences in the microthermometry data between gangue minerals (fluorite and quartz) and associated ore minerals (pyrite, huebnerite, and sphalerite).

2.4.3 Laser Raman spectroscopy

CO_2 was the only gas species detected in Raman spectra from vapor-rich type 1 and 2 FIs and in gas bubbles from type 3 FIs (Appendix Table 2). Solid crystals of anhydrite and calcite were identified in some FIs. Since no melting or dissolution behavior was observed during heating, it is likely that these solids were accidentally trapped (Fig. 9c, d).

2.4.4 Fluid inclusion hydrogen and oxygen isotopic composition

The results of fluid inclusion hydrogen and oxygen isotope analysis are presented in Fig. 11 and Appendix Table 3. With δ^2H_w values from -70 to -50‰ and $\delta^{18}O_w$ values from -2.0 to 7.6‰, FIs in samples of early-stage pyrite plot into or slightly to the left of the primary magmatic water box (Taylor 1974). Fluid inclusions in early-stage fluorites show more variable δ^2H_w and $\delta^{18}O_w$ values than those hosted in early-stage pyrite, but they plot on the same trend line between magmatic and meteoric water (Fig. 11). Inclusions in early-stage quartz yields lower δ^2H_w and $\delta^{18}O_w$ values (from -114.3 to -94.8‰ and from -13.1 to -10.0‰, respectively), which plot at the end of the trend line close to the meteoric water line (GMWL; Craig 1961). Early-stage huebnerite samples give remarkably low δ^2H_w values from -150.5 to -133.5‰, which differ from all other studied minerals (Fig. 11).

The δ^2H_w values of FIs hosted in galena (from -115.7 to -86.1‰), tetrahedrite-tennantite (from -122.0 to -106.0‰), and chalcopyrite (from -99.2 to -91.5‰) from the main sulfide stage are generally lower than those in early-stage minerals, whereas the $\delta^{18}O$ values do not differ significantly. Altogether, the δ^2H_w and $\delta^{18}O_w$ data of samples from the main sulfide stage plot along a trend line that is approximately parallel to the early-stage mineral trend line (Fig. 11).

Main sulfide-stage quartz and late-stage rhodochrosite and fluorite consistently yield δ^2H_w and $\delta^{18}O_w$ values plotting close to the meteoric water line.

It must be noted that oxygen-bearing minerals, such as quartz, huebnerite, and rhodochrosite, may have experienced a post-depositional depletion in ^{18}O due to low-temperature isotope re-equilibration (e.g. Rye and O'Neil 1968; Uemura et al. 2020). Thus, the original $\delta^{18}O_w$ value of these minerals may have been higher, and caution must be paid when interpreting the measured data.
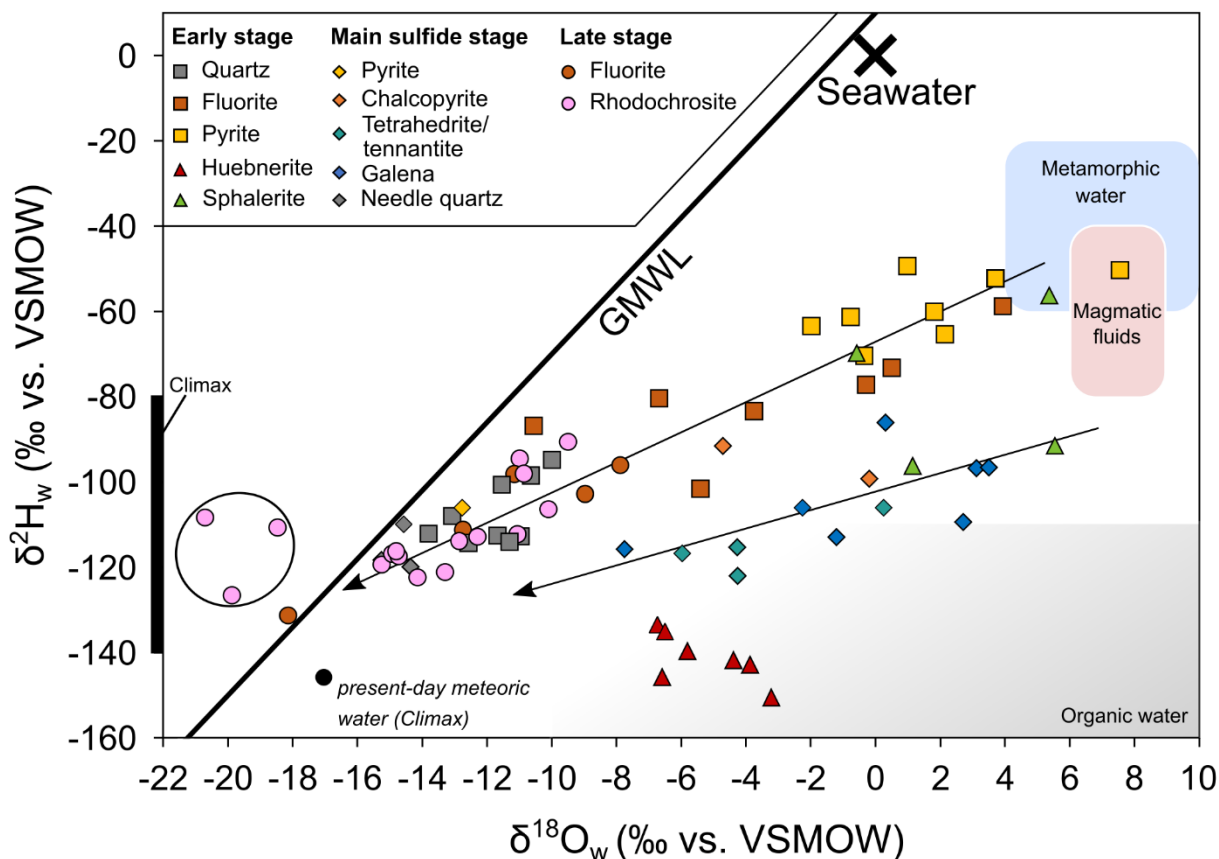
Figure 11 Fluid inclusion hydrogen and oxygen isotope data of early-, main sulfide- and late-stage ore and gangue minerals from the Detroit City portal of the Sweet Home mine, Colorado. Arrows represent possible fluid evolution paths, indicating the existence of at least two distinct fluid reservoirs and fluid mixing. The global meteoric water line (GMWL), which expresses the relation between δ^2H_w and $\delta^{18}O_w$ in natural terrestrial waters as a global average (Craig 1961), the metamorphic and magmatic boxes (Taylor 1974), the organic water box (Sheppard 1986), as well as a previously published δ^2H_w range from FIs in quartz and fluorite samples of different mineralization stages and present-day meteoric water from Climax (Hall et al. 1974) are shown for reference. The circle on the left side marks rhodochrosite samples, of which the $\delta^{18}Ow$ value is likely not primary and originally could have been higher. In general, fluid inclusions in oxygen-bearing minerals may experience a post-depositional depletion in ^{18}O due to temperature-forced isotope re-equilibration and therefore must be interpreted with care.

2.4.5 $\delta^{13}C_{CO2}$ of fluid inclusion gas and carbon and oxygen isotope ratios of rhodochrosite

The carbon isotopic composition of CO_2 from FIs in early-stage fluorite and quartz as well as the carbon and oxygen isotopic compositions of rhodochrosite are shown in Fig. 12 and Appendix Table 3. The CO_2 of FIs in early-stage fluorite and quartz has $\delta^{13}C_{VPDB}$ values between -7.2 and -3.3‰ (mean -5.5‰).

The majority of DCP rhodochrosites and the gemmy rhodochrosites from the former SHP (Lüders et al. 2009) yielded a narrow range of $\delta^{13}C_{VPDB}$ values between -8.0 and -9.2‰, which are lower than the FI range (Figure 12). The $\delta^{18}O_{VSMOW}$ values of rhodochrosites from the DCP and the former SHP are similar and both show a wider range of between 0.9 and 13.9‰.
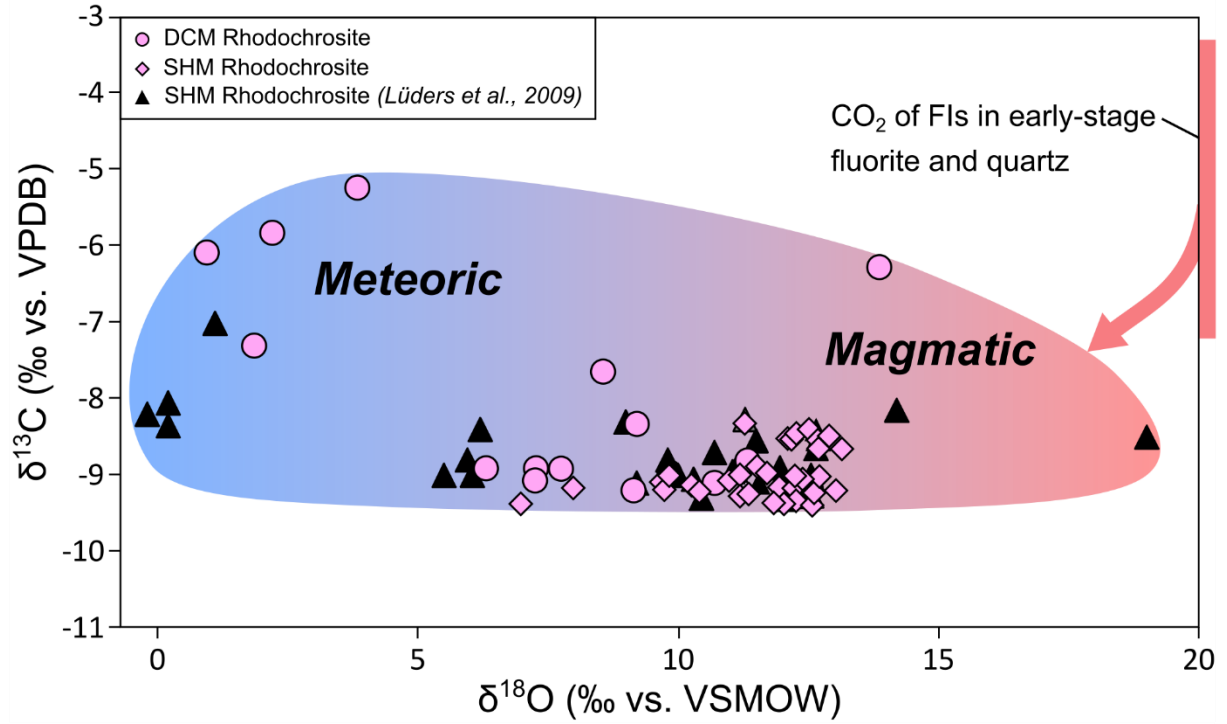
Figure 12 Carbon and oxygen isotopic composition of rhodochrosite from the Detroit City portal of the Sweet Home mine, also showing literature C and O isotope values of rhodochrosite from the Sweet Home mine (Lüders et al. 2009). The range of CO_2 carbon isotope composition of fluid inclusions in Detroit City portal early-stage fluorite and quartz is shown for comparison.

2.4.6 Noble gas elemental and isotopic composition

The results of noble gas analyses of crush-released fluids in ore and gangue minerals from the DCP are shown in Fig. 13 and Appendix Table 4.

2.4.6.1 Helium isotopic composition, He/Ne, and He/Ar ratio

Early-stage milky quartz samples (with $^4He/^{36}Ar$ from 1.2 to 13 and $^4He/^{20}Ne$ from 1.7 to 9.0) and main sulfide-stage quartz (with $^4He/^{36}Ar = 31$ and $^4He/^{20}Ne = 57$) are closest to the atmospheric values of these ratios (Fig. 13a). All other samples show values up to more than three orders of magnitude higher than the atmospheric value.

The $^3He/^4He$ versus $^4He/^{20}Ne$ plot shows that all SHM samples yielded a range of $^3He/^4He$ ratios between 0.43 and 4.3 Ra, with quartz and huebnerite from the same sample giving the lowest values of 0.43 and ~0.6 Ra, respectively (Fig. 13b). The $^3He/^4He$ ratio of late purple fluorite (0.92 Ra) is also slightly lower than the atmospheric value. The ratios of other early-stage quartz (~1.8 Ra) and fluorite samples (2.16 Ra), as well as main sulfide-stage quartz (~2.7 Ra) and late-stage rhodochrosite samples (3.03 Ra) are intermediate. Sulfide minerals including sphalerite, galena, and tetrahedrite-tennantite samples yielded a narrow range (3.1-3.5 Ra) with a low outlier for chalcopyrite (2.3 Ra) and a high value for early-stage pyrite (4.3 Ra). Except for early-stage quartz ($^4He/^{20}Ne$ = 1.7), all minerals yield $^4He/^{20}Ne$ ratios >9 and up to 13,400 (huebnerite). The atmospheric He contribution is thus generally <3.5%.

Figure 13c presents the ratio of ^4He to excess radiogenic $^{40}Ar^*$, after correction for atmospheric argon with $^{40}Ar/^{36}Ar$ = 298.56 (Lee et al. 2006). The $^4He/^{40}Ar^*$ of the huebnerite sample (17) is at least a factor of two higher than the normal production ratios (resulting from U, Th, and K decay) of 1–3 in the crust and 2–8 in the mantle (Ozima and Igarashi 2000). All sulfide samples, including early-stage pyrite, as well as early- and late-stage fluorite and rhodochrosite yielded typical crustal $^4He/^{40}Ar^*$ ratios In contrast, both early-stage quartz samples gave $^4He/^{40}Ar^*$ ratios two orders of magnitude below the typical production ratio, and the main sulfide-stage quartz gave a ratio one order of magnitude smaller.

2.4.6.2 Neon isotopic composition

Figure 13d shows $^{20}Ne/^{22}Ne$ versus $^{21}Ne/^{22}Ne$, including characteristic trajectories for MORB (Sarda et al. 1988), OIB (Honda et al. 1991), average crust with O/F = 752 (oxygen and fluorine elemental ratio) (Hünemohr 1989), the production of nucleogenic ^{22}Ne in U- and Th-bearing fluorite, and the (air) mass fractionation line. Due to the small deviations from atmospheric composition, error bars are relatively large and thus interpretations should be made with care. Nevertheless, early-stage pyrite and later chalcopyrite show the highest $^{20}Ne/^{22}Ne$ ratios (10.14 and 10.10, respectively), with $^{21}Ne/^{22}Ne$ values (0.0296 and 0.0295, respectively), close to the air ratio plotting on the air mass fractionation line. Most other ore minerals including huebnerite, sphalerite, tetrahedrite, and galena plot in a wide range between MORB and crustal values. The gangue minerals (quartz, fluorite and rhodochrosite of all stages) tend to plot closer to the atmospheric $^{20}Ne/^{22}Ne$ and $^{21}Ne/^{22}Ne$ ratios (9.8 and 0.029, respectively) with $^{20}Ne/^{22}Ne$ ranging between 9.8 and 9.9 and $^{21}Ne/^{22}Ne$ between 0.029 and 0.031.

2.4.6.3 Argon isotopic composition

The $^{40}Ar/^{36}Ar$ ratios are highly variable between air-like (296, e.g. Ozima and Podosek 2002) and a maximum value of 1876, indicating variable crustal or mantle contributions (Appendix Table 4). Early-stage pyrite and main sulfide-stage chalcopyrite have $^{40}Ar/^{36}Ar$ ratios close to the atmospheric value. They are followed by higher ratios of the late-stage fluorite, early-stage quartz, rhodochrosite, main sulfide-stage quartz, and early-stage fluorite with $^{40}Ar/^{36}Ar$ ratios between 388 and 574. Early-stage quartz from the huebnerite sample, however, yielded the highest $^{40}Ar/^{36}Ar$ ratio of 1876. Huebnerite, tetrahedrite-tennantite, galena, and sphalerite gave intermediate $^{40}Ar/^{36}Ar$ values between 574 and 1350.
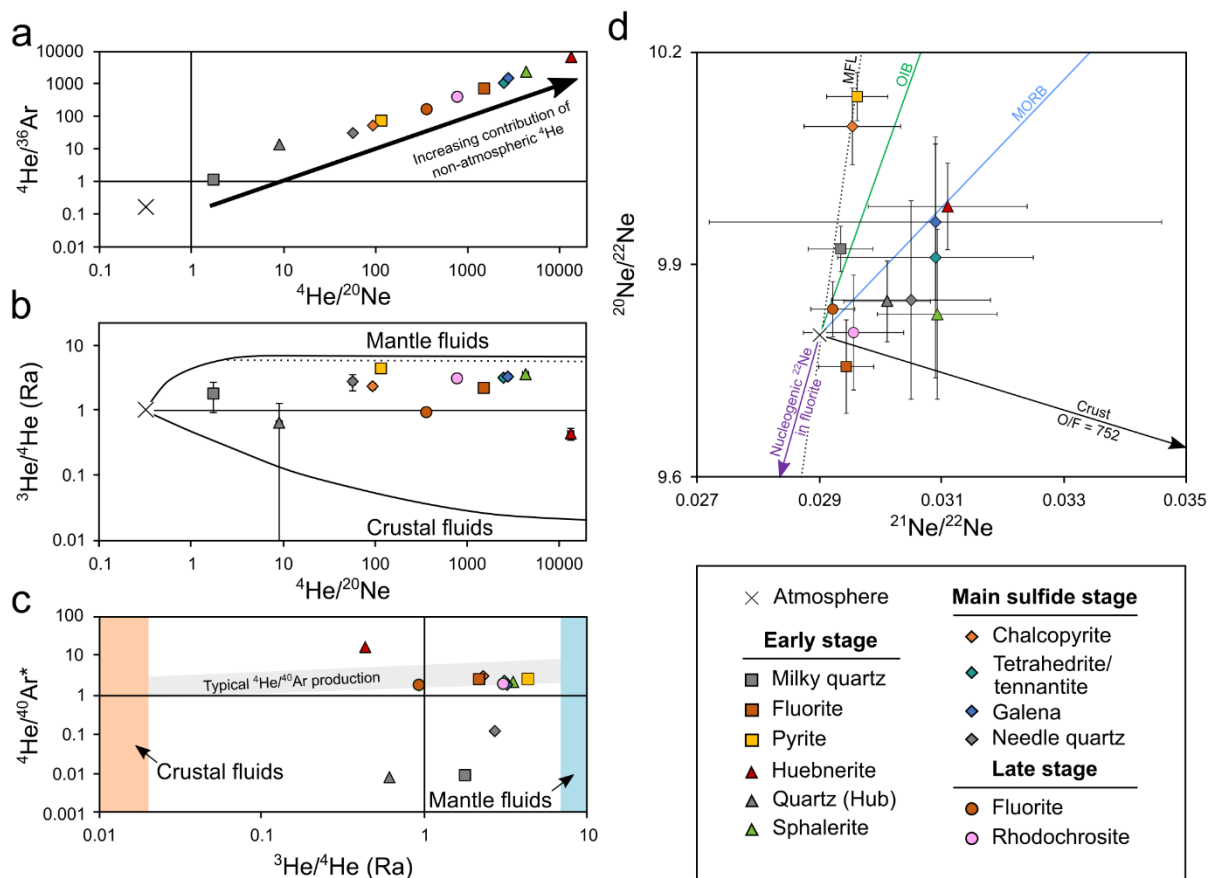
Figure 13 Noble gas isotopic compositions of gases extracted from fluid inclusions in early –, main sulfide- and late-stage ore and gangue minerals from the Detroit City portal of the Sweet Home mine, Colorado. Early-stage quartz that is intergrown with huebnerite is displayed as "Quartz (Hub)". (a) $^{4}He/^{36}Ar$ versus $^{4}He/^{20}Ne$ plot. A correlation from the atmospheric ratios ($^{4}He/^{36}Ar = 0.168$ and $^{4}He/^{20}Ne = 0.319$) to values up to four orders of magnitude higher reflects the increasing contribution of non-atmospheric (mantle or crustal) ^{4}He. (b) $^{3}He/^{4}He$ versus $^{4}He/^{20}He$ plot (Ra is the atmospheric ratio of 1.39×10^{-6}). Characteristic $^{3}He/^{4}He$ ratios of terrestrial reservoirs (1 Ra for the atmosphere, 0.02 Ra for crustal fluids, 6.1 Ra for subcontinental lithospheric mantle (black dotted line), and >7 Ra for shallow depleted and primitive mantle-derived fluids) are also indicated. (c) $^{4}He/^{40}Ar*$ versus $^{3}He/^{4}He$ plot. $^{4}He/^{40}Ar*$ is a measure of the production ratio of ^{4}He from U and Th decay to $^{40}Ar*$ (* denotes correction for atmospheric ^{40}Ar) from ^{40}K decay. Only huebnerite shows anomalously high $^{4}He/^{40}Ar*$ and only quartz samples anomalously low $^{4}He/^{40}Ar*$. All other minerals plot in the typical production range. (d) $^{20}Ne/^{22}Ne$ versus $^{21}Ne/^{22}Ne$ plot.

The lines that extend away from the Atmosphere reflect mass fractionation (MFL; black dotted line), nucleogenic ingrowth in the crust with O/F = 752 (black arrow), production of nucleogenic ^{22}Ne in U- and Th-bearing fluorite (purple arrow), or addition of mantle neon from the oceanic island (OIB; green line) and mid-ocean ridge basalts (MORB; blue line). See text for data sources.

2.4.6.4 Noble gas elemental abundances

Heavy noble gas elemental abundances are useful to test for isotopic equilibrium at the ca. 250–330°C mineralization temperature indicated by fluid inclusions. Elemental fractionation factors ($F_i=(^iX/^{36}Ar)_{sample}/(^iX/^{36}Ar)_{air}$, where $^iX=^{20}Ne$, ^{84}Kr or ^{132}Xe) are compared with those for air-saturated water calculated for temperatures from 0 to 330°C (Crovetto et al. 1982; Smith and Kennedy 1983). The results are displayed in Appendix Fig. 5, with Appendix Fig. 5a showing early-stage mineral data and Appendix Fig. 5b main sulfide- and late-stage mineral data. Helium isotope data are not displayed as they are dominated by non-atmospheric components and would plot well above the shown range. In all samples, Ne abundances are too high for equilibrium at the mineralization temperature. On the other hand, early-stage quartz, pyrite, huebnerite and sphalerite, and main sulfide-stage chalcopyrite and rhodochrosite do plot along the Kr equilibrium curves for 250 and 330°C. This is also true for the Xe 250°C equilibrium curve, regarding early-stage pyrite. Generally, however, most samples do not plot on heavy noble gas equilibrium curves, which may be related to the fact that >100°C fractionation curves (Crovetto et al. 1982) only apply to freshwater and do not consider salinities. Nevertheless, the fractionation plots show that the heavy noble gases have a significant non-magmatic component.

2.4.7 Sulfur isotopic composition

Sulfide minerals from the DCP yielded $\delta^{34}S$ values between -3.4 and +1.6‰ (Fig. 14, Appendix Table 5). The highest $\delta^{34}S$ values were measured in early-stage pyrite (0.9 to 1.6‰) and molybdenite (1.3 to 1.4‰). Sphalerite from the late greisen stage and pyrite from the main sulfide stage gave slightly lower $\delta^{34}S$ values (0.3 to 1.2‰), and the ranges for the other main sulfide-stage sulfides overlap between -3.4 and +0.2‰.
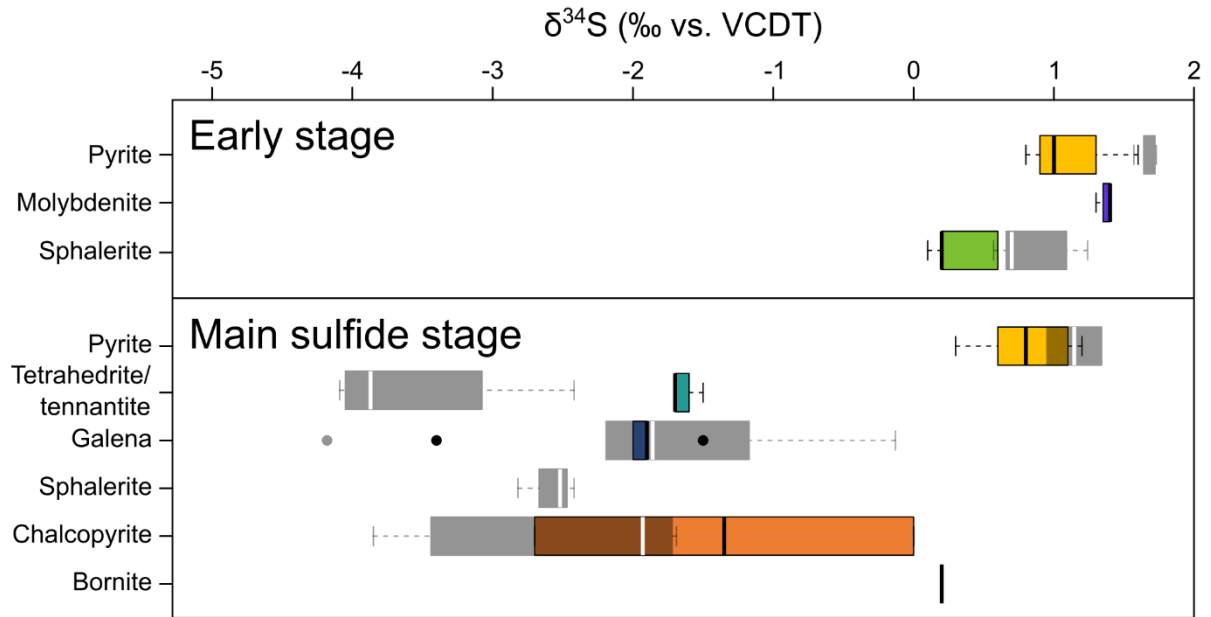
Figure 14 Boxplot showing sulfur isotopic compositions of Detroit City portal (colored boxes with black contours) early- and main sulfide-stage sulfides. Sweet Home mine data (grey boxes) of Lüders et al. (2009) are shown for comparison.

2.5 Interpretations

2.5.1 P–T conditions of fluid entrapment in quartz and fluorite from the early stage

The early-stage mineralization of the SHM formed from fluids with salinities up to 12 wt.% equiv. NaCl in the presence of CO_2. Values of T_h for FIs hosted in fluorite and quartz average at about 320°C. Solvi and isochores of individual carbonic three-phase type 1 FIs were calculated using the computer program "Fluid inclusions in the system H_2O-NaCl-CO_2: An algorithm to determine composition, density and isochore" by Steele-MacInnis (2018). The results show that the majority of these FIs were trapped at temperatures between 360 and 415°C and pressures between 1050 and 1750 bar (Appendix Fig. 6). Similar P-T conditions were estimated for carbonic three-phase type 1 FIs from the former SHM workings and interpreted as a result of an originally homogeneous fluid intersecting the solvus during cooling or decompression (Lüders et al. 2009). This may be supported by the relatively narrow range in composition of carbonic three-phase type 1 FIs (Lüders et al. 2009, this study), suggesting that the P-T fluid pathway intersected the solvus near its crest, where the composition of the two immiscible phases did not differ

significantly if immiscibility occurred (Bodnar et al. 1985; Diamond 1994). Alternatively, a fluctuating pressure regime from lithostatic to hydrostatic conditions or fluid entrapment from heterogeneous mixtures of two fluids of different origins may explain the phase transitions of Type 1 inclusions to the liquid phase or to the vapor phase (Lüders et al. 2009) (Fig. 9a).

2.5.2 Fluid inclusion hydrogen and oxygen isotopic composition

Variations of δ^2H_w and $\delta^{18}O_w$ in fluid hosted by different minerals are interpreted to reflect different mixing trends between a magmatic fluid and meteoric water (Fig. 11 and Appendix Table 3). The conspicuously low δ^2H_w values of early-stage huebnerite samples may point to an organic-rich fluid source (Sheppard 1986). The δ^2H_w and $\delta^{18}O_w$ data also suggest the cessation of the magmatic fluid input during the late mineralization stage (i.e. pink rhodochrosite, purple fluorite).

2.5.3 $\delta^{13}C_{CO2}$ of fluid inclusion gas and carbon and oxygen isotope ratios of rhodochrosite

The $\delta^{13}C_{CO2}$ values of type 1 aqueous carbonic, and type 2 vapor-rich CO_2 FIs in early quartz and fluorite suggest that carbon was derived from a magmatic source (Hoefs 2018 and references therein). The slightly lower $\delta^{13}C$ of rhodochrosites compared to $\delta^{13}C_{CO2}$ values of FI gas can be explained by temperature-dependent carbon isotope fractionation between CO_2 and carbonates (Hoefs 2018 and references therein). Whereas $\delta^{13}C$ values of rhodochrosite are relatively constant, the $\delta^{18}O$ data are more variable and suggest mixing of magmatic and meteoric fluids (Fig. 12).

2.5.4 Noble gases

While the noble gas data are complex, they indicate that the atmospheric helium contribution was generally less than 3.5% (Fig. 13a, b). Neon (Fig. 13d) and argon isotopic

compositions (Appendix Table 4), however, may represent variable mixtures of atmospheric, crustal, and mantle components and are additionally affected by minor mass fractionation.

The ^{3}He/^{4}He ratios span a relatively broad range between the crustal and mantle endmembers, however mostly closer to the mantle field, which indicates mixing of different fluid sources (Fig. 13b).

Fluid inclusions hosted in huebnerite from the DCP, however, dominantly show ^{3}He/^{4}He and ^{4}He/^{40}Ar* ratios that are typical for, or may be explained by, crustal fluids (Fig. 13b and Fig. 13c, respectively). Anomalously high ^{4}He/^{40}Ar* ratios may indicate production in a high (U+Th)/K environment or fractionation of He and Ar, e.g. by melt formation, degassing, solution (temperature dependent) or diffusion, in an upper crustal reservoir (Ozima and Podosek 2002). Rocks enriched in uranium, such as organic-rich sedimentary rocks or granites and granitic gneisses, are present in the study area as discussed in more detail in the following chapter. All sulfides, including early-stage pyrite, as well as early- and late-stage fluorite and rhodochrosite plot in the range of typical crustal ^{4}He/^{40}Ar* ratios and thus may indicate closed system conditions with respect to noble gases (Ozima and Podosek 2002). The ^{4}He/^{40}Ar* ratios of FIs in quartz samples are smaller than the range of typical production ratios, indicating He loss (Fig. 13c).

2.5.5 Sulfur isotopic composition

The isotopic variation of sulfur can depend on changes in physico-chemical conditions or mixing of sulfur from distinctly different sources (Ohmoto and Rye 1979). Assuming ore-formation temperatures of at least 400°C for early-stage sulfides, such as molybdenite, pyrite and sphalerite (Lüders et al. 2009; this study), the calculated initial δ^{34}S values of the ore fluid would range within 0 and 0.9‰ and may point to a homogeneous (probably magmatic) sulfur source (Ohmoto and Rye 1979). For ore minerals of the main sulfide stage that precipitated at lower temperatures (ca. 300°C; Lüders et al. 2009) the calculated range of δ^{34}S values is considerably larger (from 1.8 to -3.7‰; Ohmoto and Rye 1979). The calculated ranges confirm the overall trend of the δ^{34}S raw data (Fig. 14).

Assuming a homogeneous (probably magmatic) sulfur source for sulfides that precipitated during the early stage and main sulfide stage, significant changes in fO_2 and pH would have been required to explain the variation of δ^{34}S values of sulfides during ore deposition (Ohmoto and Rye 1979). At low fO_2 and pH values the δ^{34}S values of sulfides will not show significant fractionation compared to the initial δ^{34}S value of the fluid. In contrast, at high fO_2 values the δ^{34}S values of sulfides differ significantly from the initial δ^{34}S value of the ore fluid and the proportions of aqueous sulfate in the fluid increases (Ohmoto and Lasaga 1982). Given that sulfates are absent

but rhodochrosite is abundant in the main sulfide stage, significant changes of fO_2 and pH may be precluded and we assume a homogeneous fluid source. Therefore, the decreasing $\delta^{34}S$ values of the sulfides from the main sulfide stage are best explained by mixing of sulfur from different sources. These can be magmatic and sedimentary sulfur sources, the latter covering a wider range, especially for organic-rich sediments that may have negative $\delta^{34}S$ values (Hoefs 2018 and references therein).

2.6 Discussion

The results of this study are not compatible with an exclusive magmatic origin of deep hydrothermal vein-type mineralization for Climax-type ore deposits in the CMB as proposed by previous research (Wallace et al. 1978; Mutschler et al. 1981; Westra and Keith 1981; White et al. 1981; Stein and Hannah 1985; Bookstrom et al. 1988; Carten et al. 1988; Stein 1988; Carten et al. 1993; Keith et al. 1993; Cline and Bodnar 1994; Lowenstern 1994; Wallace 1995; Seedorff and Einaudi 2004a; 2004b; Klemm et al. 2008; Ludington and Plumlee 2009; Audétat 2010; Pettke et al. 2010; Audétat et al. 2011; Audétat 2015; Mercer et al. 2015; Audétat and Li 2017). Instead, the new data reported here from FI studies and stable isotope analysis of FIs, sulfides, and rhodochrosite give compelling evidence for variable mixing proportions of magmatic fluids with heated meteoric water during the evolution of the hydrothermal system at the DCP. This includes early-stage greisen and pyrite veins as well as greisen and phyllic alteration assemblages (i.e. fluorite, quartz, pyrite, huebnerite and sphalerite), main sulfide stage mineral assemblages (i.e. base metal sulfides and rhodochrosite) as well as late-stage mineralization (i.e. rhodochrosite and fluorite). Mixing models of magmatic and meteoric water have also been proposed by previous FI studies of Climax-type Mo deposits and associated hydrothermal systems (Hall et al. 1974; Bloom 1981; Smith 1983; Lüders et al. 2009; Rowe 2012).

2.6.1 Fluid inclusion characteristics of Climax-type Mo deposits

Studies of FIs in quartz and fluorite from Climax-type deposits (Climax, Hall et al. 1974; Questa, Bloom 1981; Smith 1983; Cline and Bodnar 1994; Klemm et al. 2008; Rowe 2012; Henderson, White et al. 1981; Seedorff and Einaudi 2004b) show great similarities in FI types. In

general, four major types of FIs can be classified (Table 2). These are: i) Carbonic three-phase, low-salinity to intermediate-salinity (130-400°C, 0-10 wt.% equiv. NaCl), ii) vapor-rich, low- to high-salinity (300-500°C, 0-20 wt.% equiv. NaCl), iii) liquid-rich, low- to high-salinity (300-500°C, 0-25 wt.% equiv. NaCl) and iv) multi-phase hypersaline (180-450°C, 30-65 wt.% equiv. NaCl) FIs. Although type 4 FIs have not been observed in studied minerals from the SHM (Reynolds 1998; Lüders et al. 2009; this study), type 1 to type 3 FIs are analogous to those observed in other Climax-type systems and their abundance suggests a similar fluid source and mechanism for ore formation at Climax-type deposits and the SHM. Whereas type 3 FIs are hosted in minerals from all ore stages of Climax-type deposits, type 1, 2, and 4 FIs are restricted to the main stage of Mo-mineralization (quartz-molybdenite stockwork veins, magmatic-hydrothermal breccias with a quartz-fluorite matrix, potassic alteration) and subsequent Mo-mineralization (phyllic and greisen alteration and veins). Mo-bearing greisen veins, which are typically found inside intrusive porphyry complexes, also occur in distal deep hydrothermal veins at the DCP.

Our data show that CO_2 contents of vapor-rich, CO_2-bearing FIs, liquid CO_2-bearing FIs, and liquid-rich FIs may vary considerably within the same assemblage, whereas evidence for phase separation is lacking. Based on elevated Cu contents in FIs and depletion in other metals, Lüders et al. (2009) suggested that phase separation may have occurred at greater depth beneath the actual Sweet Home workings. Boiling at depth would also explain the absence of halite-bearing type 4 FIs in minerals from vein-type mineralization of the SHM.

2.6.2 Fluid mixing

The mixing of magmatic fluids with meteoric water forming the early-stage greisen and pyrite veins as well as greisen and phyllic alteration, the main sulfide stage veins as well as late-stage mineralization at the SHM is evidenced by well-defined trends of fluid inclusion and bulk mineral isotope data. Note that all studied samples were carefully evaluated for fluid inclusion petrology prior to bulk analysis to avoid contamination by abundant secondary inclusions (for details see "Reliability of fluid inclusion bulk analysis" section of the "Samples and analytical methods" chapter). Fluid inclusion water in pyrite samples from early-stage mineralization plots in or close to the primary magmatic fluid box (Taylor 1974), while combined hydrogen and oxygen isotope compositions of fluid inclusions hosted in early-stage quartz and fluorite (locally associated with molybdenite) and later sulfides follow a mixing trend of magmatic fluids with meteoric water (Fig. 11). A similar evolution of hydrogen and oxygen isotope ratios of FIs was observed at the Questa rhyolitic porphyry Mo deposit (New Mexico) and interpreted in terms of a mixing model of early magmatic fluids that were progressively diluted by meteoric water (Rowe

2012). Alternatively, several alteration processes (e.g. exchange reactions, hydration reactions, membrane filtration) may be responsible for the variation of H and O isotopes (e.g. Hoefs 2018 and references therein). However, given the lower sensitivity of H isotopes to alteration processes (e.g. Hoefs 2018 and references therein), our preferred interpretation is mixing of different sources for the mineralizing fluids.

The mixing of fluids from different sources is supported by $\delta^{13}C_{CO2}$ values of FIs in quartz and fluorite from the early stage and slightly lower $\delta^{13}C$ of rhodochrosites, indicating a magmatic carbon source, as well as by the more variable $\delta^{18}O$ data, suggesting a mixed magmatic-meteoric origin. A magmatic carbon source, but mixed magmatic-meteoric oxygen source was also proposed for calcite at Questa (Rowe 2012).

The sulfur isotopic composition of SHM sulfides and sulfosalts show a development from homogeneous magmatic $\delta^{34}S$ values in the early stage towards more variable $\delta^{34}S$ values in the main sulfide stage. This trend may reflect a mixed magmatic-sedimentary source. There are similar findings from polymetallic vein mineralization found at the Sn-W Mole Granite, Australia (Heinrich et al. 1992; Audétat et al. 2000). Lüders et al. (2009) showed that there is a correlation between decreasing $\delta^{34}S$ values and increasing $^{206}Pb/^{204}Pb$ in galena, which was explained by fluid/rock interaction between meteoric fluids and crustal rocks. Furthermore, it is conspicuous that the sulfides with lower $\delta^{34}S$ values from the main sulfide stage also yield lower $\delta^{2}H_w$ values of FI water than sulfides from the early stage, which either suggests multiple fluid sources or (minor) variations in $\delta^{2}H_w$ and $\delta^{18}O_w$ values of the magmatic fluid endmember with time.

Progressive dilution of magmatic fluids enriched in volatiles (CO_2, H_2S, noble gases) by increasing amounts of meteoric water from the early to the late stage of mineralization is consistent with the continuously decreasing temperatures, pressures, CO_2 concentrations, and variations in noble gas and C, O, H, and S isotope ratios. The progressive mixture of CO_2-poor meteoric fluids into the system may explain why liquid CO_2-bearing FIs exclusively occur in early-stage minerals and are not observed in ore and gangue minerals of the subsequent sulfide stage (Reynolds 1998; Lüders et al. 2009). The absence of detectable CO_2 in FIs with progressive mineralization was also reported from many Chinese Mo deposits (e.g., Yang et al. 2015; Zhou et al. 2015; Zhang et al. 2016; Xiong et al. 2018).

2.6.3 The magmatic input

Considering a progressive development towards lower $\delta^{34}S$ values from pyrite of the early stage to younger sulfides of the main sulfide stage, the highest $\delta^{34}S$ values around 1.7‰ measured in early-stage minerals may represent the magmatic sulfur value (Ohmoto and Rye 1979), which

was already concluded for other Climax-type deposits (Stein and Hannah 1985; Stein 1988; Rowe 2012). Due to the low sulfur solubility in rhyolitic melts (Wallace and Edmonds 2011), it was proposed that the sulfur from the Henderson rhyolitic porphyry Mo deposit (Colorado) originated from a relatively small volume of underlying mantle-derived lamprophyre magma (Mercer et al. 2015). Over the last decades, bimodal magmatism with a mantle contribution was considered to be a likely source for melts associated with the formation of Climax-type Mo deposits during continental rifting (Westra and Keith 1981; Carten et al. 1993; Keith et al. 1993; Audétat 2010; Mercer et al. 2015).

Noble gas data may be a promising tool to distinguish between possible fluid sources and this study presents the first of their kind for the CMB. Helium isotopic compositions of fluid inclusions hosted in minerals from the SHM (Fig. 13b) support the idea that magmatic fluids had a substantial mantle component (except huebnerite, which is discussed in detail in the "Fluid-rock interaction" section). The ^{3}He/^{4}He isotope ratios of FIs hosted in early-stage pyrite from the DCP are 4.3 Ra. Considering binary mixing between the subcontinental lithospheric mantle (6.1 Ra, Gautheron and Moreira 2002) and continental lithosphere (0.02 Ra, Graham 2002) with:

$$^4\text{He}_{\text{mantle}}\ (\%) = 100 \cdot \frac{\left[\left(\frac{^3\text{He}}{^4\text{He}}\right)_{\text{sample}} - \left(\frac{^3\text{He}}{^4\text{He}}\right)_{\text{crust}}\right]}{\left[\left(\frac{^3\text{He}}{^4\text{He}}\right)_{\text{mantle}} - \left(\frac{^3\text{He}}{^4\text{He}}\right)_{\text{crust}}\right]} \qquad (1),$$

a contribution of up to ~70% mantle He during the early stage and up to ~50% for the main sulfide stage at the SHM can be estimated. The dominant mantle He contributions characteristic for the mineralization at the SHM differ significantly, e.g., from mantle He contributions of 4-20% inferred for North American porphyry copper deposits (Kendrick et al. 2001) and 0.2-41% for Chinese Mo porphyry deposits (e.g., Bangpu Mo-Cu deposit, Wang et al. 2015; Daheishan and Luming Mo deposits, Zeng et al. 2018; Dasuji Mo deposit, Chen et al. 2021a). The mantle gas involved in the formation of the Chinese Mo porphyry deposits was assumed to have derived from unstable mantle flows in convergent regimes (Zeng et al. 2018) and from upwelling asthenospheric mantle in post-collisional rifts (Wang et al. 2015; Chen et al. 2021a). The latter is similar to the CMB, which was overprinted by the Rio Grande rift extension beginning ca. 33 Ma (Chapin 2012 and references therein).

Intermediate δ^{13}C values between -3.3 and -7.2‰ for CO_2 from FIs in early-stage quartz and fluorite may support a significant mantle CO_2 contribution. Continental rift zones have repeatedly been associated with unusually carbon-rich mantle-derived magmas (Bailey 1987; Bailey and Macdonald 1987; Bailey and Hampton 1990). A melt inclusion study on the Pine Grove rhyolitic porphyry Mo deposit (Utah; Lowenstern 1994) yielded CO_2 saturation pressures as high as 4300 bar, which correspond to a depth of 16 km for the beginning of volatile exsolution during ascent to depths of 2-3 km (depth of porphyry emplacement). The exsolution of a CO_2 vapor phase

from magma promotes the concentration of sulfur and noble gases (Lowenstern 2001; Scaillet and Pichavant 2005). Generally, such a vapor phase has low density (Papale and Polacci 1999). CO_2 effervescence may explain the heterogeneous supply of CO_2 to the early-stage ore-forming fluid in the SHM.

In summary, we conclude that CO_2, noble gases, and early-stage sulfur are derived by mantle degassing (e.g., of a lamprophyric intrusion at depth) rather than originating from the rhyolitic melts. This observation is in concordance with findings about the origin of S and CO_2 at the Henderson Mo porphyry deposit (Mercer et al. 2015). However, our data do not prove whether metals such as Mo, W, and base metals originate from magmatic fluids derived from rhyolitic melts or leaching of country rocks.

2.6.4 Fluid-rock interaction

Various Mo- and W-bearing lithologies have been deposited over the last 1700 Ma in the CMB. This includes several Precambrian pegmatites in the Climax area (e.g. Platte Gulch, Buckskin Gulch, and Quandrary Peak), the Precambrian Silver Plume Granite, and the metasedimentary rocks of the Idaho Springs Formation in the Urad-Henderson area as well as numerous Precambrian scheelite occurrences in calcareous hornblende-bearing layers of metamorphic rocks across the CMB (Tweto 1960; Zahony 1968; Wallace et al. 1978; Theobald et al. 1983).

Molybdenum in Climax-type ore deposits is likely directly derived from fluids that were expelled from magmas, which either formed by partial melting of lower or upper crustal rocks (Wallace et al. 1978; DePaolo 1981; Stein and Hannah 1985; Bookstrom et al. 1988; Stein 1988; Audétat et al. 2011; Mercer et al. 2015) or developed from a Mo-enriched mantle source (Westra and Keith 1981). Mixed mantle and crustal sources for the formation of Climax-type Mo deposits were also considered (White et al. 1981; Pettke et al. 2010). However, it has been shown that melt inclusions in quartz from Climax-type rhyolitic porphyry intrusions are Mo-poor with 5-10 ppm Mo mainly (Lowenstern 1994; Audétat et al. 2011; Audétat 2015; Mercer et al. 2015; Audétat and Li 2017), while the Mo content of the magmatic bulk fluid is estimated to be 100 ppm (Audétat 2015). Lowenstern (1994) and Audétat (2015) therefore suggested the exsolution of large volumes of a fluid that originated from a low-density fluid-rich magma and circulated through semi-crystallized narrow stocks and apophyses underneath the ore bodies. The focused flow of these high fluid volumes through a small rock volume is assumed to be the principal trigger for ore formation (Audétat and Li 2017).

Another mechanism for the accumulation of metals in ore fluids is the leaching of metals from country rocks. Smith (1983) considered that ore precipitation in porphyry Mo deposits

resulted from the cooling of ore-forming fluids by interaction with the country rocks. Seedorff and Einaudi (2004b) suggested selected leaching of metals, namely Na, K, and Fe, from the country rocks, whereas Mo and base metals are derived from the rhyolitic melts. In contrast, significant leaching of metals (excluding Mo) from lower crustal rocks by circulating hot fluids in the Alma district and of Early Proterozoic rocks elsewhere in the CMB was proposed based on radiogenic isotope compositions of ore and gangue minerals (Kelley et al. 1998; Lüders et al. 2009).

Alteration and leaching of crustal rocks are also evidenced by the presence of nitrogen in huebnerite-hosted FIs (Lüders et al. 2009). The authors considered that nitrogen was either derived from decrepitated FIs in the crystalline basement rocks, NH_4^+/K^+ exchange reactions during fluid-rock interaction with feldspars and/or micas at elevated temperatures and subsequent mixing with oxygen-rich meteoric waters (Honma and Itihara 1981; Pöter et al. 2004), or thermal degradation of the organic matter during diagenetic processes (Jia and Kerrich 1999; Mingram and Bräuer 2001). The latter has also been proposed for the origin of N_2 at the Logrosán Sn-W deposit in the Central Iberian Zone (Chicharro et al. 2016). The extremely negative δ^2H_w values of huebnerite-hosted FIs point to a non-(exclusive) magmatic fluid origin, possibly indicating an organic-rich source (Fig. 11). This could be shales or biotite schist, the latter is the host rock of the mineralization at the SHM. The relatively low δ^2H_w values (Fig. 11) and decreasing $\delta^{34}S$ values (Fig. 14) of sulfides from the main sulfide stage may also reflect considerable hydrogen and sulfur supply from organic-rich rocks.

Fluid inclusions hosted in huebnerite from the DCP show $^3He/^4He$ ratios that are dominated by a crustal fluid component (Fig. 13b). Leaching of uranium-bearing crustal rocks such as organic-rich sedimentary rocks or granites, which are abundant in the study area (Fig. 5), may provide the initial conditions for a higher ^4He production and the elevated $^4He/^{40}Ar^*$ ratio (Ozima and Podosek 2002). Organic-rich sedimentary rocks contain fixed immobile U(IV), in e.g. U-oxides, sulfides, or carbonates, that can be efficiently leached as soluble U(VI) by circulating fluids under oxidizing conditions (Idiz et al. 1986; Granet et al. 2007; Cuney 2010). Similarly, granites and granite gneisses in the Climax and Henderson areas contain U-bearing accessories, such as zircon, monazite, or thorite (Desborough and Sharp 1978; Desborough and Mihalik 1980), and may supply mobile U due to metamictization (e.g. Romer and Cuney 2018 and references therein). The fact that both host rocks are present in the study area also makes a combined fluid-rock interaction history possible.

2.7 Summary and conclusions

Our fluid inclusion and stable isotope studies in ore and gangue minerals from various mineralization stages of the SHM provide compelling evidence that the mineralization formed from magmatic fluids and meteoric water, which mixed to different proportions with time. The evolution of ore deposition at the Sweet Home mine is shown schematically in Fig. 15.
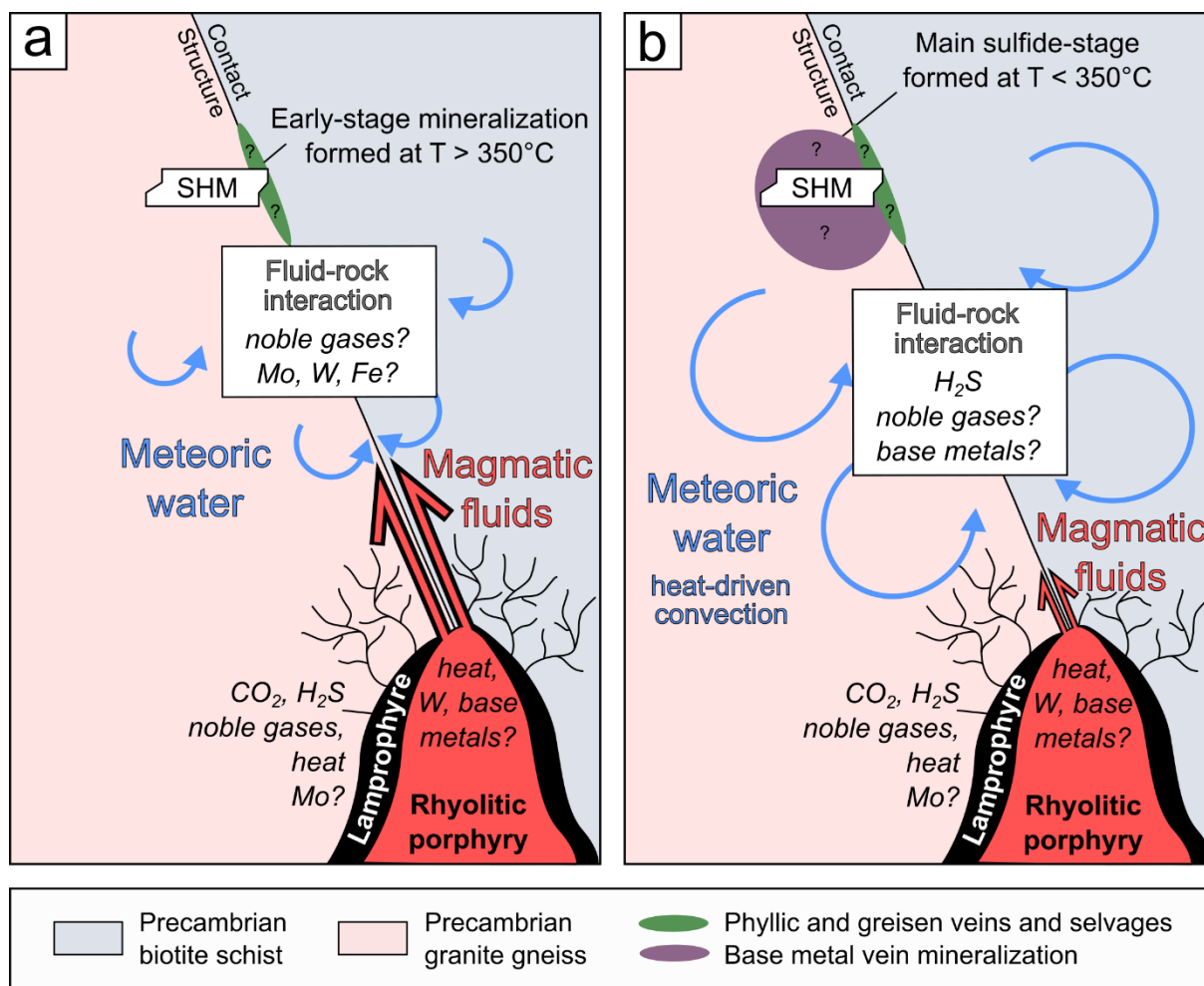
Figure 15 Schematic model of the formation of Sweet Home mine mineralization with bimodal magmatism at depth supplying both mantle-derived volatiles (i.e. CO_2, H_2S, noble gases) and heat. Mineralization formed from magmatic fluids and meteoric water, which mixed to different proportions with time. (a) Hot magmatic-hydrothermal fluids migrated along the reactivated Precambrian Contact Structure and mixed to variable proportions with meteoric water during ascent to the site of mineralization. Mixing caused fluid cooling and dilution of the magmatic fluids, and the deposition of greisen vein mineralization and phyllic alteration at temperatures above 350°C. (b) Heat propagation with time may have led to large-scale convection of meteoric water and leaching of sulfur (and possibly metals) from the crustal rocks. Progressive mixing led to a meteoric-dominated ore fluid and further cooling and dilution. Subsequently, polymetallic vein mineralization of the main sulfide stage formed at temperatures of less than 350°C.

Early-stage Mo-bearing mineralization likely formed from magmatic-dominated fluids at temperatures >400°C. Early fluid migration occurred along a reactivated Precambrian Contact

Structure during N-S-trending tectonic movements (Fig. 15a). The magmatic fluids were enriched in volatiles, such as CO_2, H_2S/SO_2, and noble gases, most likely derived from mantle sources (e.g., lamprophyric intrusion at depth). The mixing of meteoric water with magmatic fluids during the early greisen stage was minor, but increased significantly towards the main sulfide stage (Fig. 15 b). Fluid mixing caused decreasing temperature and dilution of magmatic fluids. Progressive heat-driven convection of meteoric fluids may have facilitated leaching of metals from crustal rocks and led to the formation of polymetallic vein mineralization at the SHM.

Fluid mixing of magmatic fluids with large amounts of meteoric water seems the most likely mechanism for the formation of Climax-type-related peripheral vein mineralization in the CMB. The data from this study are not sufficient to determine whether Climax-type Mo mineralization in ore shells above porphyry stocks can be attributed to a similar mixing model. However, our study does show that the combination of FI studies including noble gas and stable isotope analyses with stable isotope analysis of ore and gangue minerals has the potential to answer this question.

Acknowledgements

3 The role of the Laramide orogeny in the formation of Climax-type molybdenite mineralization: constraints from Re-Os and Rb-Sr isotope systematics

Stoltnow M.[1,2], Romer R.L.[2], Glodny J.[2], Brauns M.[3], Kärstens J.M.[1]

[1]*Institute of Geosciences, University of Potsdam, Karl-Liebknecht-Straße 24/25, 14476 Potsdam, Germany*
[2]*GFZ German Research Centre for Geosciences, 14473 Telegrafenberg, Germany*
[3]*Curt-Engelhorn-Zentrum Archäometrie gGmbH, D6, 3, D-68159 Mannheim, Germany*

In preparation for submission to *Mineralium Deposita*. The readers must be aware of potential differences between the future publication and this chapter.

Abstract

The Sweet Home Mine hosts Pb-Zn-Ag vein mineralization similar to the peripheral vein mineralization that is spatially and temporally associated with the Oligocene Climax-type porphyry Mo deposits related to the Rio Grande Rift. Molybdenite mineralization in the Sweet Home Mine occurs in two styles (i) veins with pyrite, quartz, fluorite, and white mica and (ii) molybdenite coatings on fault gouge. Both styles occur exclusively along a major normal fault named the Contact Structure.

This study presents Re-Os molybdenite ages of 65.86±0.30 Ma from mineralization in the Contact Structure and multimineral Rb-Sr isochron ages of 26.26±0.38 Ma and 25.3±3.0 Ma from gangue minerals in Sweet Home greisen assemblages. The age data imply that mineralization formed in two separate events: Late Cretaceous (Laramide-related) and Oligocene (Rio Grande Rift-related). Thus, the age of Mo mineralization at the Sweet Home Mine clearly predates that of the Oligocene Climax-type deposits elsewhere in the Colorado Mineral Belt. The Re-Os and Rb-Sr ages also constrain the age of the latest deformation along the Contact Structure to between 62.77±0.50 Ma and 26.26±0.38 Ma, which was employed by Late Cretaceous and Oligocene fluids. Along this structure Late Cretaceous molybdenite is spatially associated with Oligocene minerals in the same vein system, a feature that precludes molybdenite recrystallization or repreciptation by Oligocene ore fluids.

3.1 Introduction

The Sweet Home Mine (SHM) hosts Pb-Zn-Ag vein mineralization that was produced for Ag on a small scale in the 19th and 20th centuries and on a larger scale for mineral specimens, particularly high-quality rhodochrosite, since the 1990s (Voynick 1998; Bartos et al. 2007). The deposit has the same mineral assemblages as occur in peripheral veins that are spatially and temporally associated with the Oligocene porphyry Mo deposits related to the Rio Grande Rift (Figs. 16a, b, 17a) (Bookstrom 1989; Misantoni et al. 1998; Seedorff and Einaudi 2004a; Audétat and Li 2017). Therefore, the vein mineralization at the SHM was interpreted to be related to a hidden Oligocene porphyry intrusion (Lüders et al. 2009). Huebnerite- and apatite-bearing mineral assemblages from the SHM yielded ages of 25.7 and 24.8 Ma, respectively (Romer and Lüders 2006), which agree with published ages for the Climax and Urad-Henderson deposits (Bookstrom et al. 1987; Markey et al. 2007). However, the paragenetic position of huebnerite in

the SHM mineralization is not entirely clear (Misantoni et al. 1998; Bartos et al. 2007) and no ages of other associated minerals at the SHM have been reported.
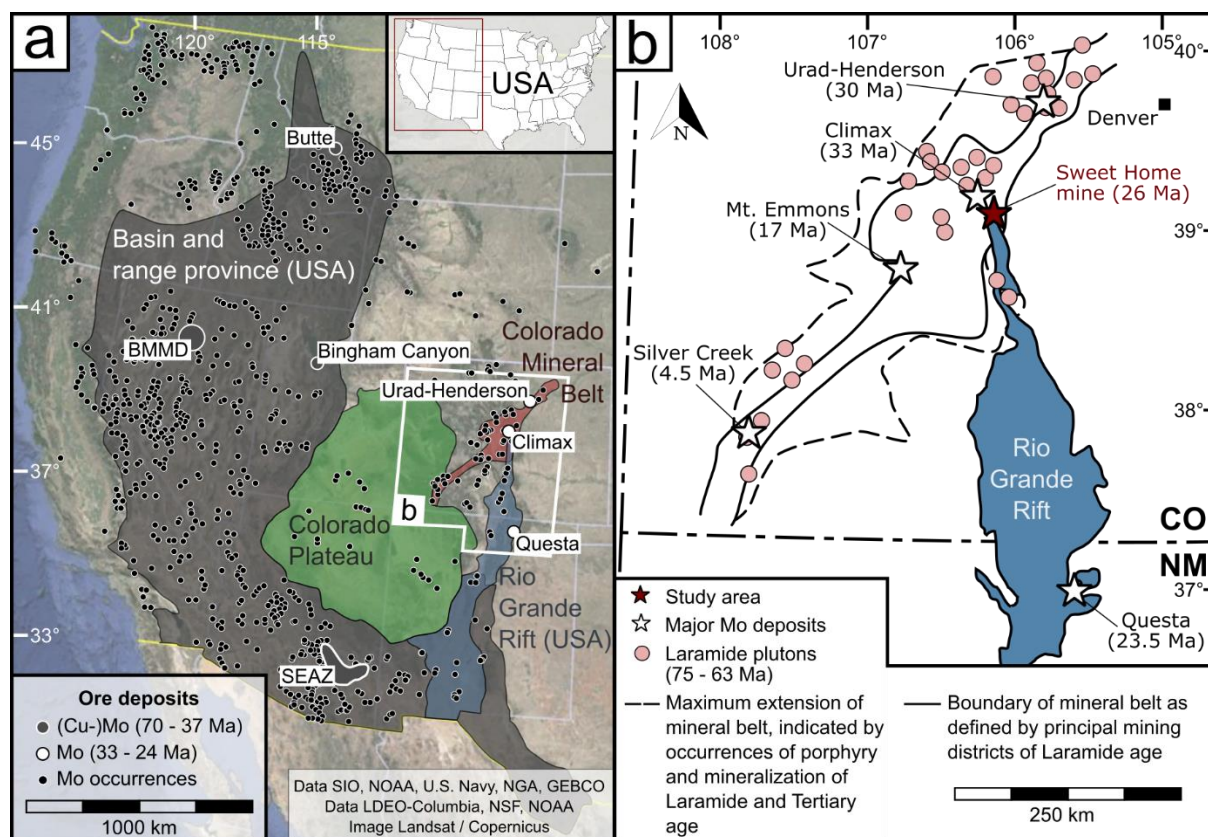
Figure 16 (a) Map of the western United States showing major geological provinces as well as major Mo deposits and occurrences: Laramide-related (gray circles), Rio Grande Rift-related (white circles), and minor Mo occurrences of all ages (black dots), from (McFaul et al. 2000). *SEAZ* = South-East Arizona district, *BMMD* = Battle Mountain Mining District. (b) Map showing the extent of the Colorado Mineral Belt (Tweto and Sims 1963) and the Rio Grande Rift with the distribution of early Laramide plutons (Chapin 2012 and references therein) and major Mo deposits with ages (Wallace 1995 and references therein; Romer and Lüders 2006).

The SHM comprises two portals, namely the Sweet Home portal (SHP), which has been operated until 2004, and the topographically higher Detroit City portal (DCP), which started operating in 2018 (Figs. 17b, c). Recent tunneling in the DCP revealed the occurrence of two styles of molybdenite mineralization along a major normal fault named the Contact Structure: (i) molybdenite-pyrite vein mineralization with quartz, fluorite, white mica, and alkali feldspar gangue (Fig. 18a); and (ii) molybdenite coating on fault gouge (Fig. 18b) which indicates syn- and/or post-mineralization movement along the fault (Stoltnow et al. 2022).

The SHM is located at the intersection of the Rio Grande Rift and the Colorado Mineral Belt (CMB) (Figs. 16a, b), which formed at the end of the Late Cretaceous Laramide orogeny (e.g., Mutschler et al. 1987). This geological setting is characterized by tectonomagmatic overprints of Late Cretaceous intrusions caused by rift-related crustal extension and bimodal magmatism (Fig. 17a) (Wallace 1995; Chapin 2012). This study applies Re-Os and Rb-Sr geochronology to determine the timing of SHM mineralization relative to these two major events; specifically, if all

SHM mineralization is contemporary with the Climax-type deposits (Rio Grande Rift- related) or whether the SHM deposit also includes an early stage of mineralization related to the development of the CMB (e.g., Laramide-related).
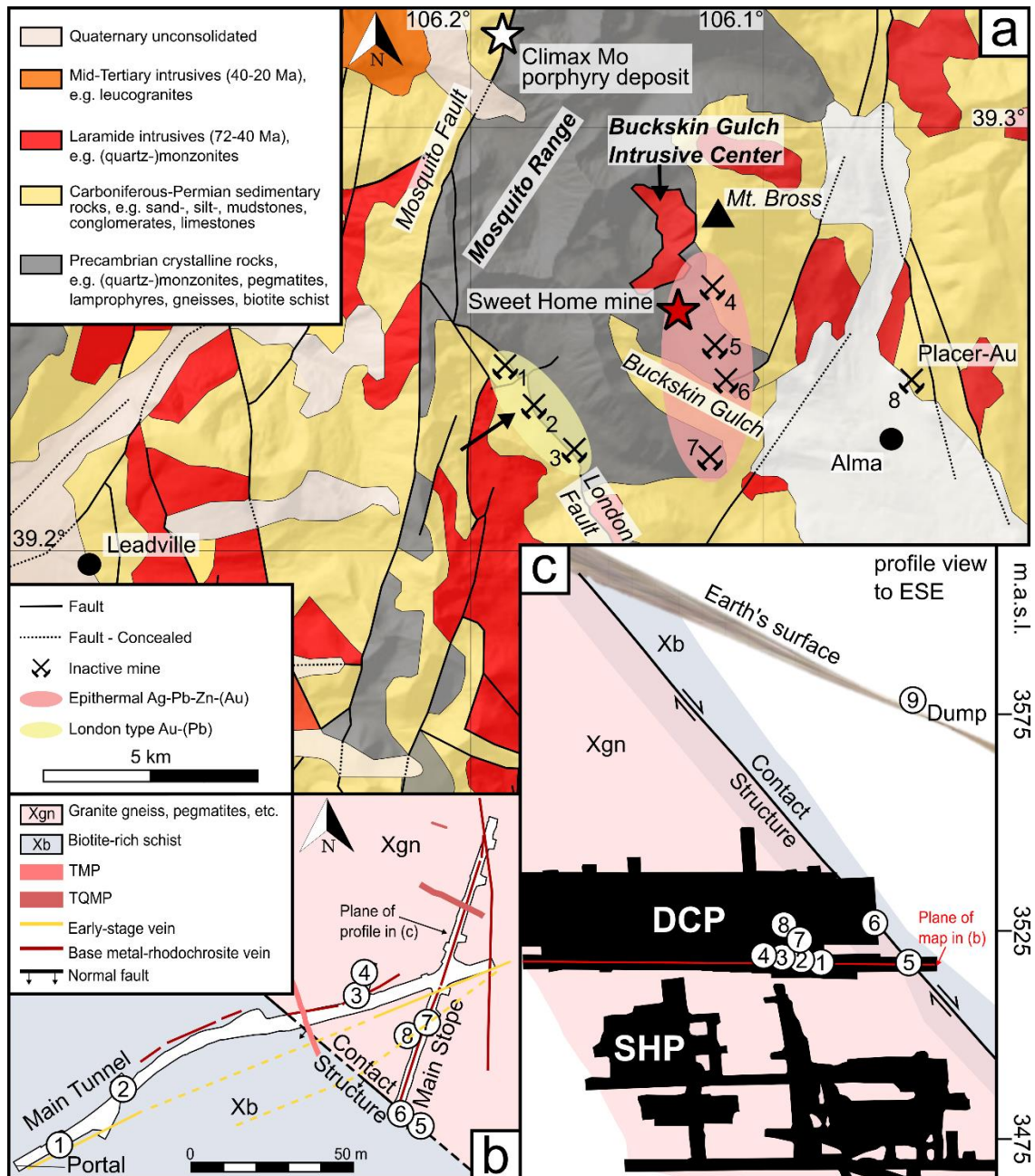
Figure 17 (a) Geological map of the Alma quadrangle (Widmann et al. 2004) showing the location of the Sweet Home Mine, the Climax Mo deposit, and other historical mining locations. *1*–North London mine, *2*–South London mine, *3*–American mine, *4*–Dolly Varden mine, *5*–Paris mine, *6*–Phillips mine, *7*–Hock Hocking mine, *8*–Richards Placer (modified from Bartos et al. 2007). (b) Simplified geological map (plan view) of the adit level (3515 m.a.s.l.) of the Detroit City Portal. (c) Profile projected onto main stope of the Sweet Home Mine with the former Sweet Home Portal workings at the bottom and the Detroit City Portal workings above. Numbers in white circles refer to sample locations, *TMP* = Tertiary Monzonite porphyry, *TQMP* = Tertiary Quartz-monzonite porphyry, *DCP* = Detroit City Portal, *SHP* = Sweet Home Portal (modified from Stoltnow et al. 2022).

3.2 Geological setting

3.2.1 Geology of the western United States

From the Neoproterozoic to late Devonian the western United States (Fig. 16a) were part of the western Laurentian passive margin, characterized by the sedimentation of thick sequences of continental clastic sediments (Stewart 1980; Cook and Corboy 2004; Dickinson 2006; Yonkee et al. 2014; Cook 2015). Starting from the Carboniferous, the western margin of Laurentia became an active margin that experienced accretion of a series of intraoceanic island arcs (Dickinson 2004). Arc accretion was accompanied by pulses of calc-alkaline intrusions in the Late Jurassic and Cretaceous related to several eastward-propagating orogenies (e.g., Burchfiel et al. 1992; DeCelles 2004; Howard et al. 2011). The last accretionary event occurred during the Laramide orogeny between 80 and 40 Ma (English and Johnston 2004).

Arc accretion was accompanied by subduction of clastic continental sediments derived from the former passive continental margin, which led to metasomatism of the sub-lithospheric mantle beneath the western United States (Lee 2005; Sun et al. 2021). The development of an active margin setting resulted in the formation of major mineral deposits. These include numerous porphyry Cu(-Mo-Au) deposits associated with Laramide magmatism, such as the Late Cretaceous South-East Arizona (SEAZ) district, the Butte porphyry Cu-Mo deposit in Montana, the Eocene Battle Mountain Mining District (BMMD) in Nevada and the Bingham Canyon porphyry Cu-Mo deposit in Utah (Fig. 16a; Appendix Fig. 7) (Gostyayeva et al. 1996; Deino and Keith 1998; Rowins 2000; Lageson et al. 2001; Sillitoe 2010; Quadt von et al. 2011). The source of the peraluminous Late Cretaceous to Eocene magmas related to these mineral deposits was suggested to be the lower crust (e.g., Farmer and Depaolo 1984) or the metasomatized lithospheric mantle (Pettke et al. 2010).

Long-lived contractional deformation in the western United States was followed by large-scale extensional tectonics in the middle to late Eocene (Dickinson 2002; Dickinson 2006; Chapin 2012). To the west of the Colorado Plateau, extensional tectonics were accompanied by the formation of the 42 and 36 Ma Carlin-type Au province in Nevada (e.g., Cline et al. 2005) and shaped the Basin-and-Range Province in the late Miocene (Fig. 16a) (e.g., McPhee 1990; Dickinson 2004). To the east of the Colorado Plateau, crustal extension of the Rio Grande Rift began about 33 My ago and was marked by the intrusion of bimodal 33-25 Ma magmas associated with the formation of Climax-type Mo porphyry deposits (Fig. 16b, Appendix Fig. 7) (e.g., Ludington and Plumlee 2009; Chapin 2012; Mercer et al. 2015).

The Colorado Mineral Belt (CMB) extends northeastward ~500 km through Colorado. This belt marks the eastern limit of magmatism related to the Laramide orogeny (Chapin 2012). Similar to the magmatic arcs to the west of the Colorado Plateau, the Late Cretaceous to Eocene history of the CMB was characterized by subduction and calc-alkaline to alkaline magmatism (Fig. 16b) (Simmons and Hedge 1978; Mutschler et al. 1987). In contrast to Laramide intrusions in the Basin-and-Range Province, which are associated with major and widespread porphyry Cu-Mo deposits (e.g., Sillitoe 2010), Laramide intrusions in the CMB do not have notable Mo mineralization (Mutschler et al. 1987). Instead, the major Mo mineralization in the CMB seems to be restricted to younger intrusions, i.e., the 33-25 Ma Climax-type porphyry Mo deposits (Urad-Henderson and Climax) that seem to be related to the opening of the Rio Grande Rift as well as post- 17 Ma mineralization (Mt. Emmons and Silver Creek) (e.g., Chapin 2012; Audétat and Li 2017).

3.2.2 Geology of the Sweet Home mine

The SHM is located ~8 km SE of the Climax Mo deposit in the Mosquito Range. The Mosquito Range is part of a NNE striking, east dipping sequence of metasedimentary rocks in the Alma mining district (Fig. 17a). The Precambrian crystalline core of the range is overlain by a lower Carboniferous sequence of siliciclastic and platform carbonate rocks as well as an upper Carboniferous-Permian sequence of arkosic sandstones and siltstones with rare, thin carbonate beds (Fig. 17a) (Myrow et al. 2003). The entire section was intruded by a series of 75 to 42 Ma old porphyritic sills, small stocks, and dikes, as well as by the 35 and 25 Ma old highly-evolved Climax-related rhyolitic intrusions (Bookstrom 1989; Bartos et al. 2007). The older group of intrusions (75 to 42 Ma) includes the monzonitic to granodioritic rocks of the Buckskin Gulch Intrusive Center (Fig. 17a) and the younger group (35 and 25 Ma) includes the so-called 'later white porphyry' and 'Climax late dikes' that are abundant in the Alma district and also occur in and near the SHM (Fig. 17b) (Bookstrom 1989; Stoltnow et al. 2022).

The SHM deposit is mainly hosted in Precambrian biotite-rich schists and granite gneisses (Fig. 17b). These units were intruded by (quartz)-monzonitic dikes (72-67 Ma) (Fig. 17b) (Bookstrom 1989) as well as by quartz-orthoclase pegmatites (Paleocene inferred; D. Misantoni, pers. commun.). The location and shape of the intrusions in the vicinity of the SHM are structurally controlled by (i) NW-SE to E-W striking and ~75° to S dipping fault and fracture zones, including the SW dipping Contact Structure, which is a contact between Precambrian biotite schist and Precambrian granite gneiss (Fig. 17b) (Stoltnow et al. 2022), (ii) NE-SW striking, ~70° to NW dipping faults, and (iii) N-S-directed, steeply (~80°) westward dipping late faults and fractures (Misantoni et al. 1998).

The SHM mineralization includes polymetallic-rhodochrosite veins and pocket mineralization and is distinguished into three mineralization stages, namely the 'early stage', the 'main sulfide stage', and the 'late stage' (Fig. 19) (Lüders et al. 2009; Stoltnow et al. 2022). The early stage is characterized by greisen-type mineral assemblages and pyrite±huebnerite±sphalerite veins with quartz, fluorite, and white mica as gangue minerals (Fig. 19) (Stoltnow et al. 2022). Early-stage veins trend NW-SE to E-W and formed from hot (>350°C), CO_2-bearing, and medium-salinity fluids (Lüders et al. 2009; Stoltnow et al. 2022). Early-stage huebnerite yielded an U-Pb age of 25.7±0.3 Ma (Romer and Lüders 2006). Along the Contact Structure, there occur thin quartz-pyrite-molybdenite±white mica veins (Fig. 18a) as well as molybdenite coatings on fault gouge with slickensides, indicating post-precipitation movement along the fault plane (Fig. 18b). Molybdenite in the quartz veins forms small acicular crystals with characteristic kink bands surrounding pyrite, quartz, and white mica crystals (Figs. 18c, d). Based on these petrographic relations molybdenite is assigned to the early stage (Stoltnow et al. 2022).

The main sulfide stage is characterized by major sulfide/sulfosalt mineralization that forms massive veins and less commonly open voids with valuable, gem-quality, cherry-red rhodochrosite specimens for which the mine is famous (Fig. 19). Both veins and pockets generally trend NE-SW and formed at temperatures between 350° and 250°C from low to medium salinity fluids with little CO_2 (Lüders et al. 2009; Stoltnow et al. 2022). Pyrite and sphalerite from the early and main sulfide stages from the DCP (Fig. 19) have the same composition as texturally equivalent sulfides from the SHP (Wenrich and Aumente-Modreski 1998), demonstrating the homogeneous character of mineralization across different mine levels (Appendix Table 6).
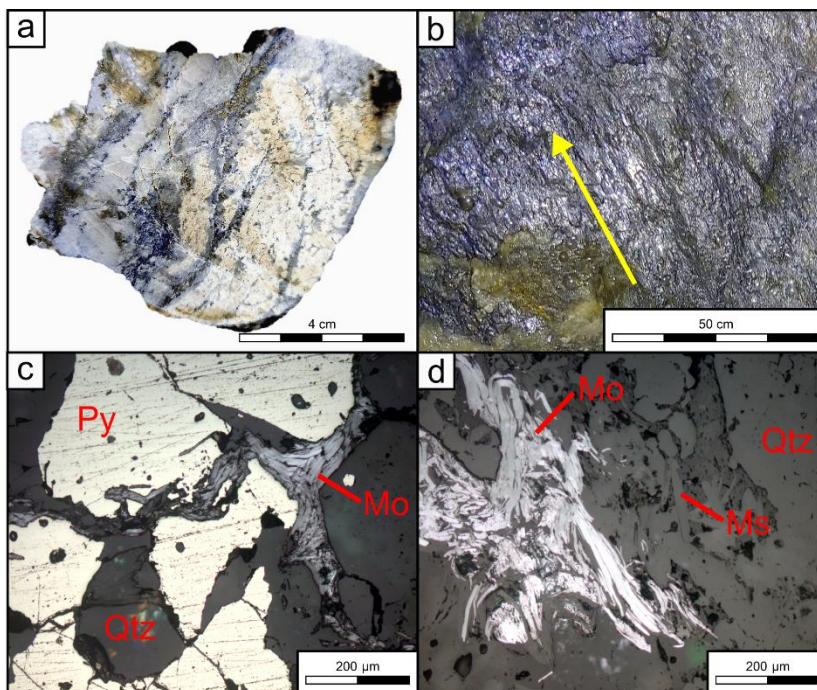
Figure 18 a) Molybdenite-pyrite vein mineralization with gangue minerals quartz, fluorite, white mica, and alkali feldspar hosted by altered granite gneiss from the Contact Structure (Sample 6), modified after Stoltnow et al. (2022). b) Underground outcrop (hanging wall) showing molybdenite coating on fault gouge with slickensides. Yellow arrow indicates movement direction on surface (photo by D. Misantoni). c) Photomicrograph showing molybdenite aggregates (Mo) surrounding pyrite and quartz (Qtz) crystals, modified after Stoltnow et al. (2022). d) Photomicrograph showing molybdenite aggregates (Mo) containing non-identifiable micro-inclusions. The aggregates surround white mica (MS) and quartz (Qtz).

Late-stage mineralization comprises assemblages of pink rhodochrosite followed by purple fluorite, and late calcite, barite, and apatite (Fig. 19). The late-stage minerals commonly form overgrowths on main sulfide-stage pocket minerals (Fig. 19) and they precipitated from a meteoric water-dominated fluid without detectable CO_2 at temperatures between 230 and 140°C (Lüders et al. 2009). Apatite of this stage yielded an U-Pb age of 24.8±0.5 Ma (Romer and Lüders 2006).

	Laramide molybdenite stage	Early stage: Greisen veins, greisen / phyllic alteration	Main sulfide stage	Late stage
Gangue minerals				
Milky quartz		▬▬		
Euhedral quartz		▬▬	▬▬	
Fluorite		*orange, green, transparent*	*purple*	*purple*
Muscovite		▬▬		
Rhodochrosite			*gemmy, murky*	*pink*
Calcite				▬▬
Apatite				▬▬
Barite				▬▬
Ore minerals				
Huebnerite		▬▬		
Pyrite		▬▬	▬▬	
Molybdenite	▬▬ This study	◄‑‑‑ ▭▭▭ Stoltnow et al. (2022)	▬▬	
Sphalerite			▬▬	
Tetrahedrite/Tennantite			▬▬	
Galena			▬▬	
Chalcopyrite			▬▬	
Bornite			▬▬	

Figure 19 Paragenetic scheme of the mineralization at the Sweet Home Mine, modified from Stoltnow et al. (2022). Modifications include the introduction of the Laramide molybdenite as the earliest mineralized stage at the Sweet Home Mine and removal of molybdenite from the early stage.

3.3 Samples and analytical methods

3.3.1 Samples

The samples studied here originate from the DCP of the SHM and are representative for the early, main sulfide, and late stages of mineralization (Fig. 19). Sample descriptions are provided in Appendix Table 7 and sample locations are presented in Figs. 17b, c and the Appendix Fig. 8.

3.3.2 Mineral separation for radiogenic isotope analysis

Mineral separation was carried out after careful textural and mineralogical characterization of the samples, with respect to mineral assemblages and mineralization stages within the veins. Small fragments with mineral assemblages belonging to a single mineralization stage were crushed in a steel mortar to particle sizes equivalent to the average grain size of individual crystals in the rocks. Minerals were concentrated using a FRANTZ magnetic separator combined with heavy liquid-based density separation. Alkali feldspar, quartz, fluorite, rhodochrosite, sphalerite, pyrite, chalcopyrite, galena, fahlore, and huebnerite were purified by hand-picking. White mica fractions were additionally ground in pure ethanol in an agate mortar to release inclusions and then sieved in ethanol to obtain inclusion-free separates. Molybdenite was enriched by heavy liquid techniques and panning. All mineral separates were finally checked and purified by hand-picking under a binocular microscope.

3.3.3 Electron microprobe analysis

The chemical compositions of sulfides and sulfosalts from 9 different thick and polished sections were determined by EPMA using a fully automated JEOL JXA-8200 instrument at the Institute of Geosciences at the University of Potsdam. The instrument is equipped with a tungsten filament and five wavelength dispersive spectrometers. The analyses were performed at an acceleration voltage of 20 kV, a probe current of 20 nA and with a focused beam (spot size of 2 μm). The elements As, Mo, Au, Fe, Ag, Ga, Sn, S, Ni, Pb, Ge, In, Ti, Cu, Sb, Zn, Mn, Te, W, and Cd were analyzed and standardized against ASTIMEX MINM 25-53 and SPI spi#02757-AB reference materials. Counting times were 20/10 s for element peaks and 10/5 s for background positions. The online ZAF matrix correction of the EPMA instrument was used. The instrument was calibrated at the beginning and during each analytical session. The accuracy of the analytical results was controlled using secondary standards. The complete EPMA dataset is presented in the Appendix Table 6. Care was taken to choose analytical points in homogeneous areas far from fractures and cavities. Sulfides and sulfosalts were analyzed using WDS.

3.3.4 Rb-Sr dating

A set of 20 mineral separates including muscovite/sericite, fluorite, K-feldspar, and sphalerite, collected from 3 samples were analyzed for Rb-Sr geochronology at GFZ German Research Centre for Geosciences (Potsdam), following the routines described in Glodny et al. (2002) and Glodny and Ring (2022). Minerals were dissolved in a 5:1 mixture of concentrated HF and HNO_3 for two days on a hot plate. The solutions were then dried, followed by conversion into chloride-form using 6N HCl at 160°C overnight on a hot plate. Sr and Rb were separated using standard cation exchange techniques (Bio Rad AG50 W-X8, 100–200 mesh, 3.8 ml resin volume) in 2.5 N HCl medium. Sr was loaded on single Ta-filaments and its isotopic composition was determined using a TRITON multi-collector thermal ionization mass spectrometer (TIMS) in dynamic multi-collection mode. Rb was loaded on single Ta-filaments and analyzed in static multi-collection mode. Concentrations were determined by isotope dilution, using a set of mixed ^{84}Sr–^{87}Rb tracers. Repeated measurements of Sr standard NIST SRM 987 during the measurement period gave 0.710255 ± 0.000024 (2σ, n=23). Total procedural blanks were consistently below 0.15 ng for both Rb and Sr. Due to generally high sample-to blank ratios and highly variable blank values, no blank correction was applied. For age calculations, uncertainties of ±0.005% for ^{87}Sr/^{86}Sr and of ±1.5% for ^{87}Rb/^{86}Sr ratios were assigned to the results if individual analytical uncertainties were smaller than these values. Otherwise, individual analytical uncertainties were used. Uncertainties of isotope and age data are quoted at 2σ. The program ISOPLOT/EX 3.71 (Ludwig 2009) was used for calculating regression lines. The ^{87}Rb decay constant as recommended by IUPAC-IUGS (Villa et al. 2015) is used in all age calculations.

3.3.5 Re-Os dating

A set of 6 molybdenite samples were handpicked under the microscope and then carefully cleaned of all mineral adhesions. The selected samples were weighed into a Carius ampoule previously spiked with ^{185}Re/common Os tracer. The Carius ampoule was cooled in a mixture of ethanol/dry ice before a mixture of 1 ml HNO_3 conc. +3 ml HCl conc. was added. The ampoules were then fused and left in an oven at 240°C for 24 hours. After the heat treatment, the samples were prepared for distillation. Distillation of the volatile Os tetroxide produced by this digestion procedure occurs at a temperature of 80°C according to Brauns (2001). In this process, OsO_4 is extracted from the digestion solution and passed through a cold trap coated on the inside with concentrated sulfuric acid. Osmium oxide condenses on the cooled H_2SO_4 and is collected in 2 ml

of 6.8 N HBr after distillation is complete. Post-purification of Os was performed by micro distillation (e.g., Birck et al. 1997). After the Os separation the digestion solution is transferred into a Teflon beaker, evaporated, picked up with HNO_3 0,8 N and Re is separated from the matrix using TEVA resin (Triskem) and HNO_3 chemistry. Os isotope ratios were determined as negative ions with ion counting on a modified Finnigan-MAT 261 (Völkening et al. 1991; Walczyk et al. 1991). Mass fractionation and correction for oxides were performed according to the method (Reisberg and Meisel 2002). The internal (2σ) precision of the $^{187}Os/^{188}Os$ was better than 0.2%. The measured $^{186}Os/^{188}Os$ as well as $^{187}Os/^{188}Os$ ratios were corrected for a blank value when necessary (0.05±0.05 pg Os, $^{187}Os/^{188}Os$ blank ~0.125), assuming an Os recovery of 85% (Brauns et al. 2000; Brauns 2001). Re measurements to determine Re concentration were performed using a Thermo ICap Q ICP-QMS, and the in-run uncertainty for $^{187}Re/^{185}Re$ is <0.2% (2σ). We calculated a blank value of 0.1 pg Re. The external reproducibility for repeated analysis of comparable amounts of Re is better 0.5%. Together with the error for the spike calibration, we estimate the overall error for the Re–Os method to be 3% (2σ, $^{187}Re/^{188}Os$) and 0.3% (2σ, $^{187}Os/^{188}Os$).

3.4 Results

3.4.1 Rb-Sr data

The Rb-Sr analytical data are listed in Table 3 and comprise analyses of gangue minerals (fluorite, alkali feldspar, white mica) and sphalerite from four greisen samples without molybdenite (Fig. 20a) as well as gangue minerals from a molybdenite-pyrite vein (Fig. 20b). Taken together, the Rb-Sr mineral data for molybdenite-free greisen samples define a regression line corresponding to an age of 26.26 ± 0.38 Ma (n = 20, MSWD = 65930). Rb-Sr mineral data from the molybdenite-pyrite vein define a regression line corresponding to an age of 25.3 ± 3.0 Ma (n = 6, MSWD = 136). The Rb and Sr concentration data reveal remarkably high Rb concentrations between roughly 1500 and 2200 ppm for all analyzed white mica fractions (Table 3), indicative of low K/Rb ratios in mica, a feature commonly observed in highly evolved, chemically fractionated granitic to pegmatitic systems (cf. London 2008). Most white mica fractions also show high $^{87}Rb/^{86}Sr$ ratios of up to >3000, as commonly seen in chemically highly evolved pegmatitic melts and fluids.

Table 3 Rb-Sr mineral data

Sample No. Analysis No.	sample	Rb ppm	Sr ppm	$^{87}Rb/^{86}Sr$	$^{87}Sr/^{86}Sr$	$^{87}Sr/^{86}Sr$ 2SE	$^{87}Sr/^{86}Sr_{26\,Ma}$
1 (greisen sample without Mol association)							
MS-1	Fluorite (green)	34.9	933	0.109	0.751460	0.0015	0.7514
MS-2	Fluorite (orange)	0.149	1059	0.00041	0.750957	0.0018	0.7510
MS-3	White mica (250-1000-nm@2A-12°)	1683	2.74	1907	1.448406	0.0028	
MS-4	White mica (125-250-mag@2A-13°)	1682	2.93	1775	1.392027	0.0023	
MS-5	White mica (250-1000-mag@2A-13°)	1683	2.47	2125	1.508615	0.0040	
3 (greisen sample without Mol association)							
MS-6	Alkali feldspar	1347	101	38.9	0.761564	0.0021	0.7473
MS-7	Fluorite (orange)	68.2	529	0.374	0.743508	0.0009	0.7434
MS-8	Fluorite (colorless)	44.9	343	0.380	0.739030	0.0012	0.7389
MS-9	Fluorite (purple)	8.73	220	0.115	0.727954	0.0012	0.7279
MS-10	White mica (125-250)	1941	4.13	1435	1.258946	0.0021	
MS-11	White mica (250-1000)	2002	2.83	2218	1.544171	0.0029	
MS-12	White mica (45-125)	1872	27.1	202	0.808164	0.0029	
2-1 (massive greisen sample without Mol association)							
MS-13	Fluorite (orange, colorless)	60.3	495	0.354	0.746917	0.0010	0.7468
MS-14	White mica (>125-mag@2A-12°)	1625	5.70	853	1.049333	0.0033	
MS-15	White mica (<125-mag@2A-12°)	1562	40.2	113	0.783044	0.0017	
2-2 (porous greisen sample without Mol association)							
MS-16	Sphalerite	5.97	0.37	46.9	0.739438	0.0080	0.7223
MS-17	White mica (125-250-mag@1,4A-13°)	2095	2.10	3232	1.941972	0.0020	
MS-18	White mica (250-1000-mag@1,4A-13°)	2218	23.1	281	0.811946	0.0020	
MS-19	White mica (250-1000-nm@1,4A-13°)	2004	3.34	1855	1.407909	0.0040	
MS-20	White mica (250-1000-mag@1,4A-nm@1A-12°)	2114	2.00	3448	2.002551	0.0040	
6 (quartz-fluorite-pyrite-molybdenite vein)							
PS3817	Alkali feldspar	781	100	22.7	0.762176	0.0024	0.7539
PS3819	Fluorite (orange, green, purple, colorless)	96.5	657	0.427	0.754467	0.0042	0.7543
PS3818	White mica (90-125 μm)	686	71.2	28.0	0.764767	0.0018	0.7546
PS3820	White mica (125-160 μm)	1495	49.4	88.2	0.785449	0.0009	0.7534
PS3821	wm 250-160 μm	1527	88.2	50.4	0.773837	0.0012	0.7555
PS3822	wm >250 μm	1324	165	23.4	0.764432	0.0016	
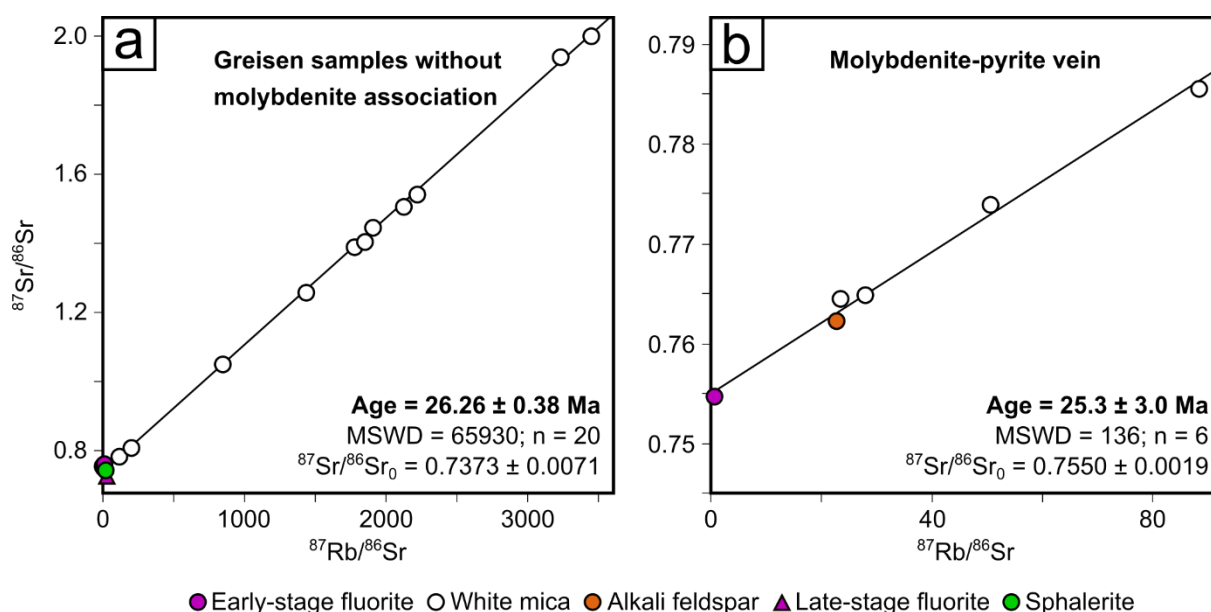
Figure 20 Rb-Sr isochrons comprising (a) gangue and ore minerals from greisen samples without molybdenite association and (b) a molybdenite-pyrite vein in a gangue of fluorite, white mica, alkali feldspar, and quartz. Note, that symbol sizes do not refer to error bar extensions.

Calculation of initial $^{87}Sr/^{86}Sr$ ratios of the low-Rb/Sr phases fluorite and sphalerite for 26 Ma gives a wide range of values between 0.7223 and 0.7514 (Table 3) as already shown from gangue minerals from the SHP (Lüders et al. 2009). This pattern points to variable Sr isotopic compositions of the fluids involved in mineral formation, with several distinct sources for Sr in the fluids and thus for other element budgets in general. This Sr-isotopic disequilibrium between different fluids and their mineral precipitates is reflected in the high MSWD values of the age-constraining regression lines. However, the variation in calculated initial Sr isotopic compositions, and thus the degree of scatter of the data around the regression lines, is very small compared to the Sr-isotopic contrasts that evolved due to radiogenic ingrowth of ^{87}Sr, particularly in white mica. Therefore, the slope of the regression lines and thus the calculated ages are well constrained despite high MSWD values (cf. Kullerud 1991), and the Rb-Sr age information is considered accurate within limits of uncertainties.

3.4.2 Re-Os data

The Re-Os analytical data are listed in Table 4. Molybdenite samples originate from the Contact Structure in the Detroit City Portal of the SHM. The Re-Os ages were determined for molybdenite coatings on fault gouge and euhedral molybdenite crystals from a vein with molybdenite and pyrite in a gangue of quartz, fluorite, and white mica (Fig. 21). Whereas

molybdenite coatings yielded Re contents between 744 and 1055 ppm combined with [187]Os contents between 508 and 706 ppb, resulting in rather variable Re-Os ages between 65.51 ± 0.52 and 62.77 ± 0.50 Ma, euhedral vein molybdenite yielded Re contents between 287 and 362 ppm and [187]Os contents between 197 and 248 ppb, which resulted in more consistent ages between 65.95 ± 0.53 and 65.71 ± 0.53 Ma (Fig. 21, Table 4).
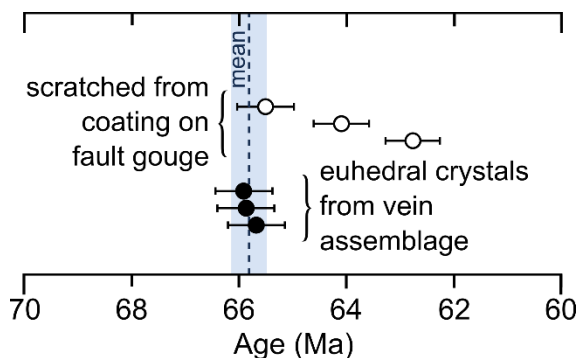
Figure 21 Re-Os ages for molybdenite coating on fault gouge (open symbols) and Re-Os ages of euhedral molybdenite crystals from the same molybdenite-pyrite vein in a gangue of fluorite, white mica, alkali feldspar, and quartz (filled symbols) along the Contact Structure in the Detroit City Portal (Sweet Home Mine, Figs. 17b, c). The mean age of vein molybdenite is 65.86 ± 0.30 Ma.

Other minerals analyzed for Re and Os in this study comprise tetrahedrite/tennantite, huebnerite, chalcopyrite, sphalerite, and pyrite. Minerals from greisen samples devoid of molybdenite have both Re and [187]Os contents below detection limit. However, pyrite from the vein assemblage has Re contents of 0.38 to 0.71 ppm and [187]Os contents of 0.27 to 0.49 ppb, which are about four orders of magnitude lower than Re and [187]Os contents of the molybdenite from the same sample (Table 4). Thus, even minute inclusions of molybdenite would, if present, dominate the Re-Os system of pyrite. The apparent Re-Os ages of pyrite between 67.15 ± 0.54 and 66.28 ± 0.53 Ma (Table 4) broadly agree with the Re-Os ages of molybdenite, which possibly implies that the apparent pyrite ages are in fact the age of molybdenite inclusions.

3 The role of the Laramide orogeny in the formation of Climax-type molybdenite mineralization

Table 4 Re-Os mineral data

Sample No. Analysis No.	Sample	Total Re (ppm)	187Os (pg)	187Re (ng)	187Os (ppb)	2s	2s	Re-Os age	2s
Sample 5 (molybdenite coating on altered granite gneiss)									
MA-205198	Molybdenite (scratched from coating)	974	1230	1.88	638	13	97	62.77	0.50
MA-205198	Molybdenite (scratched from coating)	1055	2013	3.01	706	14	105	64.10	0.51
MA-205198	Molybdenite (scratched from coating)	744	580	0.85	508	10	74	65.51	0.52
Sample 6 (quartz-fluorite-pyrite-molybdenite vein)									
MA-205199	Molybdenite (euhedral crystals)	333	354	0.51	229	5	33	65.95	0.53
MA-205199	Molybdenite (euhedral crystals)	287	432	0.63	197	4	29	65.91	0.53
MA-205199	Molybdenite (euhedral crystals)	362	363	0.53	248	5	36	65.71	0.53
Py-1	Pyrite (euhedral crystals)	0.38	27.2	0.04	0.27	0.01	0.04	67.15	0.54
Py-2	Pyrite (euhedral crystals)	0.71	44.9	0.06	0.49	0.01	0.07	66.34	0.53
Py-3	Pyrite (euhedral crystals)	0.55	36.0	0.05	0.38	0.01	0.06	66.28	0.53

3.5 Discussion

3.5.1 Two events forming the mineralization at the Sweet Home mine

The multi-mineral Rb-Sr isochron ages of gangue minerals and sphalerite from the early stage greisen assemblage at the SHM are 26.26±0.38 Ma and 25.3±3.0 Ma (Fig. 20). This age information is based on abundant sampling, internally overdetermined isochrons, with remarkably large internal Sr-isotopic contrasts due to in-situ radiogenic ingrowth of ^{87}Sr, and it is consistent between contrasting sample lithologies. This age information can thus be considered robust. Furthermore, the ages obtained agree with published ages for huebnerite- and apatite-bearing mineral assemblages from the SHM (Romer and Lüders 2006), which suggests a short interval of the formation of Oligocene mineralization at the SHM. Furthermore, they coincide with the waning stages of the Mo mineralization at the Climax and Urad-Henderson deposits, which has been related to Rio Grande Rift-related crustal extension and associated bimodal magmatism (Bookstrom et al. 1987; Wallace 1995; Markey et al. 2007; Ludington and Plumlee 2009; Chapin 2012; Mercer et al. 2015).

The initial strontium isotope ratios (calculated for 26 Ma; Table 3) of 0.7223 to 0.7514 are considerably more radiogenic than those of Climax-type-related granites/porphyries (0.7049-0.7115) in the CMB (White et al. 1981; Stein and Hannah 1985). Lüders et al. (2009) presented $^{87}Sr/^{86}Sr_{26Ma}$ values for gangue minerals from the SHP similar to those of this study, and they attributed this radiogenic strontium isotopic signature to a mixture of strontium from Climax-like porphyry stocks and the local Precambrian basement rocks (Peterman and Hedge 1968).

Molybdenite from a molybdenite-pyrite vein at the SHM yielded consistent Re−Os ages between 65.95 ± 0.53 and 65.71 ± 0.53 Ma (Fig. 21, Table 4), which are ~40 Ma older than spatially-related Oligocene mineralization (Romer and Lüders 2006; this study). The consistency of the Re−Os molybdenite ages from the molybdenite-pyrite vein underscores their reliability, as open system behavior or alteration would likely result in a range of internally inconsistent ages (Luck and Allègre 1982; Suzuki et al. 1993). In fact, the slightly wider range of Re−Os ages between 65.51 ± 0.52 and 62.77 ± 0.50 Ma of molybdenite coatings on fault gouge (Fig. 21, Table 4) may reflect variable disturbance. The oldest age from the fault gouge is identical with the Re-Os age of molybdenite-pyrite veins and may represent the mineralization age, whereas the slightly younger ages may reflect partial resetting. These slightly younger apparent ages do not necessarily date a particular event, but may be somewhere between the age of molybdenite formation and the age

of deformation, in which case the youngest Re−Os age represents the maximum age of the last deformation event. Oligocene gangue minerals do not show any signs of deformation, thus the fault gouge formed before the precipitation of the early (greisen) stage mineralization at the SHM (Fig. 19).

The Rb−Sr and Re−Os ages differ by ∼40 Ma, implying that the mineralization at the SHM formed by two separate, unrelated processes. During the older process, there was minor Mo mineralization restricted to the Contact Structure (Figs. 17b, c). The younger process formed early greisen mineralization, followed by main stage sulfide mineralization and late rhodochrosite, apatite, and fluorite, Zn, Pb, and Ag mineralization, located mainly to the north of the Contact Structure (Figs. 17b, 19). Sample 6 from the Contact Structure (Figs. 17b, 18a) is unusual as it contains minerals that were dated by both Rb−Sr and Re−Os methods and these minerals produced contrasting ages. The Contact Structure is a normal fault, which was likely (re−)activated during the Late Cretaceous (molybdenite Re−Os ages between 65.51 ± 0.52 and 62.77 ± 0.50 Ma), thereby promoting the ascent of Mo-bearing fluids, and also created the space for minor molybdenite precipitation. During the Oligocene, greisen vein mineralization (Rb−Sr isochron ages of 26.26±0.38 Ma and 25.3±3.0 Ma) cut across the Mo-hosting Contact Structure (Fig. 17b). Several studies have found that (gangue) minerals that are spatially associated with Re-Os-dated molybdenite may yield distinctly younger isotopic ages than the latter when dated by different techniques (e.g., Rb−Sr, K−Ar, ^{40}Ar−^{39}Ar) (Ishihara et al. 1989; Santosh et al. 1994; Suzuki et al. 1996; Durisova et al. 1997; Stein et al. 1997). Stein et al. (2001) proposed that this discrepancy is due to the high closure temperature of the Re−Os system, making it comparatively resistant to resetting by high-grade metamorphism and deformation (e.g., Suzuki and Masuda 1993; Suzuki et al. 1996). The Rb-Sr and K-Ar systems have lower closure temperatures as well as a greater susceptibility to chemical alteration (e.g., potassic alteration) (Watanabe and Stein 2000).

The majority of pyrite at the SHM belongs paragenetically to the Oligocene mineralization (Fig. 19) (Stoltnow et al. 2022), but dated pyrite yielded a Late Cretaceous Re-Os age, possibly due to minor protogenetic inclusions of molybdenite. These are reflected by a higher concentration of Re (0.38−0.71 ppm) and ^{187}Os (0.27−0.49 ppb) in pyrite associated with molybdenite (Sample 6, Table 4) compared to concentrations below detection limit in pyrite without this association (Samples DC−10, DC−13, Table 4, Appendix Fig. 8). Alternatively, the molybdenite inclusions may also be syngenetic, implying that there was Late Cretaceous pyrite present in addition to the Oligocene pyrite. The petrographic data in this study (Figs. 18c, d) cannot fully clarify the age of pyrite that is spatially associated with molybdenite.

3.5.2 Late Cretaceous Mo in the Colorado Mineral Belt

Re-Os molybdenite ages from the SHM coincide with the emplacement ages of numerous calc-alkaline to alkaline intrusions in the CMB that are related to the Late Cretaceous Laramide orogeny (Mutschler et al. 1987). While this arc-related magmatism has been associated with major (Cu-) Mo mineralization in the Basin-and-Range Province (e.g., Sillitoe 2010), the CMB lacks significant Mo mineralization of this age. It is likely that the absence of major Late Cretaceous Mo mineralization in the CMB is related to its position on the continent east of the former subduction zone, as well as to the thickness and composition of the underlying crust, which affected the composition of the associated magma. However, our data do not contribute further to this argumentation.

"Sweet Home-like" Mo mineralization of Late Cretaceous (and older) age in the CMB (Wallace 1995 and references therein) lacks a connection to highly evolved, F-rich A-type magmatism, which is a typical feature of Oligocene Climax-type porphyry Mo deposits in the CMB (e.g., Ludington and Plumlee 2009) and major porphyry Mo deposits elsewhere (Chen et al. 2021b). Furthermore, Rio Grande Rift-related Oligocene magmatism is bimodal, with coeval formation of mainly crust-derived (rhyolitic) and mantle-derived (lamprophyric) intrusions (e.g., Keith et al. 1993; Audétat 2010; Mercer et al. 2015). The occurrence of lamprophyric intrusions is part of an ongoing debate on whether Mo is derived from the lower crust (e.g., Farmer and Depaolo 1984; Stein 1988) or from the lithospheric mantle (Pettke et al. 2010). Stoltnow et al. (2022) provide noble gas isotope evidence that the ore fluids, which formed the Oligocene mineralization in the SHM, contained a significant mantle input. Greaney et al. (2018) noted that the lithospheric mantle should be depleted in incompatible Mo due to its refractory nature. However, the composition of the mantle may change and Mo may accumulate if fluids from the subducting slab cause mantle metasomatism. This "refertilized" mantle can then be partially melted during a subsequent rifting event (Pettke et al. 2010). Alternatively, Mo may be derived from the lower crust by partial melting of Mo-rich cumulates (e.g., Fe-Ti oxides) during rift-related magmatism (e.g., Fitton 1995; Audétat 2010; Greaney et al. 2018). Assuming a common source for both Mo and S in molybdenite, the δ^{34}S values of ~0 measured in molybdenite from the DCP would fit both a mantle and lower crustal Mo source (Stoltnow et al. 2022). On the other hand, if one allows separate sources for S and Mo, the sulfur isotope constraints may indicate a mantle or lower crustal S source, but Mo in local Late Cretaceous (and older) molybdenite mineralization in the CMB could also be derived by magma assimilation of black shales, which formed under euxinic conditions especially at the end of the Proterozoic (e.g., Holland 2005; Scott et al. 2008).

3.6 Conclusions

The combination of Re-Os and Rb-Sr isotope dating of fracture-controlled mineralization at the SHM distinguishes two separate events that exploited the same fluid pathways: Late Cretaceous (Laramide-related) and Oligocene (Rio Grande Rift-related). The molybdenite Re-Os (65.86 ± 0.30 Ma) and multi-mineral Rb-Sr (26.26 ± 0.38 Ma) ages reveal that these two events were involved in the formation of mineralization at the SHM and they also constrain the age of the latest deformation along the Contact Structure. Furthermore, Late Cretaceous molybdenite was found to coexist with Oligocene gangue minerals and sphalerite in the same vein system, which argues against molybdenite recrystallization or reprecipitation by Oligocene ore fluids.

Acknowledgements

4 Hydrological controls on base metal precipitation and zoning at the porphyry-epithermal transition constrained by numerical modeling

Stoltnow M.[1,2], Weis P.[2], Korges M. .[1]

[1]Institute of Geosciences, University of Potsdam, Karl-Liebknecht-Straße 24/25, 14476 Potsdam, Germany

[2]GFZ German Research Centre for Geosciences, 14473 Telegrafenberg, Germany

Abstract

Ore precipitation in porphyry copper systems is generally characterized by metal zoning (Cu-Mo to Zn-Pb-Ag), which is suggested to be variably related to solubility decreases during fluid cooling, fluid-rock interactions, partitioning during fluid phase separation and mixing with external fluids. Here, we present new advances of a numerical process model by considering published constraints on the temperature- and salinity-dependent solubility of Cu, Pb and Zn in the ore fluid. We quantitatively investigate the roles of vapor-brine separation, halite saturation, initial metal contents, fluid mixing and remobilization as first-order controls of the physical hydrology on ore formation. The results show that the magmatic vapor and brine phases ascend with different residence times but as miscible fluid mixtures, with salinity increases generating metal-undersaturated bulk fluids. The release rates of magmatic fluids affect the location of the thermohaline fronts, leading to contrasting mechanisms for ore precipitation: higher rates result in halite saturation without significant metal zoning, lower rates produce zoned ore shells due to mixing with meteoric water. Varying metal contents can affect the order of the final metal precipitation sequence. Redissolution of precipitated metals results in zoned ore shell patterns in more peripheral locations and also decouples halite saturation from ore precipitation.

4.1 Introduction

Porphyry copper systems are our main resources for the global supply of Cu and in addition contain a large variety of other metals at economic or sub-economic grades (Sillitoe 2010). Ore precipitation in porphyry-centered magmatic-hydrothermal systems generally produces base metal zoning patterns that transition upwards and outwards from proximal Cu-Mo to distal Zn-Pb-Ag, with variable lateral extents of up to 8 kilometers (Sillitoe 2010; Catchpole et al. 2015). Experimental studies and thermodynamic modeling indicate that cooling of magmatic fluids accompanied by fluid-rock interaction is a first-order control on metal precipitation and zonation patterns, resulting from different solubilities of the respective metals along fluid pathways (Hedenquist et al. 1998; Rusk et al. 2008). The timing and role of incursion of external fluids for ore formation are debated, with some studies indicating that fluid mixing may already occur during primary mineralization and/or that later circulation can cause metal redistribution (Sheppard et al. 1971; Proffett 2003; Fekete et al. 2016; Li et al. 2019).

Metals such as Cu, Pb and Zn in porphyry systems are predominantly transported by hydrothermal fluids as chloride complexes under elevated temperatures and rather acidic

conditions (Seward and Barnes 1997; Wood and Samson 1998). Fluid inclusion data suggest that fluids exsolving from granitic to granodioritic intrusions in the upper crust yield bulk salinities of 5 to 15 wt% NaCl$_{equiv}$ (Audétat 2019). Depending on the fluid salinity, temperature, pressure and the metal content of the parental magma, metal contents of the primary single-phase magmatic fluid vary between 20 and 20,000 ppm Cu (mean 2660 ppm), 10 and 4500 ppm Pb (mean 330 ppm), as well as 20 and 6500 ppm Zn (600 ppm) (Kouzmanov and Pokrovski 2012).

This primary fluid exsolved from the magma phase-separates upon ascent due to decompression into a low-salinity vapor and a hypersaline liquid (brine) phase. Fluid inclusion analyses and experimental studies show that base metals like Cu, Pb and Zn preferentially partition into the brine phase (Simon et al. 2006), with apparent Cu partitioning into the vapor phase now being explained as an artifact due to post-entrapment diffusion into vapor inclusions (Lerchbaumer and Audétat 2012; Seo and Heinrich 2013). However, the respective roles of the vapor and brine phases for mineralization in porphyry Cu systems remain debated, because mass balance considerations suggest that phase separation at depth produces larger amounts of vapor than brine (Henley and McNabb 1978; Landtwing et al. 2010) and some of the ascending vapor phase can condense into a liquid phase during ascent and cooling (Fournier 1999; Monecke et al. 2018; Schirra et al. 2022). Geophysical evidence and numerical modeling further suggest that brine lenses form beneath active and dormant volcanoes (Magee et al. 2018), which inspired propositions that these metal-rich hypersaline fluids with Cu contents of up to 7000 ppm stored at depth may have an economic potential (Blundy et al. 2021). However, it remains unknown whether such brine accumulations are long-lived or rather transient features, with both scenarios being permissive in different set-ups in numerical simulations (Weis et al. 2012; Blundy et al. 2021).

Furthermore, a large number of ore-stage brine inclusions homogenize by halite disappearance, which either reflects saturation in solid halite (Lecumberri-Sanchez et al. 2015) or post-entrapment modifications (Audétat 2022). Halite saturation also occurs in numerical simulations of porphyry systems using different models and set-ups (Weis 2015; Afanasyev et al. 2018). The transition from liquid-vapor stability toward vapor-halite stability of the ascending fluid would be accompanied by an abrupt decrease and eventually disappearance of the liquid mass fraction. This process would lead to an abrupt decrease in the capacity of the fluid to carry metals in solution, which could lead to base metal precipitation (Lecumberri-Sanchez et al. 2015), albeit further transportation as dispersed particles during potential eruptive processes at these conditions may also be possible.

Quantifying the dynamic behavior of mass and heat transfer in porphyry systems can be approached by numerical simulations using models that can handle high-temperature multi-phase flow of H$_2$O-NaCl fluids in porous media (Ingebritsen et al. 2010). These numerical models can simulate the evolution of the mineralization and have provided insightful results for specific

ore-forming processes (Weis 2015; Korges et al. 2020), but still rely on some simplifications. In particular, capabilities for full reactive-transport modeling including chemical speciation, pH and redox conditions as well as the role of ligand complexing for metal transport in the formation of high-temperature ore deposits are still under development. Previous work using the software CSMP++ focused on the physical hydrology and implemented a simple proxy for temperature-dependent Cu enrichment (Weis et al. 2012; Weis 2015; Korges et al. 2020). These numerical simulations suggest that the dimensions of the resulting ore shell depend on the interplay between magmatic fluid release, meteoric water convection and dynamic permeability distributions, reproducing typical copper ore bodies with bell-like shapes and lateral extents of 1-3 km (Weis et al. 2012). Recent simulations of clastic-dominant (CD-type) Pb-Zn deposits using the same model further considered the remobilization of Pb and Zn by circulating heated fluids, but based their parameterizations only on the temperature dependence of metal solubility (Rodríguez et al. 2021). These models do not yet consider the effect of fluid salinity and metal partitioning between fluid phases.

For this study, we therefore developed a new parametrization, which considers individual temperature- and salinity-dependent solubilities for Cu, Pb and Zn. The used metal solubilities are based on calculations of Kouzmanov and Pokrovski (2012), similar but not identical to parameterizations in the simulations of Blundy et al. (2021), which also introduced temperature- and salinity-dependent Cu solubilities and partitioning during phase separation to their model. The addition of Pb and Zn provides a further constraint for the hydrology at the porphyry-epithermal transition and an opportunity to test whether metal zoning with variable lateral extents can be explained by simple cooling along characteristic fluid pathways. Furthermore, we use the remobilization functionality introduced by Rodríguez et al. (2021) to constrain its impact on base metal ore shells related to porphyry systems. To date, a full representation of fluid-rock interactions at these conditions is not yet possible, because it would require an internally consistent thermodynamic model that can reliably cover high-temperature, low-density fluid phases. However, the new developments mark a step forward towards more geological realism by including additional geochemical constraints. We use this augmented numerical model to investigate the role of phase separation, brine formation, halite saturation, fluid mixing and remobilization as first-order controls of the physical hydrology on precipitation mechanisms of base metals in porphyry systems.

4.2 Methods

4.2.1 Governing Equations

We calculate fluid flow with a continuum approach for porous media using the Control Volume Finite Element Method (CVFEM) numerical scheme which is implemented in the Complex Systems Modeling Platform (CSMP++) (Weis et al. 2014). Using a realistic expression of the nonlinear fluid properties (e.g., density, viscosity and enthalpy) and the physical separation of fully miscible multi-phase fluids (liquid, vapor and halite in the H_2O-NaCl system), the model can perform compressible fluid flow at temperatures up to 1000°C and pressures up to 500 MPa (Driesner 2007; Driesner and Heinrich 2007).

Given the Darcy velocity v of a fluid phase i (liquid (l) or vapor (v)), using the extended form of Darcy's law, the circulation of these fluids is calculated as

$$v_i = -k \frac{k_{r,i}}{\mu_i} (\nabla p - \rho_i g), \qquad i = l, v \tag{1}$$

where k is the bulk rock permeability and $k_{r,i}$ the relative permeability, μ_i the dynamic viscosity and ρ_i the density of the indicated fluid phase i. The gravitational acceleration is given by g and the total fluid pressure by p (Ingebritsen et al. 2006). Saline fluids may further precipitate a solid halite phase h. We use a linear relative permeability model with

$$k_{rv} + k_{rl} = 1 - S_h \tag{2}$$

where S_h is the volumetric saturation of the immobile halite phase. The residual saturation of the liquid is given as $R_l = 0.3(1 - S_h)$ and the residual saturation of the vapor as $R_l = 0.0$.

The conservation of fluid mass is calculated as

$$\frac{\partial(\phi(S_l\rho_l + S_v\rho_v + S_h\rho_h))}{\partial t} = -\nabla(v_l\rho_l) - \nabla(v_v\rho_v) + Q_{H_2O+NaCl} \tag{3}$$

where ϕ is the porosity, $Q_{H_2O+NaCl}$ refers to the source term of fluid mass and t is the time. The conservation of salt mass is given by

$$\frac{\partial(\phi(S_l\rho_lX_l + S_v\rho_vX_v + S_h\rho_h))}{\partial t} = -\nabla(v_l\rho_lX_l) - \nabla(v_v\rho_vX_v) + Q_{NaCl} \tag{4}$$

with Q_{NaCl} as the source term and X_i as the mass fraction of NaCl in the indicated fluid phase. The conservation of energy is described by heat advection through the fluid and heat transfer through the rock with the thermal conductivity K and is given by

$$\frac{\partial((1 - \phi)\rho_rh_r + \phi(S_l\rho_lh_l + S_v\rho_vh_v + S_h\rho_hh_h))}{\partial t}$$
$$= \nabla(K\nabla T) - \nabla(v_l\rho_lh_l) - \nabla(v_v\rho_vh_v) + Q_e \tag{5}$$

where the rock is denoted by the subscript r and h_i is the specific enthalpy of the phase i. The heat source term is given as Q_e and the temperature as T. Assuming local thermal equilibrium between fluid and rock, the total enthalpy within a control volume of the mesh is distributed over the rock and fluid based on their thermodynamic properties.

The permeability k is modeled as a dynamic element property (Weis et al. 2012; Weis 2015) and is based on the following assumptions: (1) a depth-dependent background permeability profile, (2) a near-critically stressed brittle crust and a consequential failure criterion for fractures at near-hydrostatic fluid pressure conditions, (3) an increasingly ductile behavior through heating, leading to a reduction in permeability and differential stress, causing failure criteria at near-lithostatic fluid pressures (with the transition from brittle to ductile starting at 360°C), (4) a pressure-dependent permeability increase, which counteracts the temperature-dependent permeability decrease and (5) an incremental increase in permeability in response to hydraulic fracturing by as much as two orders of magnitude if fluid pressures exceed the local stress-state-dependent failure criterion. Further details on the numerical approach and benchmark solutions are given in Weis (2015) and Weis et al. (2014).

4.2.2 Proxies for metal transport, partitioning, Tx-dependent solubilities and precipitation

The main focus of this study is to advance the numerical model for porphyry Cu systems with respect to i) the solubility of Cu, Pb and Zn in the ore fluid in dependence on temperature and salinity, ii) the partitioning of these metals between vapor and liquid, iii) the metal transport by ore fluids, iv) varying metal concentrations of the primary magmatic fluid and resulting metal enrichment potential and v) remobilization of previously precipitated metals.

i) Metal solubilities are calculated using temperature- and salinity-dependent functions for the individual metals $C_i(T, x)$ applying a simple interpolation of the pyrite–magnetite–haematite-saturated solubility data at pH = 5 of Kouzmanov and Pokrovski (2012) for elevated temperatures and salinities with

$$\log(C_i) = a_{00,i} + a_{10,i}T + a_{01,i}x + a_{20,i}T^2 + a_{11,i}xT, \tag{6}$$

where T is the temperature in °C, x is the weight fraction $NaCl_{eq}$ in the fluid, $a_{00,Cu} = -9.215$, $a_{01,Cu} = 0.1126$, $a_{10,Cu} = 0.03875$, $a_{20,Cu} = -3.209 \cdot 10^{-5}$, $a_{11,Cu} = -1.213 \cdot 10^{-4}$, $a_{00,Pb} = -3.269$, $a_{01,Pb} = 0.1068$, $a_{10,Pb} = 0.01408$, $a_{20,Pb} = -5.685 \cdot 10^{-6}$, $a_{11,Pb} = -7.534 \cdot 10^{-5}$, $a_{00,Zn} = -2.234$, $a_{01,Zn} = 0.1245$, $a_{10,Zn} = 0.01313$, $a_{20,Zn} = -4.914 \cdot 10^{-6}$, $a_{11,Zn} = -1.367 \cdot 10^{-4}$. The resulting expressions are shown in Fig. 22b. These solubility relationships must be refined with further

experimental data for T > 400°C and salinities >40 wt% NaCl$_{equiv}$ as they are not yet constrained by the data from Kouzmanov and Pokrovski (2012). For the time being, we use extrapolations to higher temperatures and salinities with this parameterization, which leads to higher solubilities in these ranges and is generally in line with other studies on Cu contents in hydrothermal fluids (Lerchbaumer and Audétat 2012). However, metal precipitation is expected to rather occur within the data range covered in Kouzmanov and Pokrovski (2012). Metals are completely dissolved in the fluid phases if $c_t \leq c_{metal}(T, x)$ and metals are precipitated when $c_t > c_{eq}(T, x)$. The capacity to form sulfide minerals typical for porphyry systems (e.g., Cu: chalcopyrite, bornite, chalcocite; Pb: galena; Zn: sphalerite) would depend on sulfur availability and other chemical parameters such as pH and redox, which cannot be resolved here.

ii) The total metal concentrations, C_t, in vapor and liquid phases are expressed by

$$C_t = \sum_{i=g,l} \rho_i\, C_i S_i \Big/ \sum_{i=g,l} \rho_i\, S_i \tag{7}$$

Analytical and experimental data indicate that metal partitioning between liquid and vapor depends on the salinity of the respective phase. We approximate this observation by first calculating the solubility of the individual phases with their respective salinities and then calculate the solubility of the bulk fluid. If the fluid is saturated in a respective metal, we partition the concentration according to the respective phase solubilities, leading to a salinity- and mass-dependent partitioning. If the bulk fluid is undersaturated in a metal, we use the same degree of partitioning by assuming the same degree of undersaturation in both phases.
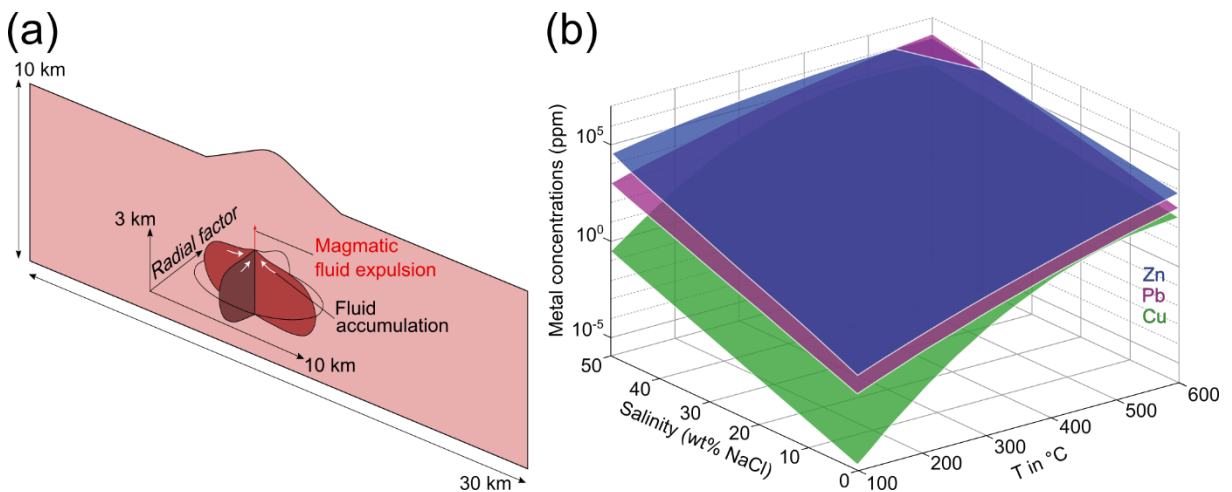
Figure 22 Model configuration and proxies for metal solubilities (a) The modeling domain represents a two-dimensional cross-section of the upper crust with dimensions of 10 x 30 km in height and width, including a magma reservoir with an extension of 3 x 10 km. The radial factor describes the extent of the magma chamber in the (unresolved) third dimension relative to the extent in the horizontal direction and thereby controls the total volume of the magma reservoir in three dimensions. Magmatic fluids are assumed to accumulate beneath a cupola region at about 5 km depth before release to the host rock. Modified from Weis (2015). (b) Modeled proxies for temperature- and salinity-dependent metal solubilities based on thermodynamic calculations by Kouzmanov and Pokrovski (2012) for zinc, lead and copper.

iii) We introduce Cu, Pb and Zn as tracers to the mass conservation as

$$\frac{\partial\big(\phi(S_l\rho_lC_l + S_v\rho_vC_v)\big)}{\partial t} = -\nabla \cdot (v_l\rho_lC_l) - \nabla \cdot (v_v\rho_vC_v) + \nabla \cdot (D_v\nabla(\rho_lC_l)) + Q_i \tag{8}$$

with the individual metal concentration in the fluid C_i, the diffusion-dispersion coefficient D, and a source term $Q_i = C_i^{initial} \cdot Q_{H_2O+NaCl}$, reflecting varying Cu, Pb and Zn concentrations $C_i^{initial}$ in the primary magmatic ore fluid. For simplicity, this formulation assumes that no metals are stored in the solid halite phase. In our simulations the amount of fluid expelled from the magma chamber depends on the size of the magma chamber, which is controlled by the radial factor (Fig. 22a). The radial factor describes the extension of the magma chamber in the unresolved z direction of a two-dimensional modeling domain. Given an extension of 10 km in x direction, a radial factor of 0.5 would correspond to an extension of 5 km in z direction (Fig. 22a).

iv) To ensure the best possible comparability with other numerical modeling studies (Weis et al. 2012; Weis 2015; Korges et al. 2020), the primary magmatic fluid contains 500 ppm Cu, which is based on measurements of intermediate density (ID) fluid inclusions in porphyry Cu systems and experimental studies. The Pb concentrations of 330 ppm as well as Zn concentrations of 600 ppm refer to mean values of ID fluid inclusions originating from numerous porphyry Cu deposits (Kouzmanov and Pokrovski 2012). To study the effect of the initial metal concentrations and metal zoning, we also performed simulations with lower initial Zn concentrations of 330 ppm (same as Pb) and Pb concentrations of 33 ppm. As a modeling proxy for ore grade distributions, we calculate metal enrichment potentials as

$$\psi_i = \frac{m_i}{C_i^{initial}C_{water}\rho_{rock}V} \tag{9}$$

with the mass of the precipitated metals m_i and the control volume V.

v) In a first suite of simulations, we consider that metals only accumulate over time due to metal precipitation from oversaturated fluids. As an additional functionality, we include remobilization of previously precipitated metals if undersaturated hydrothermal fluids flow through volumes containing metal precipitates. We assume that fluids can remobilize metals until either the fluids are saturated or the respective volume is fully depleted in the respective metal. This functionality for remobilization also covers the potential case that Cu, Pb and Zn are temporarily stored as Cl-complexes together with solid halite and also get subsequently redissolved by later ingression of less saline fluids. Further downstream, the metals can get reprecipitated as soon as the fluids become oversaturated again.

Although we account for temperature- and salinity-dependent metal solubilities, the current model cannot resolve the effect of chemical speciation (e.g. incl. pH, redox, chloride and bisulfide complexing) on metal transport, partitioning, precipitation and remobilization. Full reactive-transport has only been well established for less complex hydrothermal systems forming at lower temperatures (Yao and Demicco 1997; Yapparova et al. 2017a; Yapparova et al. 2017b),

but has the potential to be extended to higher temperatures once robust thermodynamic datasets are available. For the time being, we have to use the simplifying assumptions mentioned above and critically consider them when evaluating the modeling results.

4.2.3 Model configuration

The modeling domain is a two-dimensional cross-section of 30 km width and 10 km height and an additional topography described by a central volcano of about 1.5 km height (Fig. 22a). An elliptical magma chamber (~3 km height, 10 km width) with an initial temperature of 900°C is emplaced at 5 km depth (Fig. 22a). Previous modeling work resolving incremental magma growth shows that such magma reservoirs can be built up with magma fluxes in the order of about 10^{-2} km^3/y (Korges et al. 2020). Two radial factors (0.25 and 0.5) were applied resulting in a theoretical magma volume of ~47 km^3 and ~95 km^3, respectively. This is in line with a presumed minimal volume of 50 km^3 proposed to form porphyry Cu deposits (Sillitoe 2010; Schöpa et al. 2017). An approximately doubled magma volume is also accompanied by an approximately doubled fluid release rate, with primary magmatic fluids assumed to be expelled exclusively from the cupola region of the magma chamber (Fig. 22a). Previous modeling work resolving magma degassing mechanisms from similarly sized reservoirs describes how focused fluid release can self-organize during cooling and degassing (Lamy-Chappuis et al. 2020). With this configuration, fluid release is directly related to the cooling and crystallization of the magma reservoir due to heat conduction and convection of surrounding fluids (Weis et al. 2012). This parameterization leads to fluid release once the outer rim has reached water saturation, with highest release rates in the earlier stages and a gradual decline as the reservoir undergoes radial cooling.

Previous studies using this model for porphyry copper systems have highlighted how the dynamic permeability evolution controls the thermal evolution (Weis et al. 2012). Overall higher permeabilities lead to spatially more confined potential ore grades. Similarly, porphyry stocks that are also injected above the cupola region in natural systems but are neglected in our simplified geometry may also serve as higher-permeability pathways that could support fluid focusing. Further, the convection of surrounding meteoric fluids at depth generally flows along the margins of the magma reservoir towards the cupola region. However, the topography of a stratovolcano leads to lateral transport of mixed magmatic-meteoric fluids at shallower levels towards the base of the volcano due to the hydraulic head of the groundwater column (Weis 2015). Even though the simulations with moderate host rock permeability underneath a stratovolcano produce less confined porphyry copper ore shells, we use this configuration for the

present study, because it is best suited to understand the processes controlling metal zoning at the porphyry-epithermal transition over a lateral distance of several kilometers.

The host rock has a porosity of 0.05 and is initially saturated with pure water under a hydrostatic pressure gradient along a thermal gradient of 22.5°C km^{-1}, which is maintained by a basal heat flux of 45 mW m^{-2}. During the simulation, the upper boundary represents the Earth's surface at atmospheric pressure and is permeable. Ascending fluids can discharge across the top boundary at temperatures calculated by the model. Recharging fluids enter the modeling domain as salt-free liquid water with a temperature of 10°C. However, the fluids cannot leave the model domain via the left, right and bottom boundaries, as these are defined as no-flow boundaries. The rock properties are kept constant, including a density of 2700 kg m^{-3}, a thermal conductivity of 2 W m^{-1} C^{-1}, a diffusion-dispersion coefficient of 10^{-12} m^2 s^{-1} and a heat capacity of 880 J kg^{-1}°C^{-1}. The same values apply to the magma chamber, though beginning with a two-fold heat capacity that decreases gradually as the magma chamber cools considering the latent heat release during crystallization (Hayba and Ingebritsen 1997).

We present results from the five most representative simulations to study the influence of three key parameters:

- Magma volume and fluid release rate: magma volume of ~47 km^3 (simulation 1) or ~95 km^3 (simulation 2); initial fluid concentrations of 500 ppm Cu, 330 ppm Pb, and 330 ppm Zn; without metal remobilization;

- Metal contents: magma volume of ~47 km^3; initial fluid concentrations of 500 ppm Cu, 33 ppm Pb, and 600 ppm Zn (simulation 3); without metal remobilization;

- Remobilization: magma volume of ~95 km^3 (simulation 4) or ~47 km^3 (simulation 5); initial fluid concentrations of 500 ppm Cu, 330 ppm Pb, and 330 ppm Zn; with metal remobilization.

4.3 Results

4.3.1 Contrasting hydrological evolutions in response to magma degassing

Our simulations show that the release rate of magmatic fluids from the cupola region of a magma chamber is an important control on the outward propagation of the thermal and saline fronts as well as the location of the hydrological divide (Fig. 23). This hydrological divide (indicated by a pore fluid factor of 0.7; red dashed line) separates an inner domain dominated by ascending magmatic fluids under near-lithostatic pressures and nominally ductile rock behavior from an outer brittle domain characterized by the convection of colder fluids under near-hydrostatic pressures [23,26]. The fluid release rate is proportional to the dimensions, water content and cooling rate of the magma reservoir. In simulation 1, which assumes a reservoir volume of ~47 km^3 (radial factor = 0.25), the hydrologic divide is located at a depth level of ~2.2 km, ~2.1 km and ~3.6 km after 10, 50 and 100 kyrs, respectively (Figs. 23a, b, c). In comparison, assuming a larger total reservoir volume of ~95 km^3 (radial factor = 0.5) results in a hydrological divide that is located at comparatively shallower depths at ~1.8 km, ~1.9 km and ~3.1 km after 10, 50 and 100 kyrs, respectively (Figs. 23d, e, f).

In both simulations, the highest bulk salinities are found on the brittle domain side of the hydrologic divide at 10 and 50 kyrs, respectively (Figs. 23a, b, d, e). However, in simulation 1, both the fluid bulk salinity as well as the extent of the thermal and saline plume are lower compared to simulation 2 with higher magmatic fluid release (Fig. 23), reflecting contrasting phase separation behavior. During the entire degassing period of simulation 1, the primary magmatic fluid is injected as a single-phase fluid that phase-separates into a vapor and brine phase upon ascent, but no saturation with solid halite occurs. In contrast, simulation 2 rises to slightly shallower crustal levels at lower pressures where the liquid-vapor fluid mixture reaches halite saturation (yellow areas), therefore entering the three-phase (VLH) field of the H_2O-NaCl system (Figs. 23d, e, f). At these conditions, the liquid phase can eventually disappear completely and the fluids enter the two-phase VH-field with a volatile, low-density vapor phase and an immobile solid halite phase, resulting in the observed high bulk salinities.
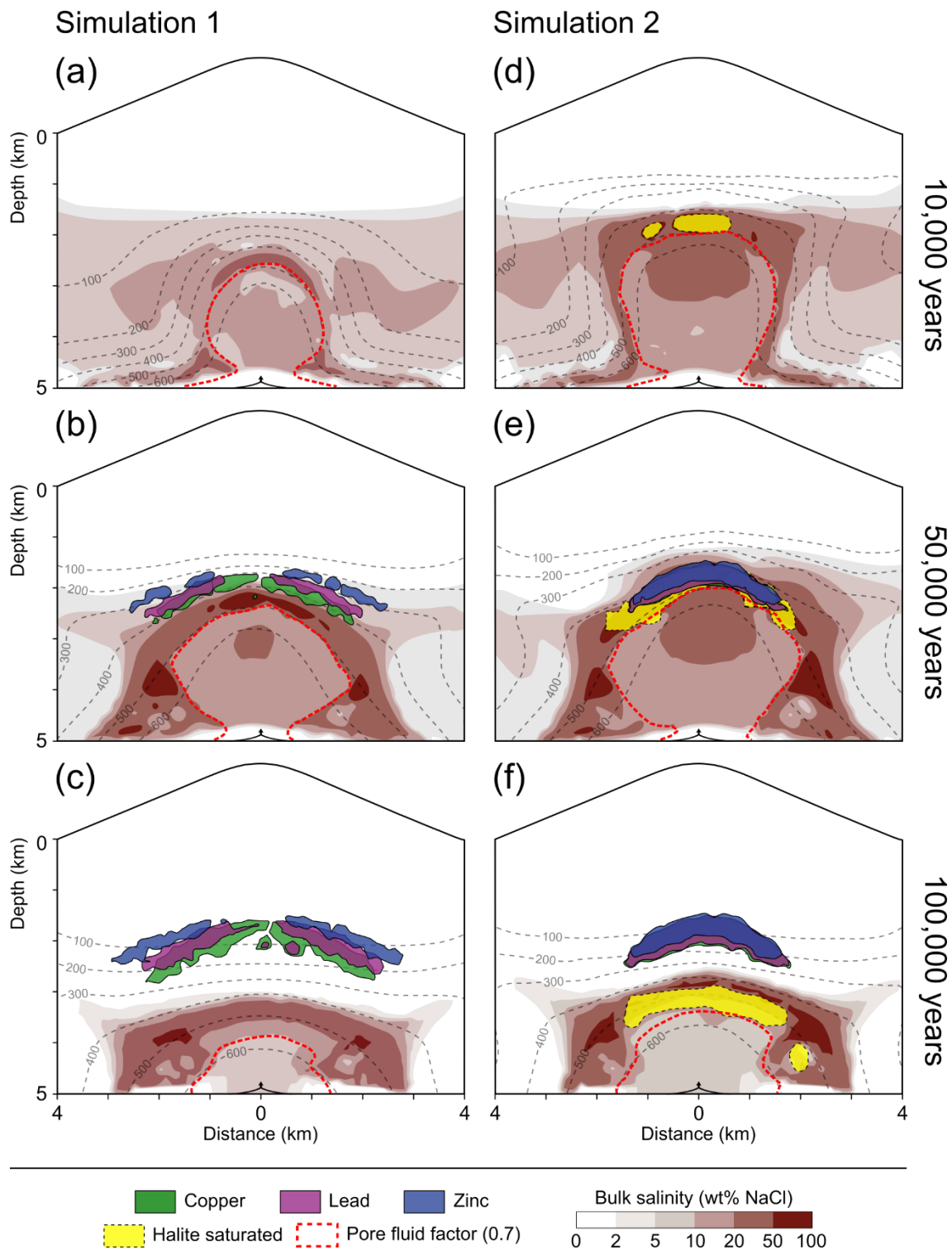
Figure 23 Temporal and spatial evolution of the hydrology of porphyry copper systems with a volcano topography after 10 (a, d), 50 (b, e) and 100 (c, f) kyrs of simulation time, showing modeled temperature distributions (isolines), the bulk salinity of the fluid mixture (red colors) and the region with halite-saturated fluids (yellow). Ore shells are represented by metal enrichment potentials (see text). The pore fluid factor (fluid pressure divided by lithostatic pressure) of 0.7 indicates the transition from near-hydrostatic to near-lithostatic fluid pressures. Simulation 1 used a radial factor of 0.25 and metal enrichment potentials of 250 for Cu, Zn and Pb (a-c). Simulation 2 used a radial factor of 0.5 and metal enrichment potentials of 500 (d-f). Arrows at a depth of 5 km refer to the fluid injection location at the cupola region of the magma reservoir.

4.3.2 Metal transport and precipitation

Ore precipitation in simulation 1 occurs atop the area of highest fluid bulk salinities under relatively low temperatures ranging from 400 to 200°C (Figs. 23b, c). The ore shells are represented by a metal enrichment potential of 250 and show an outward zonation from Cu to Pb to Zn (Fig. 23b). A metal enrichment potential of 1000 corresponds to an ore grade of about 2.5 wt%, but should only be considered as a proxy as it does not include the efficiency of Cu precipitation (Weis 2015). This zonation pattern becomes more pronounced during further magma cooling (Fig. 23c). Contrastingly, ore shells in simulation 2 develop in the restricted area of halite saturation of the ore fluid, which is characterized by higher temperatures ranging from 450 to 350°C (Fig. 23e). Ore precipitation is displayed with a metal enrichment potential of 500, taking into account that twice the amount of magmatic fluids is used in simulation 2 in comparison to simulation 1 (Figs. 23e, f). The Cu, Pb and Zn ore shells do not show a considerable zonation pattern (Figs. 23e, f). In addition to the retreat of the thermal and saline fronts caused by the cooling of the magma chamber, the area of halite saturation also recedes while the ore shells remain in place (Figs. 23c, f), showing that metal enrichment is dominated by the early phases of the hydrothermal system with the highest fluid release rates.

The impact of varying amounts of magmatic fluids expelled from the magma chamber can further be illustrated by monitoring the degree of Cu saturation (value between 0 and 1) and the Cu content (in ppm) of the fluid (Fig. 24). The magmatic volatiles are injected as single-phase fluids with Cu contents of 500 ppm and a Cu saturation of about 0.66 at the cupola of the magma chamber at a depth of ~5 km (Fig. 24). With continuing ascent in the inner part (pore fluid factor >0.7) under near-lithostatic pressures, the fluids separate into a low-salinity, low-density vapor and a high-salinity, high-density brine phase. This region is characterized by elevated bulk salinities between 30 and 50 wt% NaCl (Figs. 23b, e), low Cu saturation (Figs. 24a, c), but relatively high Cu contents (Figs. 24b, d). Even though the Cu content increases due to preferential partitioning into the brine phases, the bulk Cu saturation is reduced because metal solubilities are not linearly correlated with salinity (Fig. 22). The spatial extent of the two-phase region is smaller in simulation 1 (Figs. 23a, b) than in simulation 2 (Figs. 24b, d).

High-pressure conditions enable the further ascent of the heavy brine within the overpressured inner domain and therefore a brine-dominated zone develops atop the hydrological divide after the pressure-drop to near-hydrostatic values (Fig. 23). In simulation 2, this is the zone where halite saturation occurs, which is accompanied by a rapid increase in Cu saturation (Fig. 24c), because the saturation of the brine phase is reduced at the VLH-coexistence and can lead to the complete disappearance of the brine phase if the fluid enters the VH-field. Subsequently, Cu, Pb and Zn co-precipitate (Figs. 23e, f) and the Cu content in the ore fluid

decreases (Fig. 24d). Ore precipitation occurs within magmatic fluid fractions between 0.9 and 1, reflecting a minor contribution of relatively cool, low-salinity meteoric fluids between 0 and 10% (Fig. 24c).
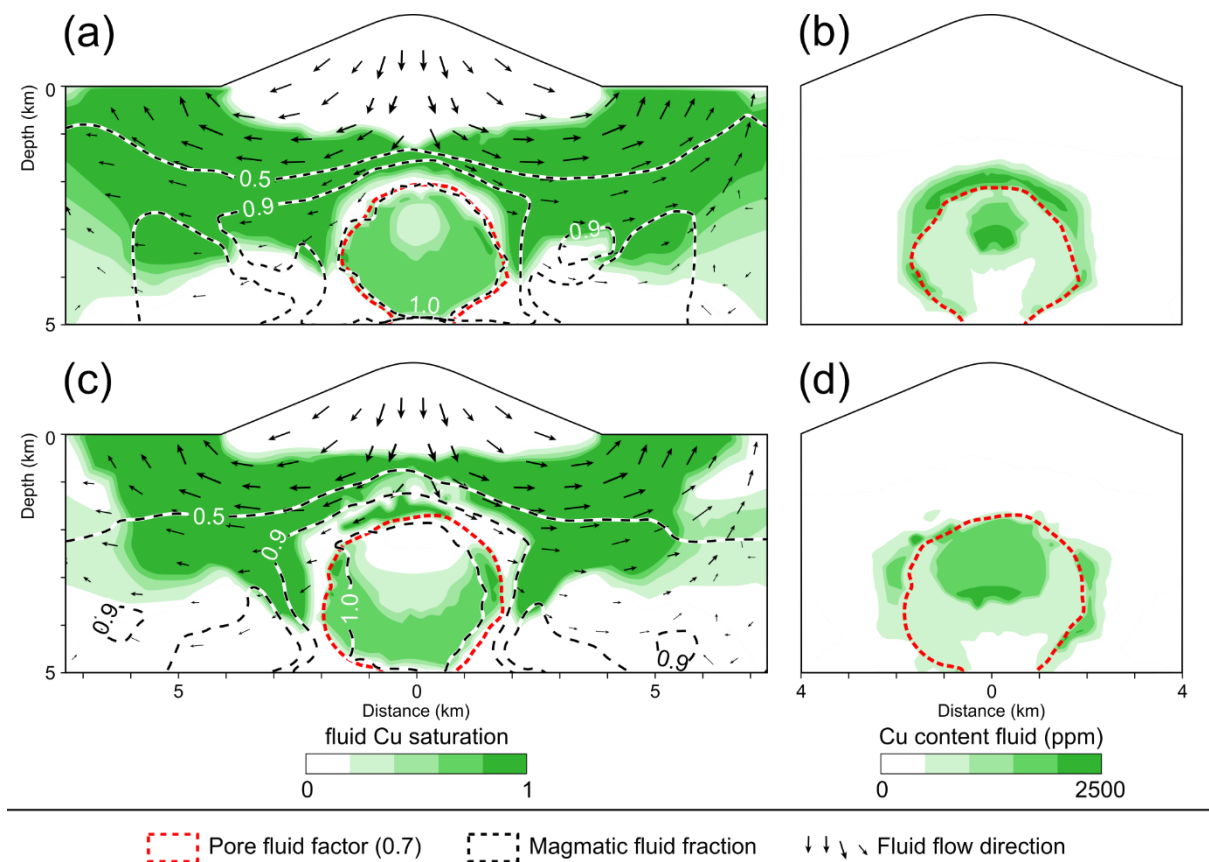
Figure 24 Copper saturation (a, c) and copper content (b, d) of the fluids within the hydrothermal system after 25 kyrs for the simulations 1 (a, b) and 2 (c, d). The pore fluid factor of 0.7 indicates the hydrological divide. The magmatic fluid fraction is represented by isolines of 1, 0.9 and 0.5, reflecting a magmatic fluid contribution of 100, 90 and 50% or a meteoric fluid contribution of 0, 10 and 50%, respectively. Black arrows schematically show fluid flow in the dominantly brittle domain.

In the absence of halite saturation, as in simulation 1, the brine zone is enriched in Cu (Fig. 24b) and ore precipitation occurs directly atop by dilution of the metal-rich magmatic brines (Fig. 23b). This zone is characterized by the convection of significant amounts of meteoric fluids (Fig. 24a). At the time of ore precipitation, the meteoric water contribution in this simulation increases significantly to 50% in the area of the Cu and Pb shells and even to more than 50% within the Zn shell (Figs.23b, c, 24a). Similar to simulation 2, ore precipitation in simulation 1 is accompanied by a decrease in the Cu content of the ore fluid, indicating that the majority of the metals have been deposited (Fig. 24a, b). Compared to the simulation with halite saturation (Fig. 23f), the potential ore shells have been moved to more peripheral locations and are spread out more laterally (Fig. 23c), which is less similar to the characteristic ore shell geometry of porphyry Cu deposits but approaches the maximum extent of base metal zoning observed in some porphyry-epithermal systems.

4.3.3 The role of initial metal contents

Simulation 1 produces a pattern of metal zoning which directly reflects the general trend of metal solubilities during cooling and dilution (Fig. 22), with Cu precipitating first, followed by Pb and Zn precipitating last. However, some deposits show a different zoning sequence, such as the polymetallic Morococha deposit in Peru with an outward directed Cu-Zn-Pb zonation (Catchpole et al. 2015). Ore precipitation is related to the timing of saturation in the respective metals, which depends on the metal contents in the input fluid. In simulation 3, we reduce the initial Pb content to 33 ppm and increase the initial Zn content to 600 ppm. Regarding the isoline of maximum Zn saturation from simulation 1, higher Zn contents only cause minor deviations towards greater depths (Fig. 25a). In contrast, the reduced Pb contents shift precipitation towards markedly shallower depths (Fig. 25b).
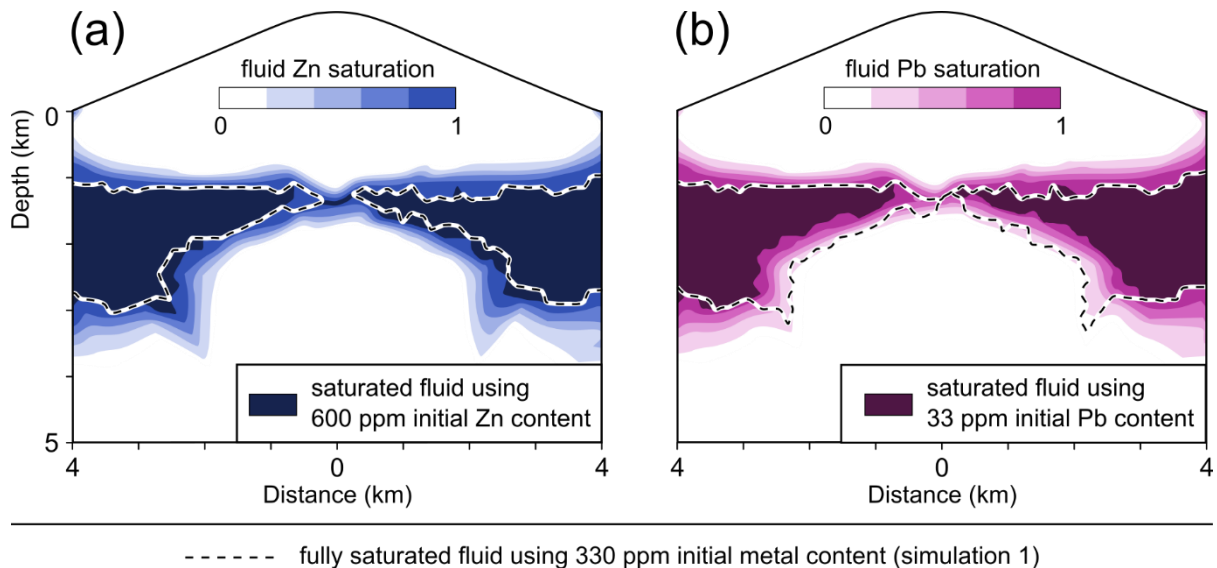
Figure 25 Variations in Zn (a) and Pb (b) saturations due to different initial metal concentrations in simulations 1 (dashed lines) and 3 (contours) after 25 kyrs of simulation time.

In Fig. 26a, comparison of the simulations 1 and 3 shows the effect of varying initial fluid metal contents on the final metal enrichment (after 100 kyrs of simulation time). We use an arbitrary threshold of 0.5 kg/m^3 of the total metal contents in the rock (sum of the Cu, Pb and Zn contents) as a proxy for a potential polymetallic ore shell.

Considering initial fluid metal contents of 500 ppm Cu, as well as 330 ppm Pb and Zn (simulation 1), the highest total rock metal contents are found at the intersection of the Cu and Pb shells and thus indicate a dominance of Cu and Pb in the overall metal content of the rock (Fig. 26a). The area of the total metal contents, which is overlain by the corresponding Zn shell, however, yields rather intermediate values (Fig. 26a). In comparison, Fig. 26b presents the highest total metal contents directly on and beneath the intersection of the Cu and Zn shells and

thus indicates the dominance of Cu and Zn in the overall rock metal content. The area of the total rock metal contents, which is overlain by the corresponding Pb shell, however, yields rather low values (Fig. 26b).

Figures 26c, d display the ratios of the individual metals in relation to the total metal content. Cu is found most proximal to the fluid source. Cu ratios are similar for both simulations due to the same initial Cu contents in the ore fluid and a similar overall initial metal content in the ore fluid (compare 1160 ppm for simulation 1 and 1130 ppm for simulation 3). Zinc yields relatively high ratios beyond the Cu-enriched zone (Figs. 26c, d), however, increasing initial fluid zinc contents to 600 ppm caused zinc enrichment to start at greater depths and to reach higher ratios of up to >0.9 (dark red; Fig. 26d). In contrast, at initial fluid contents of 330 ppm, Pb has a rather moderate ratio because of the partial overlap with the Cu and Zn shells and is located proximal to the Cu zone (Fig. 26c). Initial Pb contents of 33 ppm result in low ratios located more distal to the Cu zone (Fig. 26d).
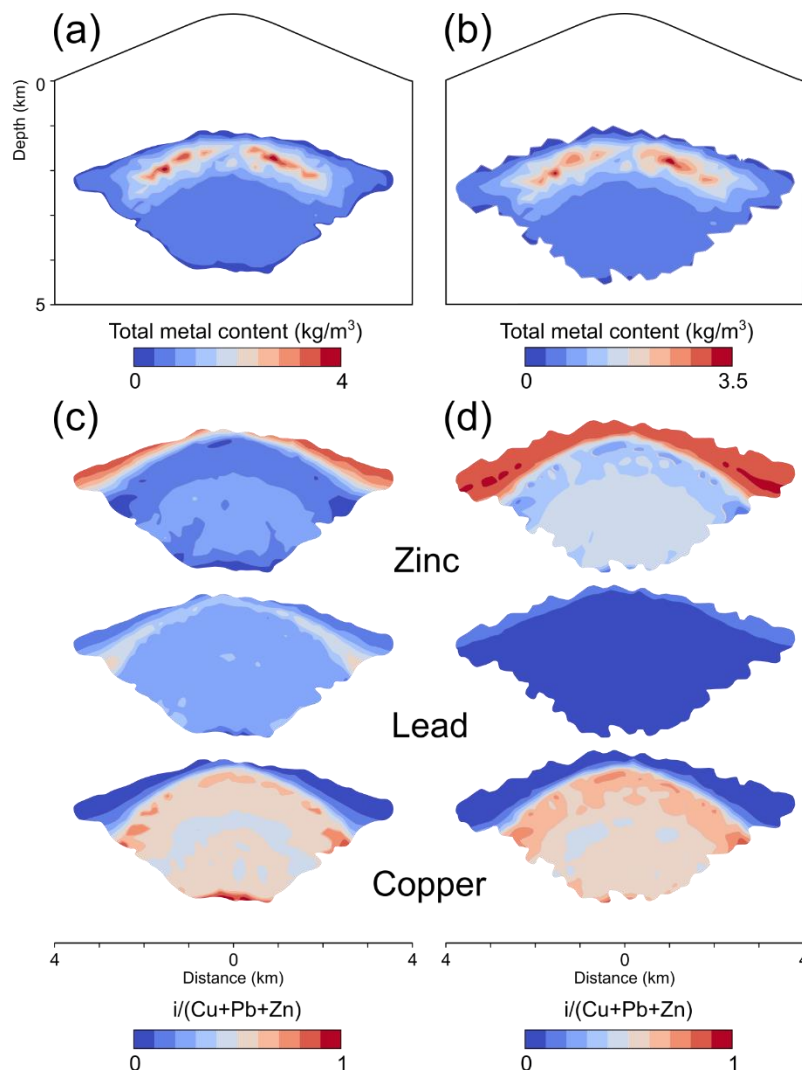
Figure 26 Total modeled metal content of the rock after 100 kyrs of simulation time above a threshold of 0.5 kg/m³ (sum of the copper, lead and zinc contents) for the simulations 1 (a) and 3 (b). Individual metal fractions within these areas of enrichment illustrate the modeled base metal zonation (c, d).

4.3.4 The role of remobilization

Remobilization of metals shifts the position of the ore shells beyond the brine zone to more peripheral areas (Fig. 27). Due to the downward flow of cooling ambient fluids from the stratovolcano to the flanks (see Fig. 24c), metal saturation is also moved to greater depths with remobilization (Fig. 27). The sequence of the metal zonation is similar to previous simulations, hence the Zn appearance forming the broadest shell, Pb the intermediate and the Cu shell the narrowest one (Figs. 27a, 27b and 27c, respectively). However, Zn and Pb develop ore shells that exclusively occupy the flanks of the upper boundary of the brine zone whereas Cu forms nearly a continuous ore shell after 25 kyrs of simulation time (Figs. 27a, 27b and 27c, respectively).
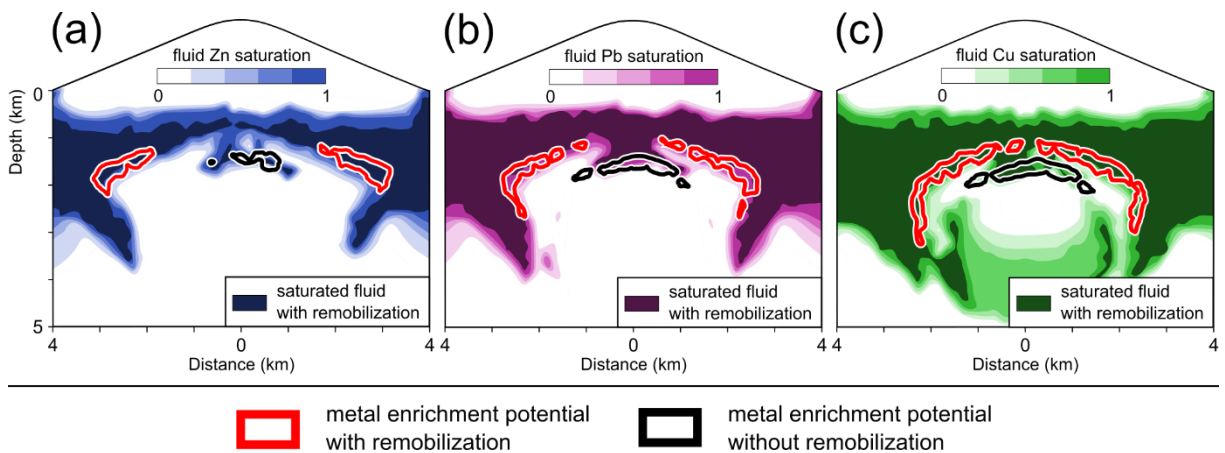
Figure 27 Location of Cu (a), Zn (b) and Pb (c) enrichment potentials of 500 after 25 kyrs of simulation time with (red isoline; simulation 4) and without (black isoline; simulation 2) metal remobilization, as well as zinc (a), lead (b) and copper (c) saturations of simulation 4 (color contours).

Figure 28 shows a comparison of the final shapes and extensions of the ore shells caused by remobilization for simulations with (simulation 4 with a larger magma reservoir) and without halite saturation (simulation 5 with a smaller magma reservoir) after 100 kyrs of simulation time. A threshold of >0.5 kg/m^3 of the total rock metal contents is displayed for simulation 4 (Fig. 28a) and 5 (Fig. 28b). Both simulations exhibit a zonation pattern from Cu to Pb to Zn. The highest total metal contents are found on and beneath the intersection of the Cu and Pb shells (Figs. 28a, b), while areas overlain by the related Zn shells yield lower values (Figs. 28a, b). The Pb and Zn ore shells are discontinuous and thickened at their outermost parts, whereas the corresponding Cu shell is continuous and rather stretched down to greater depths along the flanks (Fig. 28a). In contrast, the Zn ore shell of simulation 5 is discontinuous and peripheral precipitates are rather oriented to shallower depths, whereas the Cu and Pb shells are continuous and regularly formed (Fig. 28b).
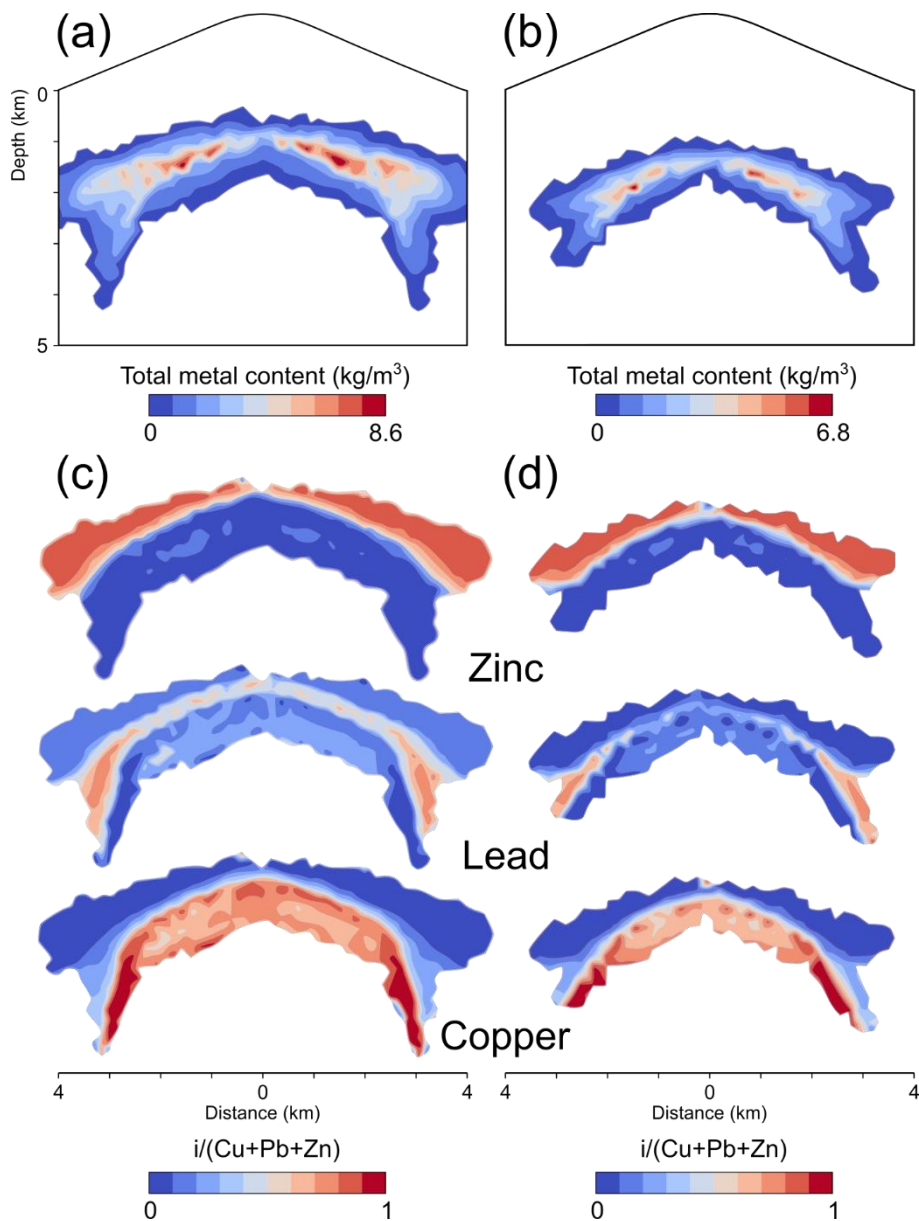
Figure 28 Total modeled metal content after 100 kyrs of simulation time above a threshold of 0.5 kg/m³ (sum of the copper, lead and zinc contents) for the simulations 4 (a) and 5 (b). Individual metal fractions within these areas of enrichment illustrate the modeled base metal zonation (c, d).

4.4 Discussion

The modeling results show that the release rate of the fluids originating from the magma chamber affects the location of the thermal and saline fronts (Fig. 23) and thereby fluid phase relations and mechanisms for metal precipitation. Higher fluid release rates from a larger magma reservoir move the hydrological divide to shallower depth levels and thus lower pressures where the two-phase fluid saturates in solid halite (Figs. 23d, e). In contrast, at lower fluid release rates

from a smaller reservoir, meteoric fluids can cool and dilute the magmatic fluids more effectively at greater depths and higher pressures which prevents halite saturation (Figs. 23a, b).

The simulations with lower fluid release rates suggest that metals are precipitated from a two-phase vapor-brine fluid and develop zoned ore shell patterns similar to typical observations in porphyry Cu systems (Sillitoe 2010; Catchpole et al. 2015) (Figs. 23b, c, 26, 28). Metal precipitation occurs directly atop the zone of highest fluid Cu contents (Fig. 24b) by admixing of relatively cool and less saline circulating meteoric water, which contributes >10% to the overall fluid budget (Fig. 24a). Our simulations indicate that meteoric water incursion is generally necessary as a cooling and diluting fluid component for the hydrothermal systems. Progressive fluid mixing along the porphyry-epithermal transition is in line with interpretations of modern stable isotope studies, but the modelled amount of meteoric water incursion required for base metal precipitation generally exceeds their estimates (Hedenquist et al. 1998). The modeled sequence of base metal precipitations (Cu-Pb-Zn) follows the parameterization of metal solubilities used for this study and is also detectable in natural ore bodies (Plotinskaya et al. 2014), especially when considering the strong overlap of the Pb-Zn mineralized zones (Nash and Theodore 1971; Mao et al. 2011; Catchpole et al. 2015). Other porphyry-related base metal deposits show a zonation from Cu to Zn to Pb, which is more common (Proffett 2003; Masterman et al. 2005; Sillitoe 2010) and could be reproduced if the initial fluid is Pb-poor.

The simulations show that the metal content and solubility of the single-phase magmatic input fluid is a limiting factor controlling ore precipitation, in particular for Cu. During ascent and phase separation of the nearly Cu-saturated primary magmatic fluid, Cu contents in the bulk two-phase fluid will be considerably increased due to preferential partitioning into the brine phase and faster ascent of the vapor phase. Our modeled concentrations are comparable to values measured in brine inclusions (Bodnar et al. 2014). However, this two-phase fluid is undersaturated in Cu, because solubility increases non-linearly with salinity according to data provided by Kouzmanov and Pokrovski (2012). Depressurization and cooling at the hydrological front can first increase the amount of vapor within the two-phase zone, leading to near-saturation Cu contents. However, once fluid pressures reach near-hydrostatic values, the high-density brine phase dominates, leading to Cu contents well above the ones of the input fluid, but again very low Cu saturations. Cu precipitation can thus only be reached by further cooling and/or brine dilution.

The simulations further illustrate that phase separation is a temporally and spatially continuous process, which makes the debate about whether the vapor or the brine phase transport and precipitate the bulk of the Cu ore difficult. Vapor and brine ascend together, albeit at different velocities, and are at all times fully miscible according to given TPX-dependent phase relations. Hence, even if Cu preferentially partitions into the brine phase and S into the vapor phase, both elements are likely to still be available in the two-phase mixture to form Cu sulfide minerals in case of oversaturation (Fournier 1999; Monecke et al. 2018; Schirra et al. 2022).

Halite saturation can cause co-precipitation of Cu, Pb and Zn (Figs. 23e, f). Given the assumption in our model setup that halite cannot incorporate any metals, metal saturation of the residual brine subsequently increases rapidly and causes the metals to precipitate. However, the lack of significant metal zoning stands in contrast with the typical distinction between Cu-bearing ore stage veins and Pb-Zn-veins in porphyry systems. This possibly limits the potential of halite saturation of a pure magmatic fluid during ore formation. The modelled halite saturation is a transient feature during the evolution of the hydrothermal system, because halite gets redissolved by later fluid incursion. Similarly, metals temporarily stored in solid sulfide or chloride phases can develop peripheral zoning patterns during later remobilization. Such metal-rich brines could still be halite-bearing during dilution and remobilization during meteoric water incursion, which would again be permissive with an interpretation of halite-saturated ore fluids. However, whether fluid inclusions homogenizing by halite disappearance are indirect evidence for halite saturation (Lecumberri-Sanchez et al. 2015) or result from post-entrapment modifications (Audétat 2022) remains debated, and our new modelling results can only confirm that it is a possible but not an inevitable ephemeral feature.

Enabling redissolution of already precipitated metals in dependence on their calculated solubility and abundance decouples halite saturation from ore precipitation and also results in the formation of a zoned ore shell pattern (simulation 4, Figs. 27, 28). Metal reprecipitation occurs beyond the brine area by further mixing with circulating meteoric water, albeit at more distal locations and at lower temperatures compared to simulations without remobilization. With the chosen simulation set-up with a stratovolcano at the surface, fluid flow in the brittle domain is directed downward and outward, which can form discontinuous ore shells (Figs. 27, 28a) with metal enrichment in peripheral areas.

The simulations presented in this study produced wider and more horizontally stretched Cu ore bodies than typically observed in high-grade porphyry Cu deposits. However, previous studies have shown that limiting the extent of more vertically extended ore shells to 1-3 km can be achieved by increasing the host rock permeability in the model parametrization (Weis et al. 2012). The dimension of the peripheral zoning with lateral extents of up to 8 km generally fits with observations of some porphyry-epithermal systems (Lang and Eastoe 1988; Sillitoe 2010), in particular when also considering low-grade metal contents (Fig. 29). However, the Pb and Zn precipitation fronts do not migrate into near-surface epithermal areas even with the consideration of remobilization (Figs. 29a, c, d), therefore displaying typical sub-epithermal veins (Sillitoe 2010). Distinct epithermal mineralization events may thus require a distinct fluid event or pulse that could lead to higher fluid temperatures in the epithermal regime.
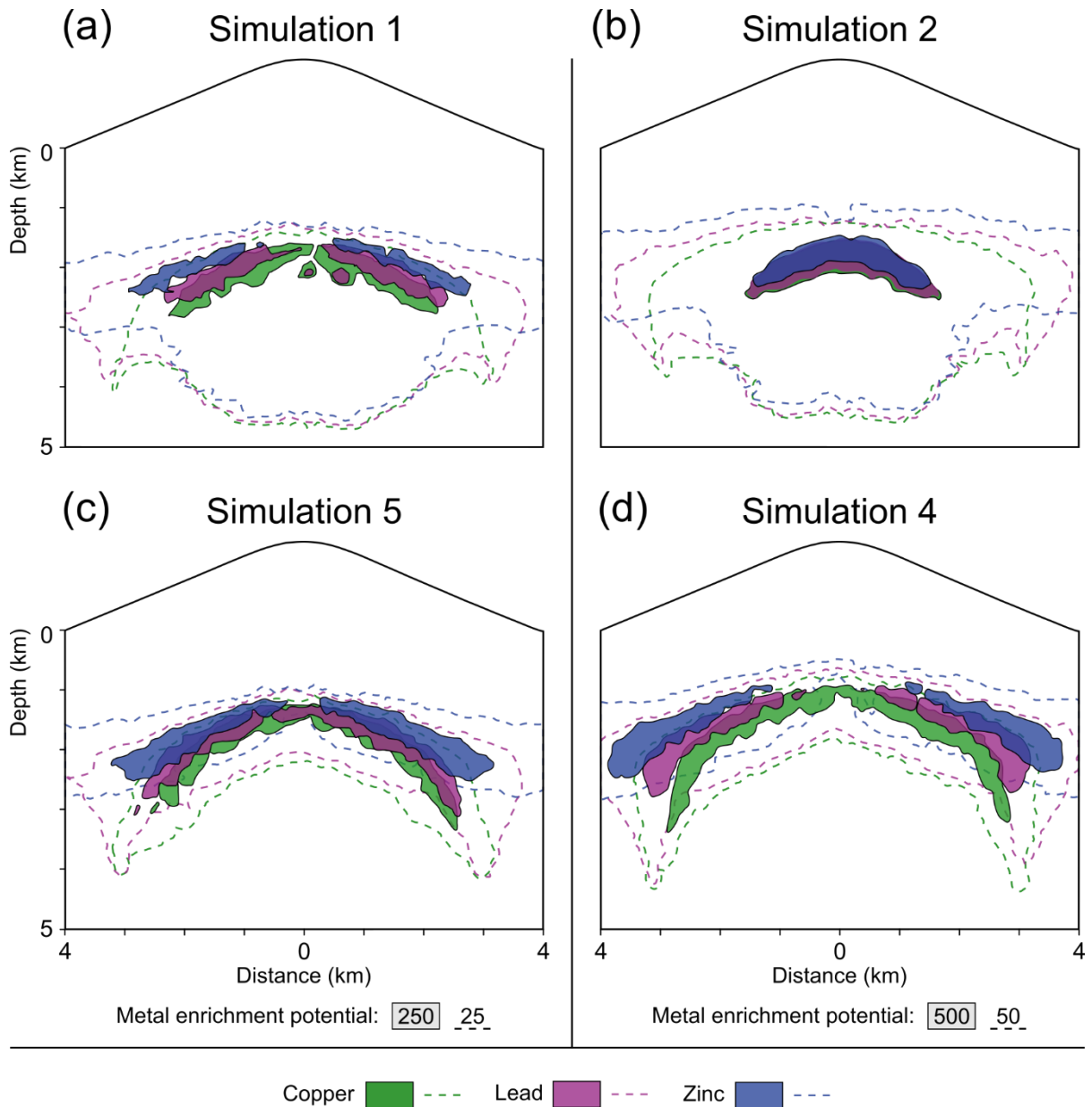
Figure 29 Modeled ore shells after 100 kyrs for simulations without (a, b) and with (c, d) remobilization. The different thresholds for metal enrichment potentials (25 vs. 5 0; 250 vs. 500) reflect the different fluid release rates controlled by the different reservoir volumes used in the respective simulations.

Our simulations share many similarities with the simulations of Blundy et al. (2021), but diverge in the residence times of metal-enriched magmatic brines formed by phase separation. Whereas Blundy et al. (2021) simulate long-lived brine lenses and propose an economic potential for metal extraction, our simulations suggest a rather transient occurrence of hypersaline brine layers that become diluted by meteoric water incursion and transported out of the system. Fluid mixing is enhanced in our model, because it includes a magma reservoir at 5 km depth as a driver for external convection, whereas Blundy et al. (2021) single out the effect of magmatic volatile injection. The two models also use different parameterizations of the host rock permeability. Hence, the residence times of magmatic brines may depend on permeability evolution and the size

and depth of the underlying magma reservoir - parameters that so far are typically not well constrained in both fossil and active systems.

The modeled physical hydrology and its geochemical implications rely on a number of simplifications, with some being intentional to reduce the complexity of the system while others are due to a lack of adequate data or numerical tools. Our modeling efforts are still restricted by limitations in the formulation of physical and chemical processes, e.g. the dynamic permeability evolution at brittle and ductile conditions, fluid-rock reactions influencing variations in pH, redox conditions, sulfide availability, mineral chemistry and species of aqueous fluids which can have a significant effect on metal solubilities (Kouzmanov and Pokrovski 2012). Lowering the pH value from 5 to 4, for example, may increase the metal contents and solubilities of the single-phase fluid by one order of magnitude for Cu and two orders of magnitudes for both Pb and Zn (Kouzmanov and Pokrovski 2012). Such complexities will only be resolvable once full reactive-transport modeling for magmatic-hydrothermal systems should become possible. However, our simulations can already be used to gain new insights into the feasibility of ore formation by cooling and dilution of magmatic fluids.

4.5 Conclusions

We investigated the role of phase separation, brine formation and remobilization on base metal precipitation in porphyry Cu systems using an advanced numerical model that incorporates published temperature- and salinity-dependent metal solubilities. Based on these simplified parameterizations, the simulations suggest some first-order feedbacks between physical hydrology and geochemistry:

1) Our simulations can reproduce the general pattern of metal zoning with lateral extents of up to several kilometers and Pb-Zn mineralization being peripheral to Cu-mineralization for scenarios that avoid halite saturation by cooling and dilution of magmatic brines due to significant incursion of meteoric water.

2) The vapor and brine phases of the two-phase ore-stage fluid ascend together with different residence times, but still in contact with each other at all times. The brine phase becomes enriched in base metals due to preferential partitioning, but remains metal-undersaturated even for saturated primary single-phase input fluids if solubilities increase non-linearly with fluid salinities.

3) Our simulations were able to produce distinct ore shells, especially when the model setups accounted for potential remobilization of metals followed by reprecipitation. Saturation of solid halite can lead to high-grade deposits with simultaneous precipitation of ore

metals, which is in contrast with characteristic vein types at the deposits, but therefore emphasizes the importance of remobilization for future modeling approaches.

4) Brine lenses underneath stratovolcanoes are transient features, leading to direct ore formation rather than longer-term storage of a metal-rich brine phase.

5) Future simulations should include improved thermodynamic models, comprising pH, redox, chloride and bisulfide complexing to provide more detailed insight into the relevant geochemical processes including the role of fluid-rock reactions.

Data Availability

The study uses the software CSMP++ and the algebraic multi-grid solver SAMG, which are subject to licensing via https://mineralsystems.ethz.ch/software/csmp.html
and
https://www.scai.fraunhofer.de/de/geschaeftsfelder/schnelle-loeser/produkte/samg.html.
The necessary information on the numerical method and the simulation setups is provided in the methods section and the references therein (Weis, 2015; Weis et al., 2012, 2014).

Acknowledgments

5 Numerical constraints on the magmatic-hydrothermal fluid evolution forming the Pirquitas Sn-Ag-Pb-Zn deposit in NW Argentina

Stoltnow M.[1,2], Weis P.[2], Korges M.[1]

[1]*Institute of Geosciences, University of Potsdam, Karl-Liebknecht-Straße 24/25, 14476 Potsdam, Germany*

[2]*GFZ German Research Centre for Geosciences, 14473 Telegrafenberg, Germany*

Abstract

The epithermal Pirquitas Sn-Ag-Pb-Zn mine in NW Argentina is hosted in a domain of metamorphosed sediments without geological evidence for volcanic activity within a distance of about 10 km from the deposit. However, recent geochemical studies of ore-stage fluid inclusions indicate a significant contribution of magmatic volatiles. We tested different formation models by applying an existing numerical process model for porphyry-epithermal systems with a magmatic intrusion located either at a distance of about 10 km underneath the nearest active volcano or hidden underneath the deposit. The results show that the migration of the ore fluid over a 10-km distance results in metal precipitation by cooling before the deposit site is reached. In contrast, simulations with a hidden magmatic intrusion beneath the Pirquitas deposit are in line with field observations, which include mineralized hydrothermal breccias in the deposit area.

5.1 Introduction

Magmatic-hydrothermal systems form a variety of ore deposits at different proximities to upper-crustal hydrous magma chambers, ranging from greisenization in the roof zone of the intrusion, porphyry mineralization at intermediate depths to epithermal vein deposits near the surface (e.g., Hedenquist and Lowenstern 1994; Sillitoe 2010). Base metal zoning can extend horizontally by distances of up to 8 km, typically containing a proximal Cu-rich core region surrounded by Pb-Zn-Ag mineralization at more distal settings (Lang and Eastoe 1988; Sillitoe 2010). The physical transport processes and chemical precipitation mechanisms vary between deposit types and are often still debated. For this study, we investigated the fluid evolution from proximal to distal settings at the epithermal Pirquitas Sn-Ag-Pb-Zn Mine in NW Argentina, where the origin of the mineralizing fluids is unclear.

The Pirquitas Mine is suggested to be the southernmost of the polymetallic epithermal deposits of the Central Andean Tin Belt (CATB; Fig. 30) (e.g., Paar et al. 2000; Passamani et al. 2020) and its formation is a topic of debate. While the Peruvian and Bolivian deposits of the CATB have a clear association with Miocene magmatism (e.g., Grant et al. 1979), Pirquitas lacks a direct connection to magmatic activity. However, there is evidence from noble gas isotopes for magmatic fluid contribution to the ore fluid, which formed the Pirquitas mineralization (Desanois et al.

2019) and the presence of the Cortaderas breccia, which is suggested to be underlain by an inferred intrusion (Slater et al. 2021).

Figure 30 Map of the southern sector of the Central Andean Tin Belt with the location of the Pirquitas deposit in the southern-most part. Miocene porphyry and subvolcanic intrusions, caldera structures, major WNW-trending lineaments, and fault zones as well as the dominant host rock litho-logies are shown (modified from Passamani et al. 2020).

Passamani et al. (2020) propose that a complex magmatic-hydrothermal fluid system could be fed from the nearby Granada volcano and the Coranzuli caldera, which are connected by the Lipez lineament over a distance of ~30 km (Fig. 30). This model suggests that the formation of the Pirquitas system may include ore fluids expelled from a magma reservoir underlying the Granada volcano, which would have travelled a distance of at least 8 km (Fig. 31a).

As an alternative explanation, the model infers a hidden intrusion located underneath the Pirquitas Mine (Fig. 31a). Such an intrusion would promote fluid temperatures of >500°C as suggested for the Bolivian deposits (e.g., Sugaki et al. 1988), which have, however, not been observed in Pirquitas yet, where the maximum temperature estimate from fluid inclusion analyses is <400°C (Desanois et al. 2019).

Analyses of fluid inclusions hosted in hydrothermal vein quartz and ore minerals from the Pirquitas Mine indicate that the hydrothermal system was characterized by mixing of magmatic fluids and meteoric water (Desanois et al. 2019). This model also proposes that there might be a hidden high-grade Ag (± base metals) lens at depth, which may have served as a source region for later remobilization eventually forming the mineralization at Pirquitas. This interpretation is supported by noble gas analyses (Desanois et al. 2019) and the existence of hydrothermal breccias with mineralized clasts at locations near the open pit mine, which indicates that the hydrothermal system extends to greater depth and suggests that the fluid source may rather be located underneath the deposit.
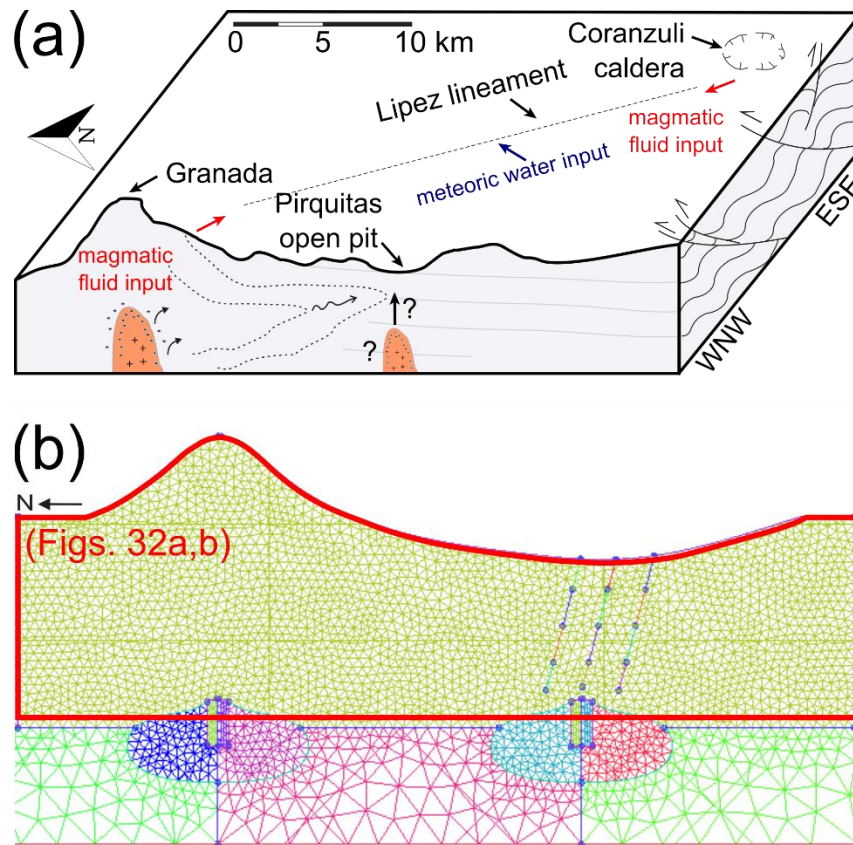
Figure 31 (a) Conceptual model showing the Lipez lineament connecting the Granada stratovolcano and the Coranzuli caldera, forming a complex magmatic-hydrothermal system with potential ore fluids either being related to the Granada volcano or to a hidden proximal intrusion at depth below the Pirquitas open-pit mine (modified from Passamani et al. 2020). (b) Excerpt of the modelling mesh approximating the geological setting including the two hypothesized magma reservoirs at about 5 km depth.

5.2 Methods

We use numerical simulations to test the different conceptual formation models. Based on the parametrization of Weis et al. (2012), we performed simulations testing the hydrology of mineral systems, where mineralization formed (i) at a distance of about 10 km and (ii) directly above a magmatic intrusion (Fig. 31b). Our approaches include a modelling setup with a total extension of 40 x 9 km. Both the stratovolcano, which rises 2 km above, and an assumed valley, which has incised to a maximum of 1 km below the ambient level, are exaggerating field observations to achieve broader fluid transport by topography-driven groundwater flow. The geometry includes two magma reservoirs, which can be switched on and off in the model configurations for either distal (simulation 1, Fig. 32a) or proximal (simulation 2, Fig. 32b) settings.

The numerical model simulates the release of magmatic fluids from a cooling and crystallizing magma reservoir and its interaction with a dynamic permeability model for hydraulic

fracturing that mimics the formation of stockwork veining, and the convection of meteoric fluids. Previous simulations have shown how the interplay of these processes self-organizes into a hydrological divide between a magmatic fluid plume at high temperatures and high pressures and a hydrothermal system with mixed magmatic-meteoric fluids at lower temperatures and pressures (for a detailed description see Weis et al. 2012).

5.3 Results and Interpretation

With the numerical modeling approach, we can test different formation models for the Pirquitas Deposit, which are based on geochemical (Desanois et al. 2019; Slater et al. 2021), geophysical (Soler et al. 2007) and structural geological (Passamani et al. 2020) studies. Figures 32a and 32b display the evolution of the hydrology after a simulation time of 15 kyrs, which represents the broadest migration of the temperature fronts.

5.3.1 Distal Setting

Simulation 1 includes a magma reservoir underlying a stratovolcano. The vertical extension of the stratovolcano promotes the flow of meteoric water towards greater depth suppressing the ascent of magmatic fluid, the accompanied temperature front, and the formation of domains with bulk salinities of >40 wt% NaCl eq. (Fig. 32a). Although fluids containing bulk salinities up to 20 wt% NaCl eq. can travel distances of up to 10 km and thus reach the site of the Pirquitas mineralization, fluid temperatures in this area are limited to <100°C.

Based on simulation results from Stoltnow et al. (2023), which used base metal solubilities reported by Kouzmanov and Pokrovski (2012), this thermal evolution implies that the area in which base metals may accumulate to economic values is restricted to the domain directly overlying the injection point. In this domain, the pore fluid factor is below 0.7 (beginning of the hydrostatic pressure regime) and extends to the 200°C isotherm (Fig. 32a). Consequently, the simulation representing a distal source for the fluids and metals may rather produce an economic mineralization underneath the Granada volcano at a distance of some 10 km, but unlikely produced the primary mineralization at Pirquitas.

5.3.2 Proximal Setting

In contrast, simulation 2 tests the proximal setup with an inferred magma reservoir right beneath the open-pit mine of the Pirquitas Deposit (Fig. 32b). The vertical depression located above the magma chamber causes a strong inflow of meteoric fluids, which focuses ascending magmatic fluids and the accompanying temperature front. Although the domain right beyond the hydrological divide is characterized by bulk salinities >80 wt% NaCl eq. due the local and temporal saturation of the fluids in solid halite, the overall migration of saline fluids (>0 wt% NaCl eq.) is restricted to the focused region between the hydrological divide and the Pirquitas open pit (Fig. 32b).

Similarly, the area of potential economic metal enrichment is more focused (~2 km horizontal extension) compared to the distal setting (~4 km horizontal extension) and reaches shallower depths of ~2 km. Furthermore, higher bulk salinities along the outer part of the hydrological divide could support an overall higher metal enrichment potential (Stoltnow et al. 2023) and higher ore grades. The modelled depth level, temperature, salinity, and mixed origin (magmatic and meteoric) of hydrothermal ore formation are in agreement with recent findings (Desanois et al. 2019; Slater et al. 2021). In addition, the modelled transition from lithostatic to hydrostatic fluid pressures at the hydrological divide would be in line with the presence of a hydrothermal breccia below the Pirquitas Mine.

5.4 Discussion and Conclusions

Our modeling results show that fluids necessary to form Pirquitas-like mineralization may not be transported farther than 2-3 km in both horizontal and vertical directions from the porphyry region of the magma reservoir (Fig. 32b). Later remobilization can lead to further transport and reprecipitation of base metals at further distances (Stoltnow et al. 2023), but is unlikely to be permissive with the hypothesis of the Pirquitas mineralization being fed by a magma reservoir underneath the Granada stratovolcano (e.g., Passamani et al. 2020).

Instead, the simulations rather highlight the necessity of an intrusion underneath or in closer proximity to a Pirquitas-like mineralization, which has also been proposed previously (Desanois et al. 2019; Passamani et al. 2020; Slater et al. 2021). These findings are supported by the occurrence of hydrothermal breccias at both the Pirquitas Deposit and the Cortaderas Deposit some 500 m north of the Pirquitas open pit, which is proposed to be underlain by a hidden intrusion (Slater et al. 2021).
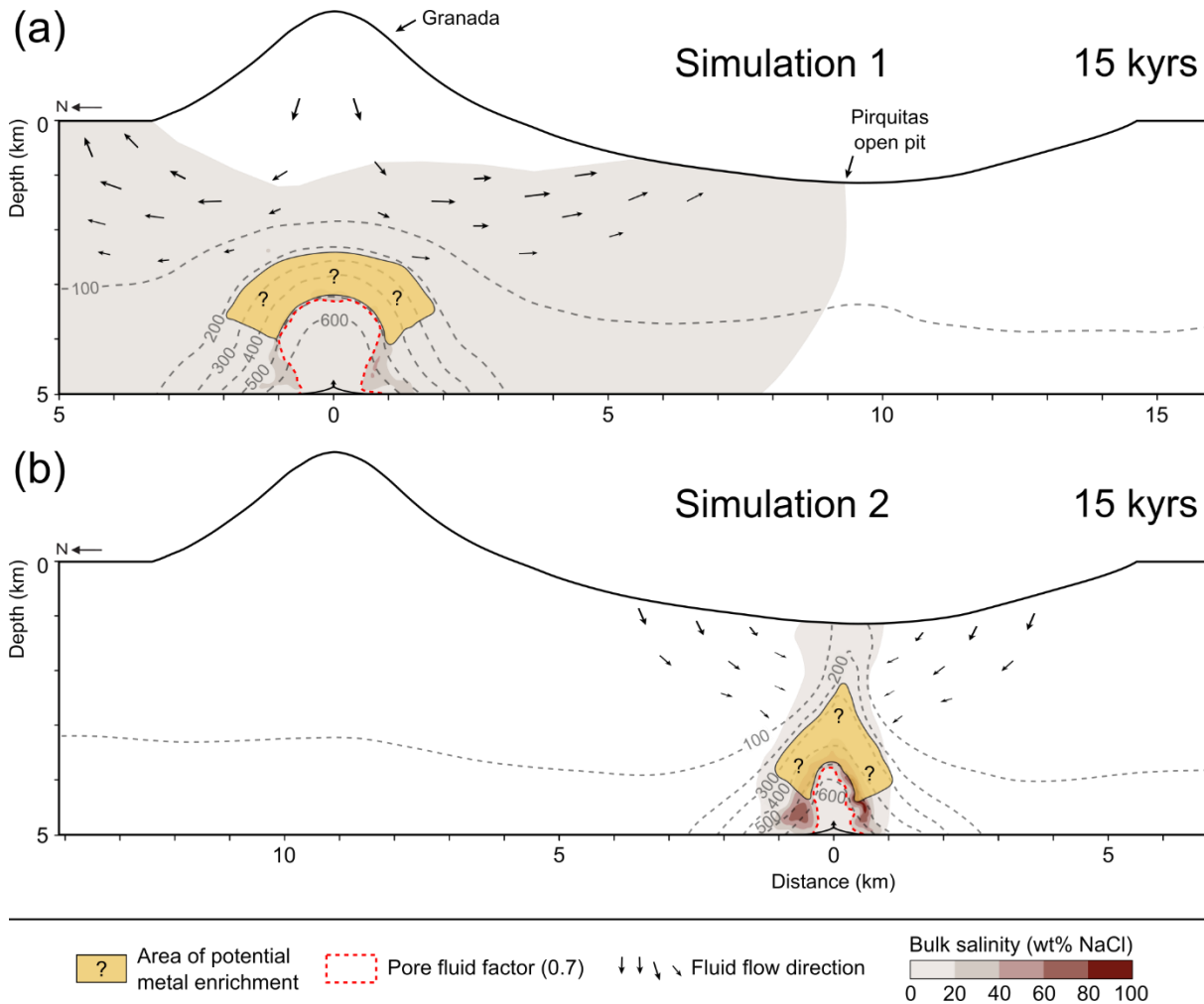
Figure 32 Bulk fluid salinity (colors) and isotherms (dashed lines) of the modeled Pirquitas hydrothermal system after 15 kyrs with a magma reservoir beneath the Granada stratovolcano (a) and beneath the Pirquitas deposit (b). The extent of areas with potential and economic metal enrichment are based on modeling results in Stoltnow et al. (2023). The pore fluid factor (fluid pressure divided by lithostatic pressure) of 0.7 indicates the transition from near-hydrostatic to near-lithostatic fluid pressures. Arrows at a depth of 5 km refer to the fluid injection location at the cupola region of the magma reservoir.

The simulations rely on a number of simplifications. In this reconnaissance study, we reduced the geological complexity to investigate first-order controls on the ore-forming hydrothermal system. To obtain a lateral transport by 10 km from the cupola region of the magma reservoir, the model required a significant topographic gradient from the volcano summit to the deposit location as a driving force for the convection of meteoric fluids. However, the same process also leads to strong cooling of the metal-bearing magmatic fluids. Further simulations could include more geological heterogeneity in the permeability structure, e.g., by including fault zones or low-permeability lithocaps, which may support lateral fluid migration with less cooling.

In general, the simulations show that the quantification of first-order controls on the physical hydrology at the porphyry-epithermal transition can be instrumental to understand the ore-forming system beyond the deposit scale.

Acknowledgements

6 Conclusions and outlook

This thesis provides new insights into the formation of different styles of mineralization located at different proximities to the intrusion in magmatic-hydrothermal systems along the American Cordillera. The two main objectives addressed ore-forming processes along the porphyry to epithermal transition to specify the potential existence and location of high-grade mineralization elsewhere in the fluid system. These objectives were (1) to constrain the fluid origin and evolution in magmatic-hydrothermal systems performing various (fluid inclusion) geochemical techniques and to quantify the processes accompanying the fluid evolution via (2) mineral geochronology and (3) numerical modeling.

(1) The first geochemical study on the Sweet Home Mine in Colorado (USA) (Chapter 2) includes a large dataset of various fluid inclusion and isotope techniques. The results of this study provide new constraints on the evolution of fluid systems related to peripheral mineralization of Climax-type porphyry Mo deposits.

(2) The second geochemical study provides both robust Re-Os molybdenite ages and robust multimineral Rb-Sr isochron ages for gangue minerals from the Sweet Home Mine. These age data indicate that mineralization in the SHM was formed by two separate, unrelated events, i.e., a Late Cretaceous (Laramide-related) event and an Oligocene (Rio Grande Rift-related) event.

(3) The numerical simulations presented in this thesis, both generic for porphyry Cu environments and specific for the Pirquitas Sn-Ag-Pb-Zn deposit in NW Argentina, provide an advanced numerical process model for the quantification of ore-forming processes in magmatic-hydrothermal systems. The results of these studies allow conclusions about the position of ore-related intrusions.

6.1 Fluid evolution in magmatic-hydrothermal systems

The Sweet Home mine in the Colorado Mineral Belt has been proposed to represent an endmember of Climax-type porphyry Mo peripheral mineralization (Misantoni et al. 1998; Lüders et al. 2009). Sweet Home is characterized by late Cretaceous Mo mineralization hosted by veinlets and coatings on fault gouge and Oligocene early-stage Fe-W-Zn-greisen, main-stage Pb-Zn-Cu-Ag-rhodochrosite, and late-stage fluorite-apatite-barite assemblages. Ore and gangue minerals of the

Oligocene assemblages were investigated with various fluid inclusion and stable isotope techniques.

The results in Chapter 2 provide compelling evidence that the mineralization formed from magmatic fluids and meteoric water, which mixed to different proportions with time as suggested by Hall et al. (1974) and Lüders et al. (2009). These findings are in conflict with a genetic model that invokes an exclusive magmatic origin of peripheral vein-type mineralization for Climax-type deposits (e.g. Stein and Hannah 1985; Wallace 1995; Seedorff and Einaudi 2004a; Seedorff and Einaudi 2004b; Audétat and Li 2017).

The early Fe-W-Zn-greisen stage is suggested to be related to magmatic-dominated fluids ($\sim$400°C) enriched in volatiles, such as CO_2, H_2S/SO_2, and noble gases, which are most likely derived from mantle sources. Progressive mixing of the early ore fluid with meteoric water during heat-driven fluid convection resulted in lower temperatures (<300°C) and fluid dilution, possibly leaching of metals from crustal rocks, and formed the Pb-Zn-Cu-Ag-rhodochrosite main stage. In the waning stages of the magmatic-hydrothermal system, meteoric fluids dominated and formed the barren late-stage mineralization.

Numerical simulations in a generic porphyry Cu environment (Chapter 4) investigated the fluid evolution from proximal to distal settings and thereby considered the process of fluid mixing in ore formation. This study presented new advances of an existing numerical model for porphyry Cu systems considering constraints on temperature- and salinity-dependent solubility of Cu, Pb and Zn in the ore-forming fluid, including partitioning during phase separation, which has variably been related to metal zoning (Cu-Mo to Zn-Pb-Ag). The results show that salinity increases in an evolving hydrothermal system generate metal-undersaturated bulk fluids and that ore precipitation from these fluids may be achieved by contrasting mechanisms. These are (i) mixing with meteoric water, which is characterized by cooling and dilution of the ore fluid accompanied by the production of zoned ore patterns (Cu to Pb to Zn or Cu to Zn to Pb), and (ii) halite saturation, which causes an abrupt decrease in salinity and thus increase in metal saturation (and precipitation). The latter scenario may be comparable with the occurrence of salt melts, e.g., in porphyry Au deposits, such as Lindero in the Southern Puna Plateau (Argentina) (Simón et al. 2021). Our simulations further showed that in an evolving hydrothermal system, redissolution of precipitated metals may occur and lead to zoned ore shell patterns in more peripheral locations.

6.2 Dating ore formation in magmatic-hydrothermal systems

The geochemical study in Chapter 3 presented two different dating techniques, namely (i) Re-Os molybdenite dating and (ii) Rb-Sr multimineral (isochron) dating, which yielded both robust Late Cretaceous and robust Oligocene ages, respectively. Both ages constrain the age of the latest deformation along the Contact Structure (which could not be determined by direct dating). Late Cretaceous molybdenite coexist with Oligocene minerals in the same vein system, a feature that precludes molybdenite recrystallization or reprecipitation by Oligocene ore fluids.

The multimineral (mainly gangue minerals from greisen assemblages) Oligocene age supports Sweet Home's proposed Climax-type peripheral endmember character (Misantoni et al. 1998) and the association with the tectonomagmatic setting, which accompanied the opening of the Rio Grande Rift (e.g., Chapin 2012). In contrast, the Late Cretaceous Re-Os molybdenite age predates major porphyry Mo mineralization in the Colorado Mineral Belt and northern New Mexico (White et al. 1981; Shannon et al. 1984; Bookstrom et al. 1987; Markey et al. 2007; Zimmerer and McIntosh 2012). The formation of the Mo mineralization found at the Sweet Home Mine can be related to magmatic intrusions, which accompanied the Laramide Orogeny, (e.g., Mutschler et al. 1987). In general, these intrusions did not result in major Mo mineralization in the Colorado Mineral Belt, in contrast to temporally-related intrusions in the Basin-and-Range province and Canada.

6.3 Constraining ore-forming processes in magmatic-hydrothermal systems via numerical modeling

The numerical modeling studies of this thesis quantitatively investigated the roles of vapor-brine separation, halite saturation, initial metal contents, fluid mixing and remobilization as first-order controls of the physical hydrology of ore formation. The results showed that the release rate of the fluids from the magma reservoir affects the location of the thermal and saline fronts and can lead to contrasting mechanisms for ore precipitation as described above: lower fluid release rates produce zoned ore shells due to fluid mixing in absence of halite saturation; higher release rates result in halite saturation of the (pure) magmatic ore fluid and metal co-precipitation without significant metal zoning. The latter relies on the assumption in our model

setup that halite cannot incorporate any metals. The lack of significant metal zoning can be observed in some porphyry-related mineralization (e.g. Hui et al. 2021) but stands in contrast to the typical distinction between Cu-bearing ore stage veins and Pb-Zn-veins in porphyry systems. The variation of initial metal contents of the primary magmatic fluid can affect the final metal precipitation sequence, however, may produce metal contents, which are usually not observed in the field. The most efficient process related to the formation of potentially overall economic and zoned Cu, Pb, and Zn shells in our simulations is the redissolution of precipitated metals. This process decouples halite saturation, if present, from ore precipitation and shifts the ore shells to the most peripheral zones.

Numerical simulations set up on the NW Argentinian Sn-Ag-Pb-Zn-Pirquitas deposit focus on fluid evolution during a horizontal fluid migration of about 10 km after expulsion from an intrusion underneath a stratovolcano. The results of these simulations show that ore fluids with high salinity (up to 20 wt% NaCl equivalent) can be transported over this distance. However, fluid temperatures upon arrival at the proposed depositional site (Passamani et al. 2020) do not exceed 100°C and, consequently, are not capable of forming Pirquitas-like mineralization. Consequently, to form a Pirquitas-like mineralization, the ore deposit likely directly overlies or has formed at least adjacent to an intrusion as proposed by Slater et al. (2021).

6.4 Position of the mineralization along the porphyry-epithermal transition

The individual studies in this thesis address major and minor ore deposits located in varying proximity to an igneous intrusion along the porphyry-epithermal transition. As suggested by Sillitoe (2010), studies on even small-scale mineralization along this transition have the potential to indicate the presence of large-scale mineralization elsewhere in the magmatic-hydrothermal system.

The Sweet Home mine is located ~8 km SE of the giant Climax Mo porphyry deposit. Based on fluid inclusion and radiogenic isotope data Lüders et al. (2009) proposed the mineralization found at the Sweet Home mine to be underlain by a hidden porphyry intrusion similar to Climax. Additional fluid inclusion, and stable and noble gas isotope data (Chapter 2) could confirm the magmatic contribution and added a mantle component to the genetic model. Recent Mo discoveries along a major normal fault supported the relationship to Climax. Geochronological data gathered from molybdenite and greisen-stage gangue minerals (Chapter 3), however, unraveled the late Cretaceous history of the Sweet Home Mine, suggesting a single magmatic

event, without (significant) impact on later major porphyry Mo mineralization in the Colorado Mineral Belt and northern New Mexico.

The Sn-Ag-Pb-Zn Pirquitas Mine has been described as Sn-Ag-polymetallic IS-type with lacking connection to a proximal magmatic intrusion (e.g. Malvicini 1978; Paar et al. 2000; Desanois et al. 2019; Passamani et al. 2020). The presence of a deposit-related intrusion directly beneath Pirquitas is supported by the fact that vertical drilling of up to 800 m depth in the mine area has not hit any igneous rocks so far (Soler et al. 2007). For the Ag-Pb-Zn-Sn Cortaderas breccia body located some 500 m north of the Pirquitas open pit, however, the existence of a magmatic intrusion directly beneath or adjacent has been proposed (Slater et al. 2021). Both our modeling results and the occurrence of breccias immediately north of the open pit suggest the presence of an intrusion in the near vicinity.

6.5 Outlook

This thesis has been initially set up on sampling campaigns in NW Argentina for geochemical analysis and corresponding numerical simulations. The change in the thematic focus of the studies is due to unforeseen complications, with a major contribution by a global pandemic. What was originally planned and how the originally planned research questions can still be investigated is described in Appendix A. In the following, themes of future research related to the previous chapters are listed.

- Geochemical data have revealed fluid mixing of magmatic fluids with large amounts of meteoric water as most likely mechanism for the formation of the Sweet Home mineralization. Our study shows that the combination of FI studies including noble gas and stable isotope analyses with stable isotope analysis of ore and gangue minerals has the potential to characterize the formation of deep hydrothermal vein mineralization. Whether Climax-type Mo mineralization in ore shells above porphyry stocks can be attributed to a similar mixing model requires further evidence.

- Geochronological data have revealed the existence of late Cretaceous Mo in the Colorado Mineral Belt, which is coincident with major Mo mineralization of porphyry Mo deposits in the Basin-and-Range Province. Due to the lack of Re-Os molybdenite age data in the Colorado Mineral Belt it remains unclear, if there is more temporal coincidence of Mo mineralization east and west of the Colorado Plateau. Therefore, further Re-Os dating on molybdenite samples from Mo deposits and occurrences in the Colorado Mineral Belt should be considered.

- By now, CSMP++ numerical process models are capable of implementing other functionalities in the simulations including, e.g., 1D line elements and incremental magma growth (Korges et al. 2020; Codeço et al. 2022), which should be considered in further simulations.

- Generally, the modeled physical hydrology and its geochemical implications rely on several simplifications, with some being intentional to reduce the complexity of the system while others are due to a lack of adequate data or numerical tools. Our modeling efforts are still restricted by limitations in the formulation of physical and chemical processes, e.g. the dynamic permeability evolution at brittle and ductile conditions, fluid-rock reactions influencing variations in pH, redox conditions, sulfide availability mineral chemistry and species of aqueous fluids which can have a significant effect on metal solubilities (Kouzmanov and Pokrovski 2012). Such complexities will only be resolvable once full reactive-transport modeling for magmatic-hydrothermal systems should become possible.

- Chapter 5 presents the first numerical simulations to constrain the extent of ore fluid migration in a Pirquitas-related setup. This study can be refined by adding more detailed geological constraints, e.g. country rock permeabilities, varying the brittle-ductile transition, different volumes of the magma chamber, combined release of magmatic fluids from a proximal and distal magma chamber in the same simulation, and the addition of faults or breccias as fluid pathways.

References

Afanasyev A, Blundy J, Melnik O, Sparks S (2018) Formation of magmatic brine lenses via focussed fluid-flow beneath volcanoes. Earth Planet Sci Lett 486:119-128. doi: 10.1016/j.epsl.2018.01.013.

Audétat A (2010) Source and evolution of molybdenum in the porphyry Mo (–Nb) deposit at Cave Peak, Texas. J Petrol 51:1739-1760.

Audétat A (2015) Compositional evolution and formation conditions of magmas and fluids related to porphyry Mo mineralization at Climax, Colorado. J Petrol 56:1519-1546.

Audétat A (2019) The metal content of magmatic-hydrothermal fluids and its relationship to mineralization potential. Econ Geol 114:1033-1056.

Audétat A (2022) A Plea for More Skepticism toward Fluid Inclusions: Part II. Homogenization via Halite Dissolution in Brine Inclusions from Magmatic-Hydrothermal Systems is Commonly the Result of Postentrapment Modifications. Econ Geol. doi: 10.5382/econgeo.4974.

Audétat A, Li W (2017) The genesis of Climax-type porphyry Mo deposits: Insights from fluid inclusions and melt inclusions. Ore Geol Rev 88:436-460.

Audétat A, Günther D, Heinrich CA (2000) Causes for large-scale metal zonation around mineralized plutons: Fluid inclusion LA-ICP-MS evidence from the Mole Granite, Australia. Econ Geol 95:1563-1581.

Audétat A, Dolejš D, Lowenstern JB (2011) Molybdenite saturation in silicic magmas: occurrence and petrological implications. J Petrol 52:891-904.

Bailey DK (1987) Mantle metasomatism—perspective and prospect In: Fitton J, Upton B (eds) Alkaline Igneous Rocks. Geol Soc London Spec Publ, pp 1-13.

Bailey DK, Macdonald R (1987) Dry peralkaline felsic liquids and carbon dioxide flux through the Kenya rift zone Magmatic Processes: Physicochemical Principles Geochem Soc Spec Publ, pp 91-105.

Bailey DK, Hampton CM (1990) Volatiles in alkaline magmatism. Lithos 26:157-165.

Barbá KE, Nelson EP, Misantoni D, Hitzman MW, Layer PW (2005) Structural controls on mineralized veins in the Sweet Home Mine, Alma district, Colorado Geol Soc Nevada Symp. pp 698-708.

Barton PB, Chou I (1993) Calculation of the vapor-saturated liquidus for the $NaCl-CO_2-H_2O$ system. Geochim Cosmochim Acta 57:2715-2723.

Bartos PJ, Nelson EP, Misantoni D (2007) The Sweet Home rhodochrosite specimen mine, Alma District, Central Colorado: the porphyry molybdenum–fluorine connection. Miner Deposita 42:235-250.

Behre CH, Jr (1953) Geology and ore deposits of the west slope of the Mosquito Range Professional Paper 235. US Geol Surv, pp 176.

Birck JL, Barman MR, Capmas F (1997) Re-Os isotopic measurements at the femtomole level in natural samples. Geostandard Newslett 21:19-27.

Bloom MS (1981) Chemistry of inclusion fluids; stockwork molybdenum deposits from Questa, New Mexico, Hudson Bay Mountain and Endako, British Columbia. Econ Geol 76:1906-1920.

Blundy J, Afanasyev A, Tattitch B, Sparks S, Melnik O, Utkin I, Rust A (2021) The economic potential of metalliferous sub-volcanic brines. R Soc Open Sci 8: 202192:1-28. doi: 10.1098/rsos.202192.

Bodnar R, Lecumberri-Sanchez P, Moncada D, Steele-MacInnis M (2014) 13.5–Fluid inclusions in hydrothermal ore deposits. Treatise on geochemistry 2nd edn Elsevier, Oxford 119:142. doi: 10.1016/b978-0-08-095975-7.01105-0

Bodnar RJ (1993) Revised equation and table for determining the freezing point depression of $H_2O-NaCl$ solutions. Geochim Cosmochim Acta 57:683-684.

Bodnar RJ (1995) Fluid-inclusion evidence for a magmatic source for metals in porphyry copper deposits. Mineralogical Association of Canada Short course series: 23:139-152.

Bodnar RJ, Reynolds TJ, Kuehn CA (1985) Fluid inclusion systematics in epithermal systems In: Berger BR, Bethke PM (eds) Geology and geochemistry of epithermal systems. Rev Econ Geol, pp 73-97.

Bookstrom AA (1981) Tectonic setting and generation of Rocky Mountain porphyry molybdenum deposits In: Dickinson W, Payne W (eds) Relations of Tectonics to Ore Deposits in the Southern Cordillera Arizona Geol Soc Digest, pp 215-226.

Bookstrom AA (1989) The Climax-Alma granite batholith of oligocene age and the prophyry molybdenum deposits of Climax, Colorado, USA. Engineering Geol 27:543-568.

Bookstrom AA, Naeser CW, Shannon JR (1987) Isotopic age determinations, unaltered and hydrothermally altered igneous rocks, north-central Colorado Mineral Belt. Isochron West 49:13-20.

Bookstrom AA, Carten RB, Shannon JR, Smith RP (1988) Origins of bimodal leucogranite-lamprophyre suites, Climax and Red Mountain porphyry molybdenum systems, Colorado: petrologic and strontium isotopic evidence. Colorado School of Mines Quarterly 83:1-24.

Brauns CM (2001) A rapid, low-blank technique for the extraction of osmium from geological samples. Chemical Geology 176:379-384.

Brauns CM, Hergt JM, Woodhead JD, Maas R (2000) Os isotopes and the origin of the Tasmanian dolerites. J Petrol 41:905-918.

Burchfiel BC, Cowan DS, Davis GA (1992) Tectonic overview of the Cordilleran orogen in the western United States In: Burchfiel BC (ed) The Cordilleran orogen: Conterminous US. Boulder, Colorado, Geological Society of America, The geology of North America, pp 407-479, v. G-403.

Burnham CW (1979) Magmas and hydrothermal fluids In: Barnes HL (ed) Geochemistry of hydrothermal ore deposits. 2 edn. John Wiley & Sons, New York, pp 71-136.

Caffe PJ (2013) Petrografía de muestras de testigo y roca. Mina Chinchillas prepared for Golden Arrow Resources.

Caffe PJ, Coira BL (2008) Depósitos epitermales polimetálicos asociados a complejos volcánicos dómicos: Casa Colorada, Pan de Azúcar, Chinchillas y Cerro Redondo. Relatorio del XVII Congreso Geológico Argentino, Jujuy.

Candela PA (1989) Felsic magmas, volatiles, and metallogenesis. Rev Econ Geol 4:223-233.

Candela PA, Holland HD (1986) A mass transfer model for copper and molybdenum in magmatic hydrothermal systems; the origin of porphyry-type ore deposits. Econ Geol 81:1-19.

Carten RB, White WH, Stein HJ (1993) High-grade granite-related molybdenum system: classification and origin In: Kirkham R, Sinclair W, Thorpe R, Duke J (eds) Mineral deposit modeling. Geol Assoc Can Spec Pap, pp 521-554.

Carten RB, Geraghty EP, Walker BM, Shannon JR (1988) Cyclic development of igneous features and their relationship to high-temperature hydrothermal features in the Henderson porphyry molybdenum deposit, Colorado. Econ Geol 83:266-296.

Catchpole H, Kouzmanov K, Putlitz B, Seo JH, Fontboté L (2015) Zoned base metal mineralization in a porphyry system: Origin and evolution of mineralizing fluids in the Morococha district, Peru. Econ Geol 110:39-71. doi: 10.2113/econgeo.110.1.39.

Cathles LM (1977) An analysis of the cooling of intrusives by ground-water convection which includes boiling. Econ Geol 72:804-826.

Chapin CE (2012) Origin of the Colorado mineral belt. Geosphere 8:28-43.

Chen P, Zeng Q, Zhou T, Chen J (2021a) He, Ar, and S isotopic constraints on the origin of the Dasuji porphyry Mo deposit, China. Arab J Geosci 14:1-14.

Chen P, Zeng Q, Guo W, Chen J (2021b) The source, enrichment and precipitation of ore-forming elements for porphyry Mo deposit: Evidences from melt inclusions, biotite and fluorite in Dasuji deposit, China. Ore Geol Rev 135:104205.

Chi G, Diamond LW, Lu H, Lai J, Chu H (2021) Common problems and pitfalls in fluid inclusion study: A review and discussion. Minerals 11(1),7:1-23.

Chicharro E, Boiron M-C, López-García JÁ, Barfod DN, Villaseca C (2016) Origin, ore forming fluid evolution and timing of the Logrosán Sn–(W) ore deposits (Central Iberian Zone, Spain). Ore Geol Rev 72:896-913.

References

Cline JS, Bodnar RJ (1994) Direct evolution of brine from a crystallizing silicic melt at the Questa, New Mexico, molybdenum deposit. Econ Geol 89:1780-1802.

Cline JS, Hofstra AH, Muntean JL, Tosdal RM, Hickey KA (2005) Carlin-type gold deposits in Nevada: Critical geologic characteristics and viable models. Econ Geol 100:451-484.

Codeço MS, Weis P, Andersen C (2022) Numerical modeling of structurally controlled ore formation in magmatic-hydrothermal systems. Geochem Geophys 23, e2021GC010302.

Cook HE (2015) The evolution and relationship of the western North American Paleozoic carbonate platform and basin depositional environments to Carlin-type gold deposits in the context of carbonate sequence stratigraphy In: Pennell WM, Garside LJ (eds) New Concepts and Discoveries, Geological Society of Nevada Symposium Proceedings. pp 1-78.

Cook HE, Corboy JJ (2004) Great Basin Paleozoic carbonate platform: Facies, facies transitions, depositional models, platform architecture, sequence stratigraphy, and predictive mineral host models. US Geological Survey Open-File Report 1078:129.

Cooke DR, Hollings P, Wilkinson JJ, Tosdal RM (2014) Geochemistry of Porphyry Deposits In: Scott SD (ed) Treatise on Geochemistry 2edn. Elsevier, pp 357-381.

Craig H (1961) Isotopic variations in meteoric waters. Science 133:1702-1703.

Creasey SC (1980) Chronology of intrusion and deposition of porphyry copper ores, Globe-Miami district, Arizona. Econ Geol 75:830-844.

Crovetto R, Fernández-Prini R, Japas ML (1982) Solubilities of inert gases and methane in H_2O and in D_2O in the temperature range of 300 to 600 K. J Chem Physics 76:1077-1086.

Cuney M (2010) Evolution of uranium fractionation processes through time: driving the secular variation of uranium deposit types. Econ Geol 105:553-569.

Darling RS (1991) An extended equation to calculate NaCl contents from final clathrate melting temperatures in H_2O-CO_2-NaCl fluid inclusions: Implications for PT isochore location. Geochim Cosmochim Acta 55:3869-3871.

de Graaf S, Vonhof HB, Weissbach T, Wassenburg JA, Levy EJ, Kluge T, Haug GH (2020a) A comparison of isotope ratio mass spectrometry and cavity ring-down spectroscopy techniques for isotope analysis of fluid inclusion water. Rapid Commun Mass Spectrom 34:e8837.

de Graaf S, Lüders V, Banks DA, Sośnicka M, Reijmer JJG, Kaden H, Vonhof HB (2020b) Fluid evolution and ore deposition in the Harz Mountains revisited: isotope and crush-leach analyses of fluid inclusions. Miner Deposita 55:47-62.

DeCelles PG (2004) Late Jurassic to Eocene evolution of the Cordilleran thrust belt and foreland basin system, western USA. Am J Sci 304:105-168.

Deino A, Keith JD (1998) Ages of volcanic and intrusive rocks in the Bingham mining district, Utah. Society of Economic Geologists, Guidebook Series 29:91-100.

DePaolo DJ (1981) Neodymium isotopes in the Colorado Front Range and crust–mantle evolution in the Proterozoic. Nature 291:193-196.

Desanois L, Lüders V, Niedermann S, Trumbull RB (2019) Formation of epithermal Sn-Ag-(Zn) vein-type mineralization at the Pirquitas deposit, NW Argentina: Fluid inclusion and noble gas isotopic constraints. Chem Geol 508:78-91.

Desborough GA, Sharp WN (1978) Tantalum, uranium, and scandium in heavy accessory oxides, Climax molybdenum mine, Climax, Colorado. Econ Geol 73:1749-1751.

Desborough GA, Mihalik P (1980) Accessory minerals in the igneous host of molybdenum ore, Henderson mine, Colorado US Geol Surv Open-File Report 80-661, 19 p.

Diamond LW (1994) Introduction to phase reactions of CO_2–H_2O fluid inclusions In: De Vivo B, Frezotti ML (eds) Fluid inclusions in minerals: methods and application. Virginia Tech, Blacksburg, pp 131-158.

Dickinson WR (2002) The Basin and Range Province as a composite extensional domain. Int Geol Rev 44:1-38.

Dickinson WR (2004) Evolution of the North American cordillera. Annu Rev Earth Planet Sci 32:13-45.

Dickinson WR (2006) Geotectonic evolution of the Great Basin. Geosphere 2:353-368.

Driesner T (2007) The system H$_2$O–NaCl. Part II: Correlations for molar volume, enthalpy, and isobaric heat capacity from 0 to 1000°C, 1 to 5000 bar, and 0 to 1 XNaCl. Geochim Cosmochim Acta 71:4902-4919. doi: 10.1016/j.gca.2007.05.026.

Driesner T, Heinrich CA (2007) The system H$_2$O–NaCl. Part I: Correlation formulae for phase relations in temperature–pressure–composition space from 0 to 1000°C, 0 to 5000 bar, and 0 to 1 XNaCl. Geochim Cosmochim Acta 71:4880-4901. doi: 10.1016/j.gca.2006.01.033.

Durisova J, Golias V, Pudilova M, Strnad L, Zak K (1997) Evolution of crustal fluids in a shear zone during retrograde metamorphism, regional uplift, and cooling (the Kašperskë Hory gold deposit, Moldanubian unit, Bohemian Massif). J Geosci 42:52-50.

English JM, Johnston ST (2004) The Laramide orogeny: What were the driving forces? Int Geol Rev 46:833-838.

Farmer GL, Depaolo DJ (1984) Origin of Mesozoic and Tertiary granite in the western United States and implications for Pre-Mesozoic crustal structure: 2. Nd and Sr isotopic studies of unmineralized and Cu-and Mo-mineralized granite in the Precambrian Craton. J Geophys Res 89:10141-10160.

Fekete S, Weis P, Driesner T, Bouvier A-S, Baumgartner L, Heinrich CA (2016) Contrasting hydrological processes of meteoric water incursion during magmatic–hydrothermal ore deposition: an oxygen isotope study by ion microprobe. Earth Planet Sci Lett 451:263-271.

Fitton JG (1995) Coupled molybdenum and niobium depletion in continental basalts. Earth Planet Sci Lett 136:715-721.

Fontboté L (2018) Ore deposits of the Central Andes. Elements 14:257-261.

Fournier RO (1999) Hydrothermal processes related to movement of fluid from plastic into brittle rock in the magmatic-epithermal environment. Econ Geol 94:1193-1211.

Gautheron C, Moreira M (2002) Helium signature of the subcontinental lithospheric mantle. Earth Planet Sci Lett 199:39-47.

Geissman JW, Snee LW, Graaskamp GW, Carten RB, Geraghty EP (1992) Deformation and age of the Red Mountain intrusive system (Urad-Henderson molybdenum deposits), Colorado: Evidence from paleomagnetic and [40]Ar/[39]Ar data. Geol Soc Am Bull 104:1031-1047.

Giggenbach WF (1992) Isotopic shifts in waters from geothermal and volcanic systems along convergent plate boundaries and their origin. Earth Planet Sci Lett 113:495-510.

Giggenbach WF (1997) The origin and evolution of fluid in magmatic-hydrothermal systems In: Barnes HL (ed) Geochemistry of hydrothermal ore deposits. 3 edn. John Wiley & Sons, New York, pp 737-796.

Glodny J, Ring U (2022) The Cycladic Blueschist Unit of the Hellenic subduction orogen: Protracted high-pressure metamorphism, decompression and reimbrication of a diachronous nappe stack. Earth Sci Rev 224:103883.

Glodny J, Bingen B, Austrheim H, Molina JF, Rusin A (2002) Precise eclogitization ages deduced from Rb/Sr mineral systematics: the Maksyutov complex, Southern Urals, Russia. Geochimica et Cosmochimica Acta 66:1221-1235.

Goldstein HR, Reynolds TJ (1994) Systematics of fluid inclusions in diagenetic minerals. SEPM Short Course 31:1-199.

Gostyayeva N, Theodore TG, Lowenstern JB (1996) Implications of fluid-inclusion relations in the Elder Creek porphyry copper system, Battle Mountain mining district, Nevada. US Geol Surv Open-File Report 96-268:1-61.

Graham DW (2002) Noble gas isotope geochemistry of mid-ocean ridge and ocean island basalts: Characterization of mantle source reservoirs. Rev Mineral Geochem 47:247-317.

Granet M, Chabaux F, Stille P, France-Lanord C, Pelt E (2007) Time-scales of sedimentary transfer and weathering processes from U-series nuclides: clues from the Himalayan rivers. Earth Planet Sci Lett 261:389-406.

Grant JN, Halls C, Avila Salinas W, Snelling NJ (1979) K-Ar ages of igneous rocks and mineralization in part of the Bolivian tin belt. Econ Geol 74:838-851.

Greaney AT, Rudnick RL, Gaschnig RM, Whalen JB, Luais B, Clemens JD (2018) Geochemistry of molybdenum in the continental crust. Geochimica et Cosmochimica Acta 238:36-54.

Hall WE, Friedman I, Nash JT (1974) Fluid inclusion and light stable isotope study of the Climax molybdenum deposits, Colorado. Econ Geol 69:884-901.

Hayba DO, Ingebritsen SE (1997) Multiphase groundwater flow near cooling plutons. Journal of Geophysical Research: Solid Earth 102:12235-12252.

Hedenquist JW (1995) The ascent of magmatic fluid: discharge versus mineralization. Mineralogical Association of Canada Short Course Series: 23:263-289.

Hedenquist JW, Lowenstern JB (1994) The role of magmas in the formation of hydrothermal ore deposits. Nature 370:519-527.

Hedenquist JW, Arribas A, Reynolds TJ (1998) Evolution of an intrusion-centered hydrothermal system; Far Southeast-Lepanto porphyry and epithermal Cu-Au deposits, Philippines. Econ Geol 93:373-404.

Heinrich CA (2005) The physical and chemical evolution of low-salinity magmatic fluids at the porphyry to epithermal transition: a thermodynamic study. Miner Deposita 39:864-889.

Heinrich CA, Ryan CG, Mernagh TP, Eadington PJ (1992) Segregation of ore metals between magmatic brine and vapor; a fluid inclusion study using PIXE microanalysis. Econ Geol 87:1566-1583.

Heinrich CA, Driesner T, Stefánsson A, Seward TM (2004) Magmatic vapor contraction and the transport of gold from the porphyry environment to epithermal ore deposits. Geology 32:761-764.

Hemley JJ, Hunt JP (1992) Hydrothermal ore-forming processes in the light of studies in rock-buffered systems; II, Some general geologic applications. Econ Geol 87:23-43.

Hemley JJ, Meyer C, Hodgson CJ, Thatcher AB (1967) Sulfide solubilities in alteration-controlled systems. Science 158:1580-1582.

Henley RW, McNabb A (1978) Magmatic vapor plumes and ground-water interaction in porphyry copper emplacement. Econ Geol 73:1-20.

Hoefs J (2018) Stable isotope geochemistry. Springer International Publishing AG.

Holland HD (2005) 100th anniversary special paper: sedimentary mineral deposits and the evolution of earth's near-surface environments. Econ Geol 100:1489-1509.

Honda M, McDougall I, Patterson DB, Doulgeris A, Clague DA (1991) Possible solar noble-gas component in Hawaiian basalts. Nature 349:149-151.

Honma H, Itihara Y (1981) Distribution of ammonium in minerals of metamorphic and granitic rocks. Geochim Cosmochim Acta 45:983-988.

Howard KA, Wooden JL, Barnes CG, Premo WR, Snoke AW, Lee S-Y (2011) Episodic growth of a Late Cretaceous and Paleogene intrusive complex of pegmatitic leucogranite, Ruby Mountains core complex, Nevada, USA. Geosphere 7:1220-1248.

Hui K, Qin K, Li Z, Wang F, Gao S, Han R, Kan J, Zhao J, Li G (2021) The linkage between the Jiawula-Chaganbulagen Ag-Pb-Zn and adjacent porphyry Mo-Cu mineralization, Inner Mongolia, Northeast China. Ore Geol Rev 134:104-153.

Hünemohr H (1989) Edelgase in U-und Th-reichen Mineralen und die Bestimmung der ^{21}Ne-Dicktarget-Ausbeute der ^{18}O (α, n) ^{21}Ne-Kernreaktion im Bereich 4.0-8.8 MeV. PhD thesis, Johannes-Gutenberg Universität Mainz.

Idiz EF, Carlisle D, Kaplan IR (1986) Interaction between organic matter and trace metals in a uranium rich bog, Kern County, California, USA. Appl Geochem 1:573-590.

Ingebritsen S, Geiger S, Hurwitz S, Driesner T (2010) Numerical simulation of magmatic hydrothermal systems. Rev Geophys 48.

Ingebritsen SE, Sanford WE, Neuzil CE (2006) Groundwater in geologic processes. Cambridge University Press.

Ishihara S, Shibata K, Uchiumi S (1989) K-Ar age of molybdenum mineralization in the east-central Kitakami Mountains, Northern Honshu, Japan: Comparison with the Re-Os age. Geochem J 23:85-89.

Jia Y, Kerrich R (1999) Nitrogen isotope systematics of mesothermal lode gold deposits: Metamorphic, granitic, meteoric water, or mantle origin? Geology 27:1051-1054.

Johansing RJ, Thompson T, Skinner B, Landis G (1990) Geology and origin of Sherman-Type deposits, Central Colorado. Discussion and reply. In: Carbonate-Hosted Sulfide Deposits of the Central Colorado Mineral Belt. Soc Econ Geol Monogr 7: 367-406.

Keith JD, Christiansen EH, Carten RB (1993) The genesis of giant porphyry molybdenum deposits In: Hodgson C, Mason R, Whiting B (eds) Giant Ore Deposits. Soc Econ Geol Spec Publ 2: 285-316

Kelley KD, Romberger SB, Beaty DW, Pontius JA, Snee LW, Stein HJ, Thompson TB (1998) Geochemical and geochronological constraints on the genesis of Au-Te deposits at Cripple Creek, Colorado. Econ Geol 93:981-1012.

Kendrick MA, Burgess R, Pattrick RAD, Turner G (2001) Fluid inclusion noble gas and halogen evidence on the origin of Cu-porphyry mineralising fluids. Geochim Cosmochim Acta 65:2651-2668.

Kesler SE (1994) Mineral Resources, Economics and the Environment. McMillan, New York.

Klemm LM, Pettke T, Heinrich CA (2008) Fluid and source magma evolution of the Questa porphyry Mo deposit, New Mexico, USA. Miner Deposita 43:533.

Klemm LM, Pettke T, Heinrich CA, Campos E (2007) Hydrothermal evolution of the El Teniente deposit, Chile: Porphyry Cu-Mo ore deposition from low-salinity magmatic fluids. Econ Geol 102:1021-1045.

Korges M, Weis P, Andersen C (2020) The role of incremental magma chamber growth on ore formation in porphyry copper systems. Earth Planet Sci Lett 552:116584.

Kouzmanov K, Pokrovski GS (2012) Hydrothermal controls on metal distribution in porphyry Cu (-Mo-Au) systems In: Hedenquist JW, Harris M, Camus F (eds) Geology and genesis of major copper deposits and districts of the world: A tribute to Richard H Sillitoe. Soc Econ Geol Spec Publ, pp 573-618.

Kullerud L (1991) On the calculation of isochrons. Chem Geol 87:115-124.

Lageson DR, Schmitt JG, Horton BK, Kalakay TJ, Burton BR (2001) Influence of Late Cretaceous magmatism on the Sevier orogenic wedge, western Montana. Geology 29:723-726.

Lamy-Chappuis B, Heinrich CA, Driesner T, Weis P (2020) Mechanisms and patterns of magmatic fluid transport in cooling hydrous intrusions. Earth Planet Sci Lett 535:116111.

Landtwing MR, Furrer C, Redmond PB, Pettke T, Guillong M, Heinrich CA (2010) The Bingham Canyon porphyry Cu-Mo-Au deposit. III. Zoned copper-gold ore deposition by magmatic vapor expansion. Econ Geol 105:91-118.

Landtwing MR, Pettke T, Halter WE, Heinrich CA, Redmond PB, Einaudi MT, Kunze K (2005) Copper deposition during quartz dissolution by cooling magmatic–hydrothermal fluids: the Bingham porphyry. Earth Planet Sci Lett 235:229-243.

Lang JR, Eastoe CJ (1988) Relationships between a porphyry Cu-Mo deposit, base and precious metal veins and Laramide intrusions, Mineral Park, Arizona. Econ Geol 83:551-567.

Lecumberri-Sanchez P, Steele-MacInnis M, Weis P, Driesner T, Bodnar RJ (2015) Salt precipitation in magmatic-hydrothermal systems associated with upper crustal plutons. Geology 43:1063-1066.

Lee C-TA (2005) Trace element evidence for hydrous metasomatism at the base of the North American lithosphere and possible association with Laramide low-angle subduction. J Geol 113:673-685.

Lee J-Y, Marti K, Severinghaus JP, Kawamura K, Yoo H-S, Lee JB, Kim JS (2006) A redetermination of the isotopic abundances of atmospheric Ar. Geochim Cosmochim Acta 70:4507-4512.

Lerchbaumer L, Audétat A (2012) High Cu concentrations in vapor-type fluid inclusions: An artifact? Geochim Cosmochim Acta 88:255-274.

Li Z-Z, Qin K-Z, Li G-M, Jin L-Y, Song G-X, Han R (2019) Incursion of meteoric water triggers molybdenite precipitation in porphyry Mo deposits: A case study of the Chalukou giant Mo deposit. Ore Geol Rev 109:144-162.

Lipman PW, Mehnert HH (1975) Late Cenozoic basaltic volcanism and development of the Rio Grande depression in the southern Rocky Mountains. Geol Soc Am Mem 144:119-154.

Livingston DE (1973) A plate tectonic hypothesis for the genesis of porphyry copper deposits of the southern Basin and Range province. Earth Planet Sci Lett 20:171-179.

London D (2008) Pegmatites. Can Mineral Spec Pub 10:347.

Lowenstern JB (1994) Dissolved volatile concentrations in an ore-forming magma. Geology 22:893-896.

Lowenstern JB (2001) Carbon dioxide in magmas and implications for hydrothermal systems. Miner Deposita 36:490-502.

Luck JM, Allègre CJ (1982) The study of molybdenites through the^{187}Re-^{187}Os chronometer. Earth Planet Sci Lett 61:291-296.

Lüders V (2017) Contribution of infrared microscopy to studies of fluid inclusions hosted in some opaque ore minerals: possibilities, limitations, and perspectives. Miner Deposita 52:663-673.

Lüders V, Ziemann M (1999) Possibilities and limits of infrared light microthermometry applied to studies of pyrite-hosted fluid inclusions. Chem Geol 154:169-178.

Lüders V, Plessen B (2015) Stable carbon isotope ratios of CH_4-rich gas inclusions in shale-hosted fracture-fill mineralization: A tool for tracing hydrocarbon generation and migration in shale plays for oil and gas. Marine Petrol Geol 63:68-81.

Lüders V, Plessen B, di Primio R (2012) Stable carbon isotopic ratios of CH_4–CO_2-bearing fluid inclusions in fracture-fill mineralization from the Lower Saxony Basin (Germany)–A tool for tracing gas sources and maturity. Marine Petrol Geol 30:174-183.

Lüders V, Romer RL, Gilg HA, Bodnar RJ, Pettke T, Misantoni D (2009) A geochemical study of the Sweet Home Mine, Colorado Mineral Belt, USA: hydrothermal fluid evolution above a hypothesized granite cupola. Miner Deposita 44:415-434.

Ludington S, Plumlee GS (2009) Climax-type porphyry molybdenum deposits. US Geol Surv Open-File Report 2009-1215:1-16.

Ludwig KR (2009) Isoplot/Ex 3.71 A geochronological toolkit for Microsoft Excel. Berkeley Geochronology Center, Spec Pub:76.

Lund K, McAleer RJ, Aleinikoff JN, Cosca MA, Kunk MJ (2018) Two-event lode-ore deposition at Butte, USA: ^{40}Ar/^{39}Ar and U-Pb documentation of Ag-Au-polymetallic lodes overprinted by younger stockwork Cu-Mo ores and penecontemporaneous Cu lodes. Ore Geology Reviews 102:666-700.

Lund K, Aleinikoff JN, Kunk MJ, Unruh DM, Zeihen GD, Hodges WC, du Bray EA, O'Neill JM (2002) SHRIMP U-Pb and ^{40}Ar/^{39}Ar age constraints for relating plutonism and mineralization in the Boulder Batholith region, Montana. Econ Geol 97:241-267.

Magee C, Stevenson CT, Ebmeier SK, Keir D, Hammond JO, Gottsmann JH, Whaler KA, Schofield N, Jackson CA, Petronis MS (2018) Magma plumbing systems: a geophysical perspective. J Petrol 59:1217-1251.

Malvicini L (1978) Las vetas de estaño y plata de mina Pirquitas (Pircas), prov. de Jujuy, Republica Argentina. Revista de la Asociación Argentina de Mineralogía, Petrología y Sedimentología, Rev 9:1-26.

Mao J, Zhang J, Pirajno F, Ishiyama D, Su H, Guo C, Chen Y (2011) Porphyry Cu–Au–Mo–epithermal Ag–Pb–Zn–distal hydrothermal Au deposits in the Dexing area, Jiangxi province, East China—a linked ore system. Ore Geol Rev 43:203-216.

Markey R, Stein HJ, Hannah JL, Zimmerman A, Selby D, Creaser RA (2007) Standardizing Re–Os geochronology: a new molybdenite reference material (Henderson, USA) and the stoichiometry of Os salts. Chem Geol 244:74-87.

Martin M, Dilles JH (2000) U-Pb zircon and sphene geochronologic constraints for the Butte porphyry system. Geol Soc Am Abstracts with Programs, v. 32, no. 6, p. A28.

Masterman GJ, Cooke DR, Berry RF, Walshe JL, Lee AW, Clark AH (2005) Fluid chemistry, structural setting, and emplacement history of the Rosario Cu-Mo porphyry and Cu-Ag-Au epithermal veins, Collahuasi district, northern Chile. Econ Geol 100:835-862.

McCalpin JP, Temple J, Sicard K, Mendel D, Ahmad B (2012) Climax Quadrangle Geologic map, Lake and Park Counties, Colorado. Colorado Geol Surv Open-File Report 12-09.

McFaul EJ, Mason GT, Ferguson WB, Lipin BR (2000) U.S. Geological Survey mineral databases; MRDS and MAS/MILS Data Series. Eastern Mineral and Environmental Resources Science Center.

McPhee J (1990) Basin and range. Noonday Press, New York.

Mercer CN, Hofstra AH, Todorov TI, Roberge J, Burgisser A, Adams DT, Cosca M (2015) Pre-eruptive conditions of the Hideaway Park topaz rhyolite: insights into metal source and

evolution of magma parental to the Henderson porphyry molybdenum deposit, Colorado. J Petrol 56:645-679.

Mingram B, Bräuer K (2001) Ammonium concentration and nitrogen isotope composition in metasedimentary rocks from different tectonometamorphic units of the European Variscan Belt. Geoch Cosmochim Acta 65:273-287.

Misantoni D, Silberman ML, Lees BK (1998) Geology of the Sweet Home mine and Alma district. Mineral Rec 29:4:101-114.

Mlynarczyk MSJ, Williams-Jones AE (2005) The role of collisional tectonics in the metallogeny of the Central Andean tin belt. Earth Planet Sci Lett 240:656-667.

Monecke T, Monecke J, Reynolds TJ, Tsuruoka S, Bennett MM, Skewes WB, Palin RM (2018) Quartz solubility in the H2O-NaCl system: A framework for understanding vein formation in porphyry copper deposits. Econ Geol 113:1007-1046.

Mutschler FE, Larson EE, Bruce RM (1987) Laramide and younger magmatism in Colorado—New petrologic and tectonic variations on old In: Drexler JW, Larson EE (eds) Cenozoic volcanism in the southern Rocky Mountains updated: A tribute to Rudy C Epis—Part I. Colorado School of Mines Quarterly.

Mutschler FE, Wright EG, Ludington S, Abbott JT (1981) Granite molybdenite systems. Econ Geol 76:874-897.

Myrow PM, Taylor JF, Miller JF, Ethington RL, Ripperdan RL, Allen J (2003) Fallen arches: Dispelling myths concerning Cambrian and Ordovician paleogeography of the Rocky Mountain region. Geol Soc Am Bull 115:695-713.

Nash JT, Theodore TG (1971) Ore fluids in the porphyry copper deposit at Copper Canyon, Nevada. Econ Geol 66:385-399.

Niedermann S, Bach W, Erzinger J (1997) Noble gas evidence for a lower mantle component in MORBs from the southern East Pacific Rise: Decoupling of helium and neon isotope systematics. Geochim Cosmochim Acta 61:2697-2715.

Ohmoto H, Rye RO (1979) Isotopes of sulfur and carbon In: Barnes H (ed) Geochemistry of Hydrothermal Ore Deposits, 3rd edn. Wiley, New York, pp 509-567.

Ohmoto H, Lasaga AC (1982) Kinetics of reactions between aqueous sulfates and sulfides in hydrothermal systems. Geochim Cosmochim Acta 46:1727-1745.

Ozima M, Igarashi G (2000) The primordial noble gases in the Earth: a key constraint on Earth evolution models. Earth Planet Sci Lett 176:219-232.

Ozima M, Podosek FA (2002) Noble Gas Geochemistry. Cambridge University Press.

Paar WH, Miletich R, Topa D, Criddle AJ, De Brodtkorb MK, Amthauer G, Tippelt G (2000) Suredaite, PbSnS3, a new mineral species, from the Pirquitas Ag-Sn deposit, NW-Argentina: mineralogy and crystal structure. Am Min 85:1066-1075.

Papale P, Polacci M (1999) Role of carbon dioxide in the dynamics of magma ascent in explosive eruptions. Bull Volcanology 60:583-594.

Passamani FM, Bongiolo EM, de Oliveira FN, Neumann R (2020) Geology and structural controls of the Ag–Sn–Zn Pirquitas deposit, northwestern Argentina. J S Am Earth Sci 100:15.

Peterman ZE, Hedge CE (1968) Chronology of Precambrian events in the Front Range, Colorado. Can J Earth Sci 5:749-756.

Pettke T, Oberli F, Heinrich CA (2010) The magma and metal source of giant porphyry-type ore deposits, based on lead isotope microanalysis of individual fluid inclusions. Earth Planet Sci Lett 296:267-277.

Plessen B, Lüders V (2012) Simultaneous measurements of gas isotopic compositions of fluid inclusion gases (N_2, CH_4, CO_2) using continuous-flow isotope ratio mass spectrometry. Rapid Commun Mass Spectrometry 26:1157-1161.

Plotinskaya OY, Grabezhev AI, Groznova EO, Seltmann R, Lehmann B (2014) The Late Paleozoic porphyry–epithermal spectrum of the Birgilda–Tomino ore cluster in the South Urals, Russia. J Asian Earth Sci 79:910-931.

Pöter B, Gottschalk M, Heinrich W (2004) Experimental determination of the ammonium partitioning among muscovite, K-feldspar, and aqueous chloride solutions. Lithos 74:67-90.

Proffett JM (2003) Geology of the Bajo de la Alumbrera porphyry copper-gold deposit, Argentina. Econ Geol 98:1535-1574.

Quadt von A, Erni M, Martinek K, Moll M, Peytcheva I, Heinrich CA (2011) Zircon crystallization and the lifetimes of ore-forming magmatic-hydrothermal systems. Geology 39:731-734.

Reisberg L, Meisel T (2002) The Re-Os isotopic system: A review of analytical techniques. Geostandard Newslett 26:249-267.

Reynolds TJ (1998) Ancient fluids at the Sweet Home mine. Mineralogical Record 29:4:127-134.

Richards JP (2003) Tectono-magmatic precursors for porphyry Cu-(Mo-Au) deposit formation. Econ Geol 98:1515-1533.

Rodríguez A, Weis P, Magnall JM, Gleeson SA (2021) Hydrodynamic constraints on ore formation by basin-scale fluid flow at continental margins: Modelling Zn metallogenesis in the Devonian Selwyn Basin. Geochem Geophys 22, e2020GC009453.

Roedder E (1984) Fluid Inclusions. Miner Soc Am Rev Mineral 12:1-644.

Romer RL, Lüders V (2006) Direct dating of hydrothermal W mineralization: U–Pb age for hübnerite ($MnWO_4$), Sweet Home Mine, Colorado. Geochim Cosmochim Acta 70:4725-4733.

Romer RL, Cuney M (2018) Phanerozoic uranium mineralization in Variscan Europe–more than 400 Ma of tectonic, supergene, and climate-controlled uranium redistribution. Ore Geol Rev 102:474-504.

Rowe A (2012) Ore Genesis and Fluid Evolution of the Goat Hill Orebody, Questa Climax-type Porphyry-Mo System, NM and Its Comparison to the Climax-type Deposits of the Colorado Mineral Belt. PhD thesis, New Mexico Inst Min Technol, Socorro, New Mexico.

Rowins SM (2000) Reduced porphyry copper-gold deposits: A new variation on an old theme. Geology 28:491-494.

Rudnick RL, Gao S (2003) Composition of the continental crust In: Rudnick RL (ed) Treatise on Geochemistry. Elsevier, Oxford, pp 1-64.

Rusk BG, Reed MH, Dilles JH (2008) Fluid inclusion evidence for magmatic-hydrothermal fluid evolution in the porphyry copper-molybdenum deposit at Butte, Montana. Econ Geol 103:307-334.

Russell LR, Snelson S (1994) Structure and tectonics of the Albuquerque basin segment of the Rio Grande rift: Insights from reflection seismic data. Geol Soc Am Spec Pap 291:83-112.

Rye RO, O'Neil JR (1968) The O18 content of water in primary fluid inclusions from Providencia, north-central Mexico. Econ Geol 63:232-238.

Santosh M, Suzuki K, Masuda A (1994) Re-Os dating of molybdenites from southern India: Implication for Pan-African metallogeny. J Geol Soc India 43:585-590.

Sarda P, Staudacher T, Allègre CJ (1988) Neon isotopes in submarine basalts. Earth Planet Sci Lett 91:73-88.

Scaillet B, Pichavant M (2005) A model of sulphur solubility for hydrous mafic melts: application to the determination of magmatic fluid compositions of Italian volcanoes. Annals Geophysics 48:671-698.

Schirra M, Laurent O, Zwyer T, Driesner T, Heinrich CA (2022) Fluid Evolution at the Batu Hijau Porphyry Cu-Au Deposit, Indonesia: Hypogene Sulfide Precipitation from a Single-Phase Aqueous Magmatic Fluid During Chlorite–White-Mica Alteration. Econ Geol 117:979-1012.

Schodde R (2017) Challenges of Exploring Under Deep Cover AMIRA International's 11th Biennial Exploration Managers Conference 28th–31st March.

Schöpa A, Annen C, Dilles JH, Sparks RSJ, Blundy JD (2017) Magma emplacement rates and porphyry copper deposits: Thermal modeling of the Yerington batholith, Nevada. Econ Geol 112:1653-1672.

Scott C, Lyons TW, Bekker A, Shen Y-a, Poulton SW, Chu X-l, Anbar AD (2008) Tracing the stepwise oxygenation of the Proterozoic ocean. Nature 452:456-459.

Seedorff E, Einaudi MT (2004a) Henderson porphyry molybdenum system, Colorado: I. Sequence and abundance of hydrothermal mineral assemblages, flow paths of evolving fluids, and evolutionary style. Econ Geol 99:3-37.

Seedorff E, Einaudi MT (2004b) Henderson porphyry molybdenum system, Colorado: II. Decoupling of introduction and deposition of metals during geochemical evolution of hydrothermal fluids. Econ Geol 99:39-72.

Seo JH, Heinrich CA (2013) Selective copper diffusion into quartz-hosted vapor inclusions: Evidence from other host minerals, driving forces, and consequences for Cu–Au ore formation. Geochimica et Cosmochimica Acta 113:60-69.

Seward TM, Barnes HL (1997) Metal transport by hydrothermal ore fluids In: Barnes HL (ed) Geochemistry of hydrothermal ore deposits. 3rd edn. Wiley, New York, pp 435-486.

Shannon JR, Bookstrom AA, Smith RP (1984) Contemporaneous bimodal mafic-felsic magmatism at Red Mountain. Clear Creek County Climax, Colorado: Geological Society of America Abstracts with Programs 16:254.

Shannon JR, Nelson EP, Golden RJ (2004) Surface and underground geology of the world-class Henderson molybdenum porphyry mine, Colorado In: Nelson E, Erslev E (eds) Field Trips in the Southern Rocky Mountains, USA. Geol Soc Am, Field Guide 5, pp 207-218.

Sheppard SMF (1986) Characterization and isotope variations in natural waters. Rev Mineral 16:165-183.

Sheppard SMF, Nielsen RL, Taylor HP (1971) Hydrogen and oxygen isotope ratios in minerals from porphyry copper deposits. Econ Geol 66:515-542.

Sillitoe RH (2010) Porphyry copper systems. Econ Geol 105:3-41.

Sillitoe RH, Hedenquist JW (2005) Linkages between volcanotectonic settings, ore-fluid compositions, and epithermal precious metal deposits. Econ Geol Spec Pub 10:315-343.

Sillitoe RH, Halls C, Grant J (1975) Porphyry tin deposits in Bolivia. Econ Geol 70:913-927.

Simmons EC, Hedge CE (1978) Minor-element and Sr-isotope geochemistry of Tertiary stocks, Colorado mineral belt. Contrib Mineral Petrol 67:379-396.

Simon AC, Pettke T, Candela PA, Piccoli PM, Heinrich CA (2006) Copper partitioning in a melt–vapor–brine–magnetite–pyrrhotite assemblage. Geochim Cosmochim Acta 70:5583-5600.

Simón V, Arnosio M, Trumbull RB, Caffe P, Rocholl A, Sudo M, Lucassen F, Huidobro F (2021) Geology, geochemistry and geochronology of Lindero porphyry gold deposit in the Southern Puna plateau, Argentina. J S Am Earth Sci 105:103047.

Sinclair WD (2007) Porphyry deposits In: Goodfellow WD (ed) Mineral deposits of Canada: A synthesis of major deposit-types, district metallogeny, the evolution of geological provinces, and exploration methods. Geological Association of Canada, Mineral Deposits Division, Spec Pub, pp 223-243.

Singer DA (1995) World class base and precious metal deposits; a quantitative analysis. Econ Geol 90:88-104.

Singer DA, Berger VI, Moring BC (2008) Porphyry copper deposits of the world: Database, Maps, Grade and Tonnage Models US Geological Survey open-file report 2008-1155.

Skinner BJ (1997) Hydrothermal metal deposits: What we do and don't know In: Barnes HL (ed) Geochemistry of Hydrothermal Ore Deposits. 3 edn. Wiley, New York, pp 1-29.

Slater ET, Kontak DJ, Mcdonald AM, Fayek M (2021) Origin of a multi-stage epithermal Ag-Zn-Pb-Sn deposit: the Miocene Cortaderas breccia body, Pirquitas mine, NW Argentina. Miner Deposita 56:381-406.

Smith RW (1983) Aqueous chemistry of molybdenum at elevated temperatures and pressures with applications to porphyry molybdenum deposits. PhD thesis, New Mexico Inst Min Technol, Socorro, New Mexico, 324 p.

Smith SP, Kennedy BM (1983) The solubility of noble gases in water and in NaCl brine. Geochim Cosmochim Acta 47:503-515.

Snee L, Miggins D, Geissman JW, Reed M, Dilles JH, Zhang L (1999) Thermal history of the Butte porphyry system, Montana. Geol Soc Am 31:A380.

Soler MM, Caffe PJ, Coira BL, Onoe AT, Kay SM (2007) Geology of the Vilama caldera: a new interpretation of a large-scale explosive event in the Central Andean plateau during the Upper Miocene. J Volcanol Geotherm Res 164:27-53.

Steele-MacInnis M (2018) Fluid inclusions in the system H_2O-NaCl-CO_2: An algorithm to determine composition, density and isochore. Chem Geol 498:31-44.

References

Steele-MacInnis M, Lecumberri-Sanchez P, Bodnar RJ (2012) Short note: HokieFlincs_H2O-NaCl: a Microsoft Excel spreadsheet for interpreting microthermometric data from fluid inclusions based on the PVTX properties of H_2O-NaCl. Computers & Geosciences 49:334-337.

Stein HJ (1988) Genetic traits of Climax-type granites and molybdenum mineralisation, Colorado Mineral Belt In: Taylor R, Strong D (eds) Recent Advances in the Geology of Granite-Related Mineral Deposits Can Inst Min Metal Spec Vol 39. pp 394-401.

Stein HJ, Hannah JL (1985) Movement and origin of ore fluids in Climax-type systems. Geology 13:469-474.

Stein HJ, Markey RJ, Morgan JW, Hannah JL, Scherstén A (2001) The remarkable Re–Os chronometer in molybdenite: how and why it works. Terra Nova 13:479-486.

Stein HJ, Markey RJ, Morgan JW, Hannah JL, Zak K, Sundblad K (1997) Re-Os dating of shear-hosted Au deposits using molybdenite In: Papunen H (ed) Mineral deposits: Research and exploration-where do we meet? A.A. Balkema, Rotterdam, pp 313-317.

Sterner SM, Bodnar RJ (1984) Synthetic fluid inclusions in natural quartz I. Compositional types synthesized and applications to experimental geochemistry. Geochim Cosmochim Acta 48:2659-2668.

Stewart JH (1980) Geology of Nevada. Nevada Bureau of Mines and Geology Spec Pub 4:136.

Stoltnow M, Weis P, Korges M (2023) Hydrological controls on base metal precipitation and zoning at the porphyry-epithermal transition constrained by numerical modeling. Sci Rep 13:3786.

Stoltnow M, Lüders V, De Graaf S, Niedermann S (2022) A geochemical study of the Sweet Home mine, Colorado Mineral Belt, USA: formation of deep hydrothermal vein–type molybdenum greisen and base metal mineralization. Mineralium Deposita 57:801-825.

Sugaki A, Kojima S, Shimada N (1988) Fluid inclusion studies of the polymetallic hydrothermal ore deposits in Bolivia. Miner Deposita 23:9-15.

Sun Y, Teng F-Z, Pang K-N, Ying J-F, Kuehner S (2021) Multistage mantle metasomatism deciphered by Mg–Sr–Nd–Pb isotopes in the Leucite Hills lamproites. Contrib Mineral Petrol 176:1-12.

Suzuki K, Masuda A (1993) The Re-Os age of molybdenite from the Hirase ore deposit, Japan, and its comparison with Rb-Sr and K-Ar ages for host rocks. Proc Jap Acad, Ser B 69:79-82.

Suzuki K, Shimizu H, Masuda A (1993) Reliable Re-Os age for molybdenite. Geochim Cosmochim Acta 57:1625-1628.

Suzuki K, Shimizu H, Masuda A (1996) ReOs dating of molybdenites from ore deposits in Japan: Implication for the closure temperature of the ReOs system for molybdenite and the cooling history of molybdenum ore deposits. Geochim Cosmochim Acta 60:3151-3159.

Taylor HP, Jr (1974) The application of oxygen and hydrogen isotope studies to problems of hydrothermal alteration and ore deposition. Econ Geol 69:843-883.

Theobald PK, Eppinger RG, Moss CK, Barton HN, Bielski AM, Kreidler TJ (1983) Mineral resource potential map of the Vasquez Peak Wilderness Study Area, and the St. Louis Peak and Williams Fork Roadless Areas, Clear Creek, Grand, and Summit counties, Colorado. US Geol Surv Miscellaneous Field Studies Map MF-1588-A.

Thompson TB, Arehart GB (1990) Geology and the origin of ore deposits in the Leadville district, Colorado: Part I. Geologic studies of orebodies and wall rocks In: Beaty DW, Landis GP, Thompson TB (eds) Carbonate-Hosted Sulfide Deposits of the Central Colorado Mineral Belt: . Econ Geol Monograph 7, pp 130-155.

Titley SR, Anthony EY (1989) Laramide mineral deposits in Arizona In: Jenney JP, Reynolds SJ (eds) Geologic Evolution of Arizona. Arizona Geol Soc Digest, pp 485-514.

Turneaure FS (1971) The Bolivian tin-silver province. Econ Geol 66:215-225.

Tweto O, Sims PK (1963) Precambrian ancestry of the Colorado mineral belt. Geol Soc Am Bull 74:991-1014.

Tweto OL (1960) Scheelite in the Precambrian gneisses of Colorado. Econ Geol 55:1406-1428.

Uemura R, Kina Y, Shen C-C, Omine K (2020) Experimental evaluation of oxygen isotopic exchange between inclusion water and host calcite in speleothems. Climate of the Past 16:17-27.

Ulrich T, Heinrich CA (2002) Geology and alteration geochemistry of the porphyry Cu-Au deposit at Bajo de la Alumbrera, Argentina. Econ Geol 97:1865-1888.

Villa IM, De Bièvre P, Holden N, Renne P (2015) IUPAC-IUGS recommendation on the half life of [87]Rb. Geochim Cosmochim Acta 164:382-385.

Völkening J, Walczyk T, Heumann KG (1991) Osmium isotope ratio determinations by negative thermal ionization mass spectrometry. Int J Mass Spectrom 105:147-159.

Voynick S (1998) The Sweet Home mine, 1873-1989. Mineral Rec 29:11-20.

Walczyk T, Hebeda EH, Heumann KG (1991) Osmium isotope ratio measurements by negative thermal ionization mass spectrometry (NTI-MS) Fresenius J Anal Chem 341:537-541.

Wallace PJ, Edmonds M (2011) The sulfur budget in magmas: evidence from melt inclusions, submarine glasses, and volcanic gas emissions. Rev Mineral Geochem 73:215-246.

Wallace S, Bookstrom A (1993) The Climax porphyry molybdenum system. Colorado School of Mines Quarterly 93:35-41.

Wallace SR (1995) The Climax-type molybdenite deposits: what they are, where they are and why they are. Econ Geol 90:1359-1380.

Wallace SR, MacKenzie WB, Blair RG, Muncaster NK (1978) Geology of the Urad and Henderson molybdenite deposits, Clear Creek County, Colorado, with a section on a comparison of these deposits with those at Climax, Colorado. Economic Geology 73:325-368.

Wallace SR, Muncaster NK, Jonson DC, MacKenzie WB, Bookstrom AA, Surface VE (1968) Multiple intrusion and mineralization at Climax, Colorado. Ore Deposits of the United States 1:605-640.

Wang L, Tang J, Cheng W, Chen W, Zhang Z, Lin X, Luo M, Yang C (2015) Origin of the ore-forming fluids and metals of the Bangpu porphyry Mo–Cu deposit of Tibet, China: constraints from He–Ar, H–O, S and Pb isotopes. J Asian Earth Sci 103:276-287.

Watanabe Y, Stein HJ (2000) Re-Os ages for the Erdenet and Tsagaan Suvarga porphyry Cu-Mo deposits, Mongolia, and tectonic implications. Econ Geol 95:1537-1542.

Weis P (2015) The dynamic interplay between saline fluid flow and rock permeability in magmatic–hydrothermal systems. Crustal permeability:373-392.

Weis P, Driesner T, Heinrich CA (2012) Porphyry-copper ore shells form at stable pressure-temperature fronts within dynamic fluid plumes. Science 338:1613-1616.

Weis P, Driesner T, Coumou D, Geiger S (2014) Hydrothermal, multiphase convection of H_2O-NaCl fluids from ambient to magmatic temperatures: A new numerical scheme and benchmarks for code comparison. Geofluids 14:347-371.

Wenrich KJ, Aumente-Modreski R (1998) Crystal chemistry of minerals from the Sweet Home mine. Mineralogical Record 29:132.

Westra G, Keith SB (1981) Classification and genesis of stockwork molybdenum deposits. Econ Geol 76:844-873.

White WH, Bookstrom AA, Kamilli RJ, Ganster MW, Smith RP, Ranta DE, Steininger RC (1981) Character and origin of Climax-type molybdenum deposits. Econ Geol 75:270-316.

Widmann BL, Bartos PJ, Madole RF, Barbá KE, Moll ME (2004) Geologic Map of the Alma Quadrangle, Park and Summit Counties, Colorado. Colorado Geol Surv Open-File Rep:04-03.

Williams-Jones AE, Heinrich CA (2005) 100th Anniversary special paper: vapor transport of metals and the formation of magmatic-hydrothermal ore deposits. Econ Geol 100:1287-1312.

Wood SA, Samson IM (1998) Solubility of ore minerals and complexation of ore metals in hydrothermal solutions In: Richards JP, Larson PB (eds) Techniques in hydrothermal ore deposits geology. Soc Econ Geol, Rev Econ Geol, pp 33-80.

Xiong X, Zhu L, Zhang G, Li N, Yuan H, Ding L, Sun C, Guo A (2018) Fluid inclusion geochemistry and magmatic oxygen fugacity of the Wenquan Triassic molybdenum deposit in the Western Qinling Orogen, China. Ore Geol Rev 99:244-263.

Yang Y-F, Chen Y-J, Pirajno F, Li N (2015) Evolution of ore fluids in the Donggou giant porphyry Mo system, East Qinling, China, a new type of porphyry Mo deposit: evidence from fluid inclusion and H–O isotope systematics. Ore Geol Rev 65:148-164.

Yao Q, Demicco RV (1997) Dolomitization of the Cambrian carbonate platform, southern Canadian Rocky Mountains; dolomite front geometry, fluid inclusion geochemistry, isotopic signature, and hydrogeologic modelling studies. Am J Sci 297:892-938.

Yapparova A, Gabellone T, Whitaker F, Kulik DA, Matthäi SK (2017a) Reactive transport modelling of dolomitisation using the new csmp++ gem coupled code: Governing equations, solution method and benchmarking results. Transp Porous Media 117:385-413.

Yapparova A, Gabellone T, Whitaker F, Kulik DA, Matthäi SK (2017b) Reactive transport modelling of hydrothermal dolomitisation using the CSMP++ GEM coupled code: Effects of temperature and geological heterogeneity. Chem Geol 466:562-574.

Yonkee WA, Dehler CD, Link PK, Balgord EA, Keeley JA, Hayes DS, Wells ML, Fanning CM, Johnston SM (2014) Tectono-stratigraphic framework of Neoproterozoic to Cambrian strata, west-central US: Protracted rifting, glaciation, and evolution of the North American Cordilleran margin. Earth Sci Rev 136:59-95.

Zahony S (1968) Chemical controls of molybdenum ore formation. Unpubl report, Climax Molybdenum Co, 20 p.

Zeng Q, Guo W, He H, Zhou L, Cheng G, Su F, Wang Y, Wang R (2018) He, Ar, and S isotopic compositions and origin of giant porphyry Mo deposits in the Lesser Xing'an Range–Zhangguangcai Range metallogenic belt, northeast China. J Asian Earth Sci 165:228-240.

Zhang F-F, Wang Y-H, Liu J-J (2016) Fluid inclusions and H–O–S–Pb isotope systematics of the Baishan porphyry Mo deposit in Eastern Tianshan, China. Ore Geol Rev 78:409-423.

Zhou L-l, Zeng Q-d, Liu J-m, Friis H, Zhang Z-l, Duan X-x, Chu S-x (2015) Ore genesis and fluid evolution of the Daheishan giant porphyry molybdenum deposit, NE China. J Asian Earth Sci 97:486-505.

Zimmerer MJ, McIntosh WC (2012) The geochronology of volcanic and plutonic rocks at the Questa caldera: Constraints on the origin of caldera-related silicic magmas. Geol Soc Am Bull 124:1394-1408.

Appendix

A Constraining the magmatic-hydrothermal fluid evolution from proximal to distal settings forming Sn-Ag-Pb-Zn deposits in NW Argentina

B Supplementary figures to chapters 2 and 3

C Supplementary tables to chapters 2, 3, and Appendix A

A Constraining the magmatic-hydrothermal fluid evolution from proximal to distal settings forming Sn-Ag-Pb-Zn deposits in NW Argentina

A report on the work progress before the COVID19 pandemic

A.1 Introduction

The original layout of this PhD thesis was part of the work package 4.2 of the DFG International Research Training Group StRATEGy, which aimed at addressing the magmatic-hydrothermal fluid evolution from proximal to distal settings forming epithermal (Sn-)Ag-Pb-Zn deposits in NW Argentina (Appendix Fig. 1). Within this framework, both geochemical and numerical modeling studies on the Pirquitas Sn-Ag (rather distal to in inferred intrusion) and Chinchillas Ag-Pb-Zn (rather proximal to an inferred intrusion) deposits had been planned and would have led to peer-reviewed publications in scientific journals. Fresh drill cores from depths >800 m from the Pirquitas and representative areas of the Chinchillas open pits would have been sampled for fluid inclusion microthermometric measurements and the acquisition of stable and radiogenic isotope data.
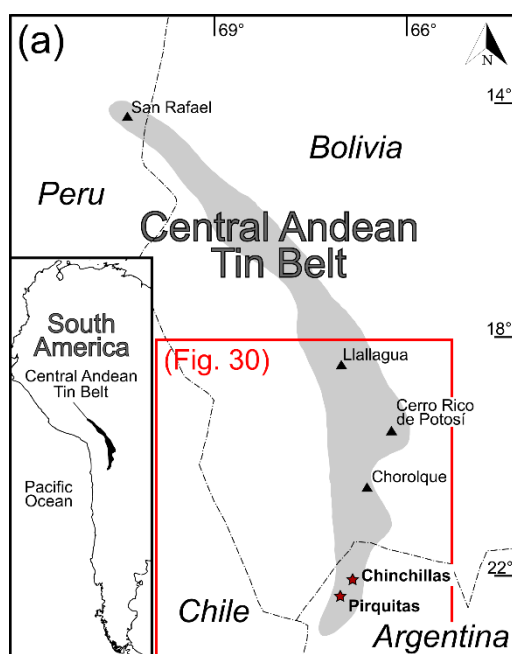
Appendix Figure 1 Map of the Central Andean Tin Belt, including major tin deposits as well as the Pirquitas and Chinchillas Deposits investigated in this chapter (modified after Mlynarczyk and Williams-Jones (2005)). The red box marks the southern sector of the tin belt presented with further details in Fig. 30.

The field campaign was planned to consist of two visits in summer 2019 and 2020. Unfortunately, the second visit was canceled a few days before departure because of the COVID19 pandemic. Access to the mine did not become possible during the first relaxation periods of the pandemic and the limited operations at the mine did not allow that samples selected during the first field visit could be shipped to

Germany. The second field visit was indispensable, because the first visit suffered from unforeseen logistical complications: (i) new drillings at Pirquitas had been postponed and would only have been available for sampling during the second visit; (ii) additional medical checks had to be performed in Argentina before the mines could be entered, which severely shortened the time at the mine sites; (ii) shortage in staff at the (then closed) Pirquitas mine prohibited sampling of old cores in the sheds; (iii) the obtained sample material from the Chinchillas open pit mine turned out to be insufficient for a comprehensive study with the planned geochemical techniques; and (iv) potentially promising samples of the drill cores from the Chinchillas mine were marked on-site, but could not be cut and shipped during the first visit, because the rock saw at the mine was not functioning.

Nonetheless, the visit to the Chinchillas project allowed for a site inspection of the open pit (Appendix Fig. 2a), including the sampling of hand specimens (Appendix Fig. 2b), and an examination of some hundred meters of drill core (Appendix Figs. 2c, d, e), where the most interesting sections have been marked.

In consequence, the original work plan on the Pirquitas and Chinchillas deposits had to be stopped during this PhD project. However, the work could potentially be continued in a follow-up project. Preliminary simulations on the formation of the Pirquitas deposit already produced interesting results and are summarized in Chapter 5.

A.2 The Chinchillas Ag-Pb-Zn deposit

In a setting of porphyry to epithermal transition, the Chinchillas Ag-Pb-Zn deposit is rather proximally located to the intrusion. A Miocene phreatomagmatic explosion produced a dacite diatreme with a cylindrically shaped caldera filled with subhorizontal tuff layers and surrounded by metapelitic Ordovician basement rocks (Caffe and Coira 2008; Caffe 2013). The collected hand specimen from Chinchillas partially consist of very fine-grained high-grade Ag ore hosted by porous tuff and partially of monomineralic sphalerite and galena veinlets and hydrothermal breccias hosted by metapelitic rocks. The tuff is mainly mineralized by very fine-grained disseminated Ag minerals (Ag sulfosalts, freibergite, boulangerite) and minor sphalerite and galena. Current conceptual models for ore genesis assume that ascending magmatic-hydrothermal fluids along the contact between the central tuff zone and surrounding basement caused brecciation of the basement with subsequent precipitation of sphalerite and galena alongside later calcite and siderite (Appendix Figs. 2b).
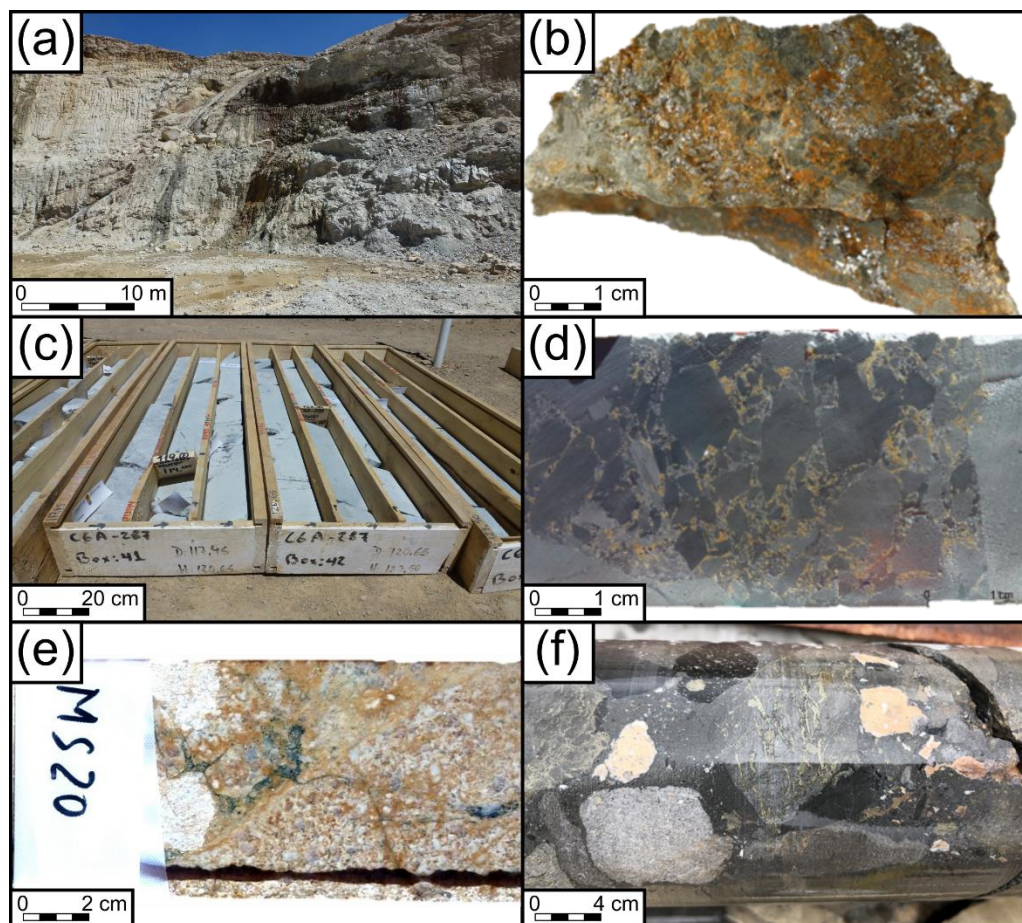
Appendix Figure 2 (a) Mineralized clasts in hydrothermal breccia from deep drillings at the Pirquitas mine (photo taken by SSR Mining Inc.). (b) Chinchillas open pit with the tuff at the bottom and the Ordovician metapelites in the stope (phase 1, level 4095). (c) Drill core sample of the galena and sphalerite breccia ore hosted by metapelite (Chinchillas Mine, sample MS03) (Appendix Table 8). (d) Drill core boxes with galena and sphalerite breccia ore hosted by metapelite (Chinchillas Mine). (e) Drill core sample of mineralized tuff (Chinchillas Mine, sample MS20) (Appendix Table 8). (f) Hand specimen of sphalerite and galena in a gangue of siderite hosted by metapelite from the Chinchillas open pit (phase 1, level 4095).

Geochemical data on the Chinchillas deposit, which is still under development for production, are sparse. With the sampling of hand specimen from the open pit and drill cores, subsequent fluid inclusion microthermometric and LA-ICPMS measurements, Raman spectroscopy, stable and noble gas isotope analyses as well as mineral stable and radiogenic isotope analyses can be applied. We aimed to reconstruct the evolution and P-T-x properties of the ore-forming fluids with the contribution of magmatic fluids and meteoric water and the extent of fluid-rock interaction prior to ore precipitation.

A.3 Proposed methods and materials

We planned the sampling of fresh deep drill cores from the Pirquitas Mine (Appendix Fig. 2f) as well as drill cores (Appendix Figs. 2c, d, e) and hand specimen (Appendix Fig. 2b) from the Chinchillas Mine. We further planned to conduct fluid inclusion microthermometric and LA-ICPMS measurements as well as Raman spectroscopy on both Pirquitas and Chinchillas samples. Furthermore, we planned to perform fluid inclusion stable and noble gas isotope analyses as well as mineral stable and radiogenic isotope analyses. Numerical simulations were planned to support the geochemical data.

Hand specimen from the open pit consist of veinlets and hydrothermal breccias mineralized with galena and sphalerite, sometimes in a gangue of calcite and siderite, hosted by the metapelitic basement rock (Appendix Fig. 2b). Drill cores from Chinchillas comprised porous tuff, which is either barren or mineralized by very fine-grained disseminated high-grade Ag ore (Appendix Fig. 2e), and basement rocks from different parts of the deposit (Appendix Figs. 2c, d). We marked 46 drill core sections, which we considered for geochemical analyses (Appendix Table 8, Appendix Fig. 2e).

A.4 Outlook

At the moment, neither the acquired geochemical data from Chinchillas, nor numerical simulations on Pirquitas are sufficient for individual full-length peer-reviewed publication. However, geochemical analysis on further sample material from mineralized hydrothermal breccias at Pirquitas may gain new insights in the formation of the Pirquitas deposit and can be combined with the numerical modeling results in an individual scientific publication. Similarly, the shipment of marked drill core samples from Chinchillas may result in good geochemical data and thus probably in another scientific publication.

New sample material from both the Pirquitas and Chinchillas deposits could be investigated for:

(i)   Fluid inclusion studies on ore and gangue minerals, including microthermometry to gather formation temperature and salinity of the ore fluid; Raman spectroscopy and Laser ICP-MS measurements to gain insides on the ore fluid composition and evolution; as well as stable and noble gas isotope analyses to check on fluid origins;

(ii)   Mineral radiogenic and stable isotope compositions (Sr, Pb, Ag, H, O, S) to find evidences on the origin of metals and sulfur;

(iii)   Numerical modeling to test the impact of certain parameters, including country rock permeabilities, varying the brittle-ductile transition, volume of the magma chamber, on the travel distance of hot ore fluids; the combined release of magmatic fluids from of a proximal and distal magma chamber in the same simulation and the activation of 1D line elements with variable widths and thus the possibility to either reflect faults or breccias, to form Pirquitas-like mineralization.

B Supplementary figures to chapters 2 and 3
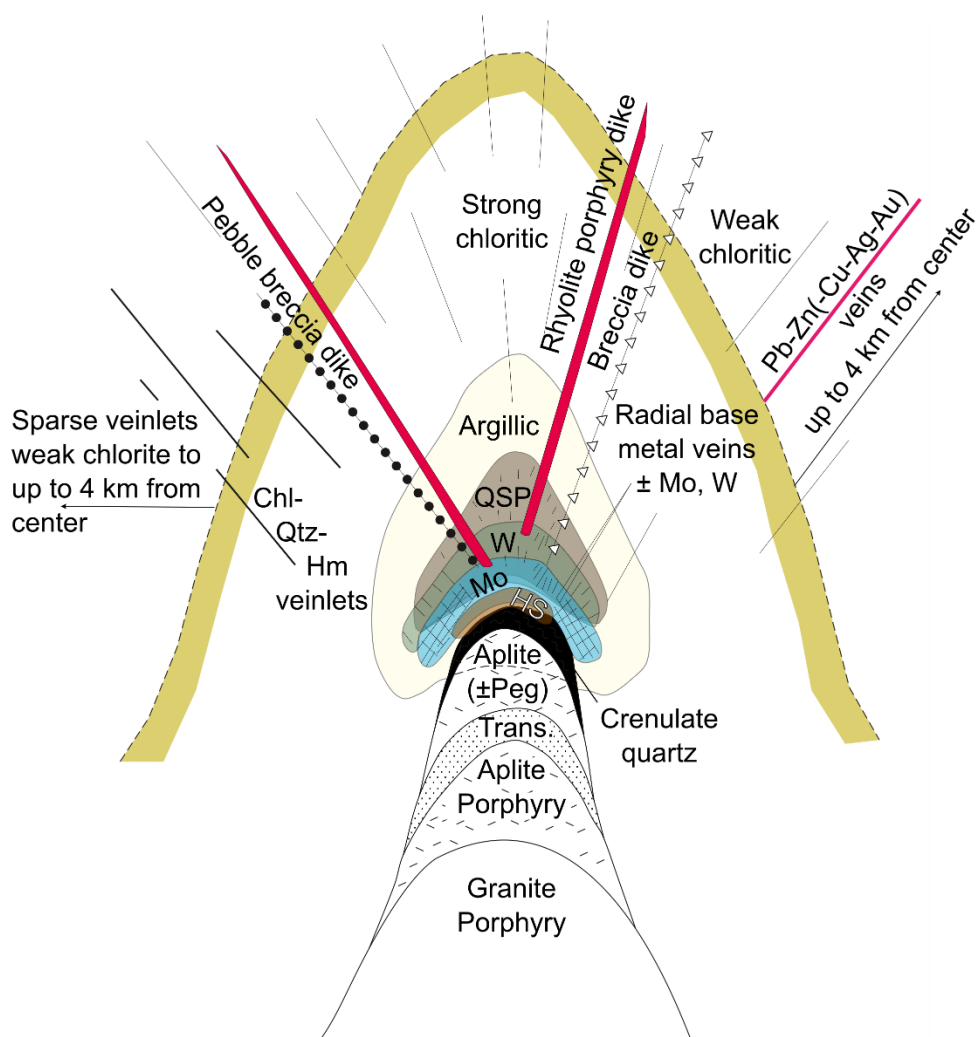
Appendix Figure 3 Idealized geologic section showing the formation of a Climax-type Mo deposit from a granite porphyry intrusion, which grades upwards to aplite porphyry and crenulate quartz layers. The cupola region is overlain and surrounded by the typical zones of the high-silica alteration (HS), molybdenite-quartz stockwork vein-bearing potassic alteration (Mo), greisen huebnerite-bearing (W), pervasive quartz-sericite-pyrite (QSP), and argillic alteration zones. Strong and weak chloritic alteration, as well as radial dikes of rhyolite porphyry, pebble, and angular breccias, may extend for several kilometers. Peripheral veins radiate from the porphyry center into adjacent country rocks and contain base metals (±molybdenite±huebnerite) in a gangue of quartz, fluorite, rhodochrosite, and calcite (± minor barite). Modified after Bookstrom (1989).
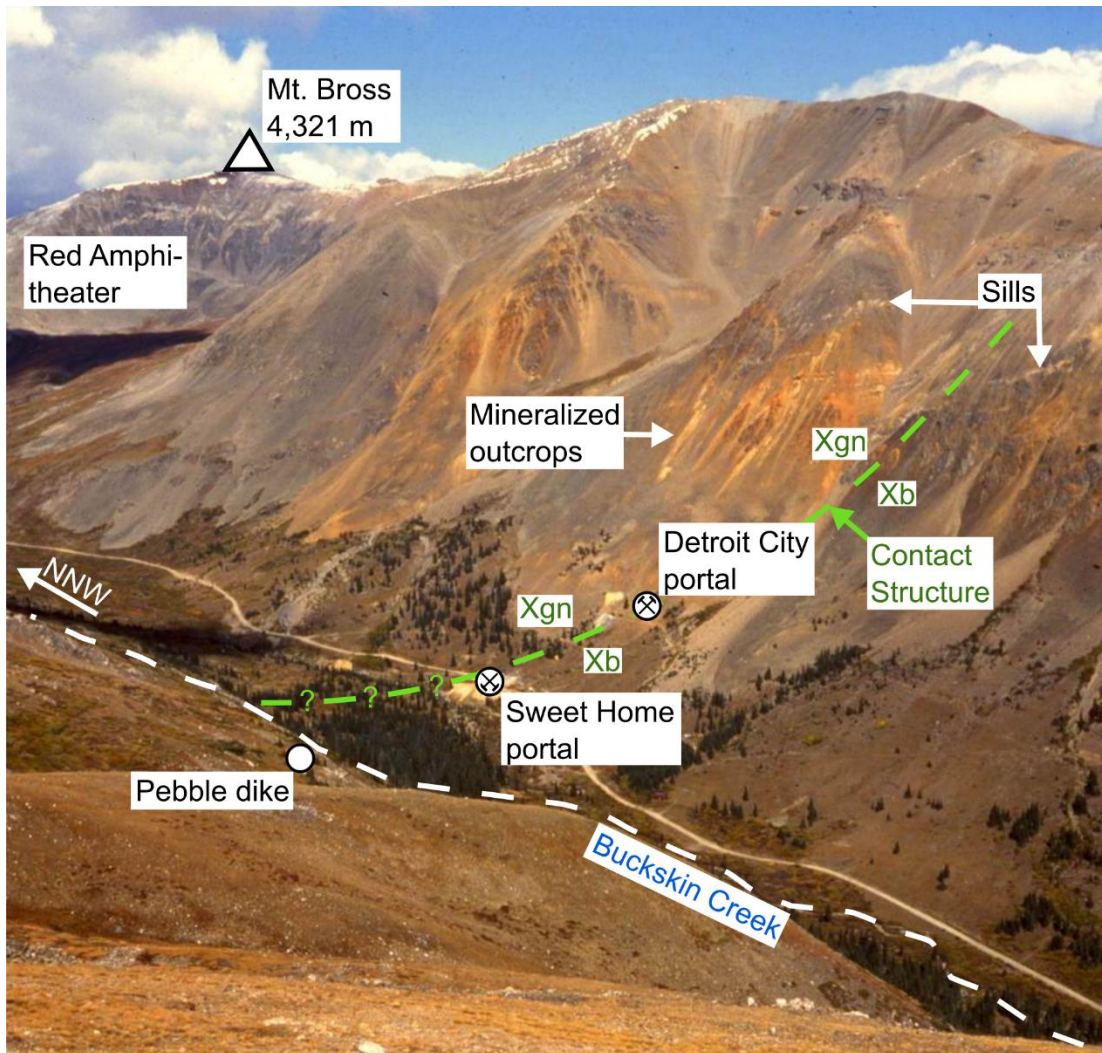
Appendix Figure 4 View showing the Buckskin Gulch along the Buckskin Creek (white dashed line) with the Red Amphitheater and Mt. Bross in the background. The Detroit City (crossed pick-axes right side up = active portal) and former Sweet Home portals (crossed pick-axes upside down = inactive portal) are located on the east side of the creek, with the pebble dike on the west side. Above the Detroit City portal, there are altered and mineralized outcrops and dioritic to quartz-monzonitic sills. The Contact Structure (green dashed line) separates the lithologies of biotite-rich gneisses and schists (Xb) and granitic rocks (Xgn, e.g. granite gneiss, pegmatite, migmatite). Photo by C. Walden, 1992, mapping by D. Misantoni.
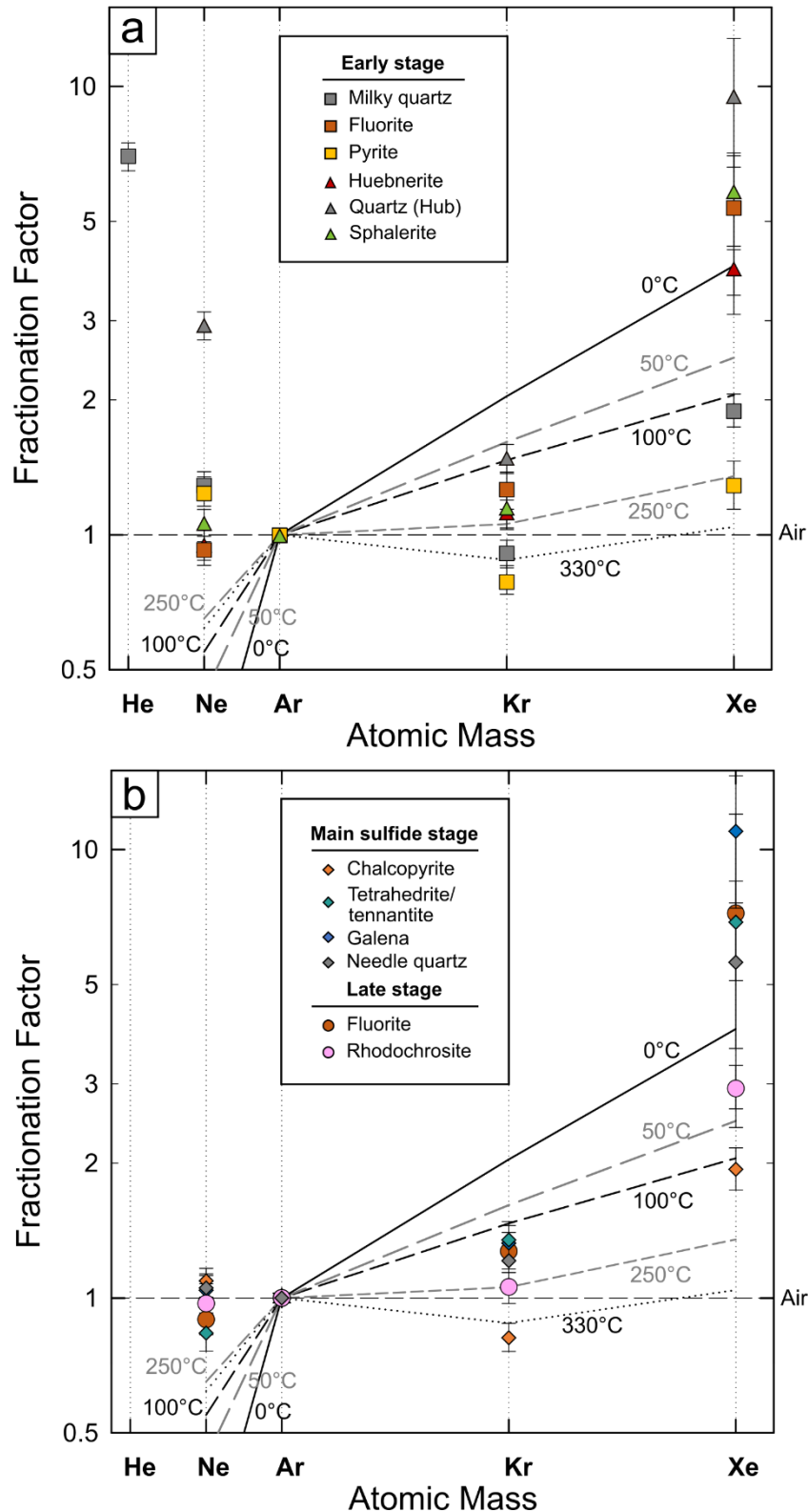
Appendix Figure 5 Logarithmic plots of noble gas abundances in Detroit City portal ore and gangue minerals as (a): early stage (ES) and (b): main sulfide (MSS) and late stage (LS) expressed as fractionation factors (ratios) relative to ^{36}Ar and air $(^iX/^{36}Ar)sample/(^iX/^{36}Ar)_{air}$, where ^iX is a noble gas. The labeled curves show dissolution equilibrium of noble gases in water for 0°C and 50°C at 5 wt.% salinity according to Smith and Kennedy (1983) and for 100°C, 250°C, and 330°C at zero salinity according to Crovetto et al. (1982). Early-stage quartz that is intergrown with huebnerite is displayed as "Quartz (Hub)".
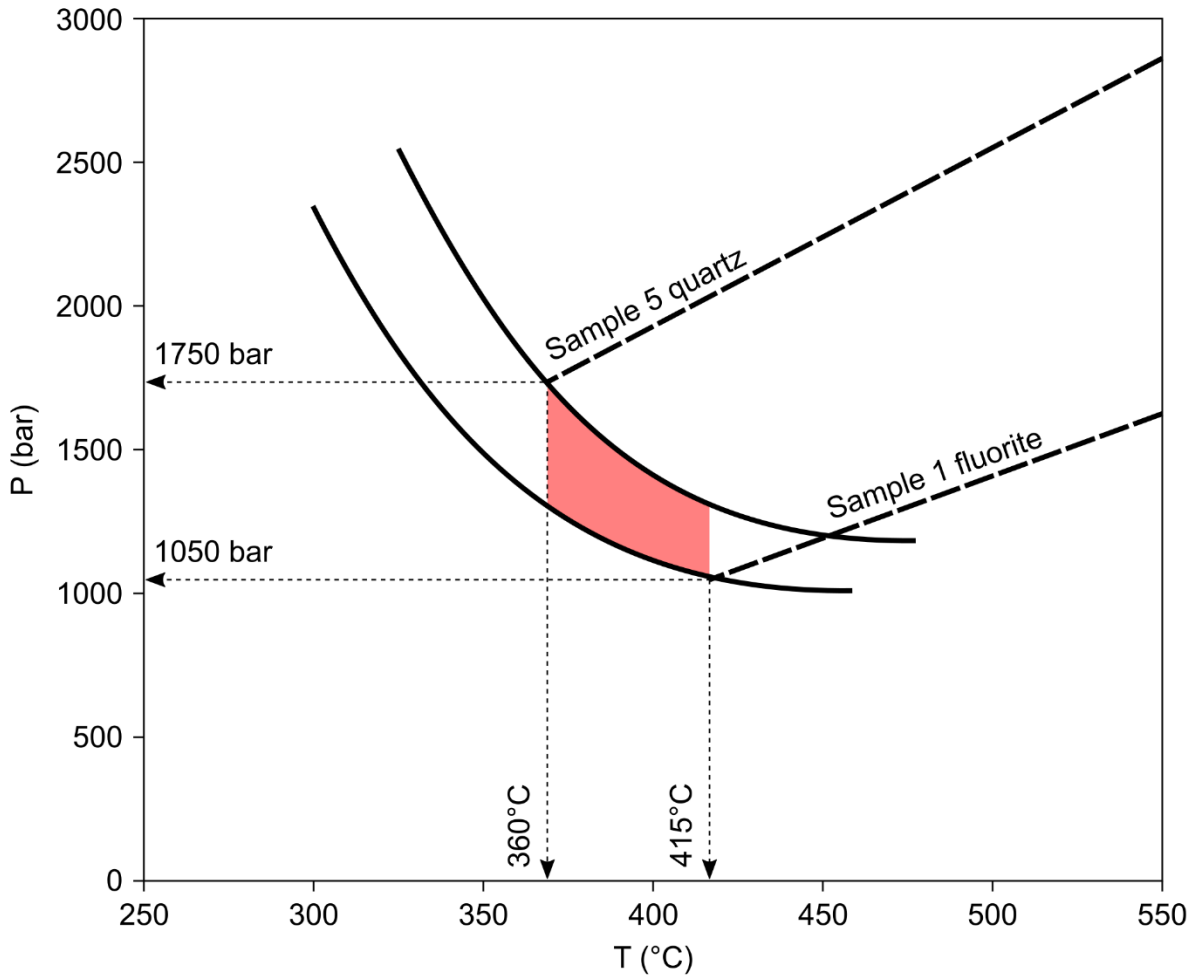
Appendix Figure 6 P-T diagram showing the solvi of the H2O-NaCl-CO2 system and selected isochores for type 1 FIs in quartz and fluorite. Solvi and isochores are calculated using the computer program by Steele-MacInnis (2018) for the H2O-NaCl-CO2 system. The red field indicates the P-T conditions of entrapment of the majority of type 1 FIs in fluorite and quartz.
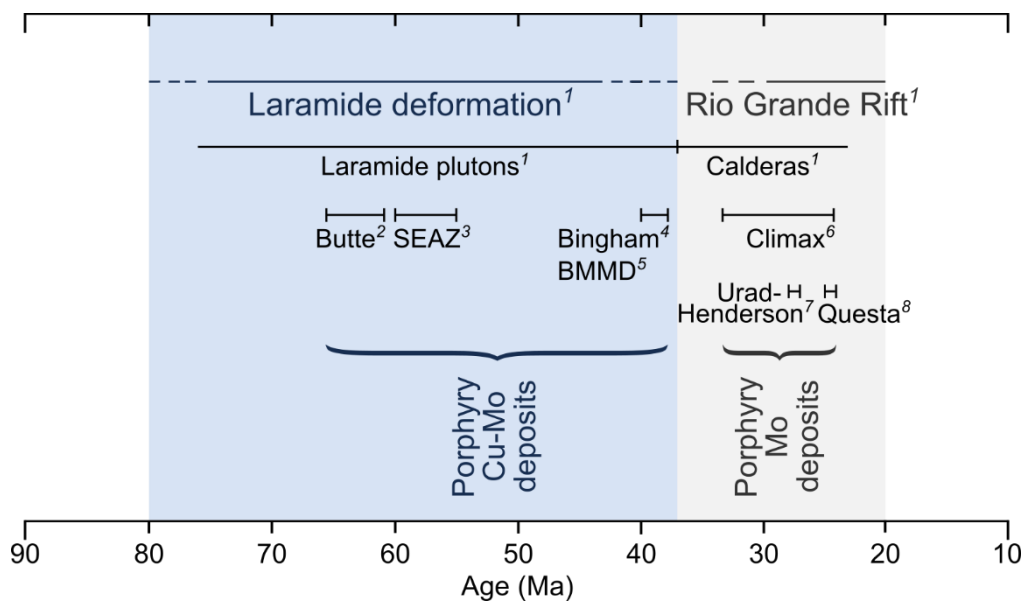
Appendix Figure 7 Time scale for tectonic and magmatic events, and major porphyry-related ore deposits. *SEAZ* South-East Arizona district, *BMMD* Battle Mountain Mining District. *1*

Chapin (2012 and references therein); *2* Snee et al. (1999); Martin and Dilles (2000); Lund et al. (2002); Lund et al. (2018); *3* Livingston (1973); Creasey (1980); Titley and Anthony (1989); *4* Deino and Keith (1998); Quadt von et al. (2011); *5* Gostyayeva et al. (1996); Rowins (2000); *6* White et al. (1981); Bookstrom et al. (1987); *7* Shannon et al. (2004); Markey et al. (2007); *8* Zimmerer and McIntosh (2012).
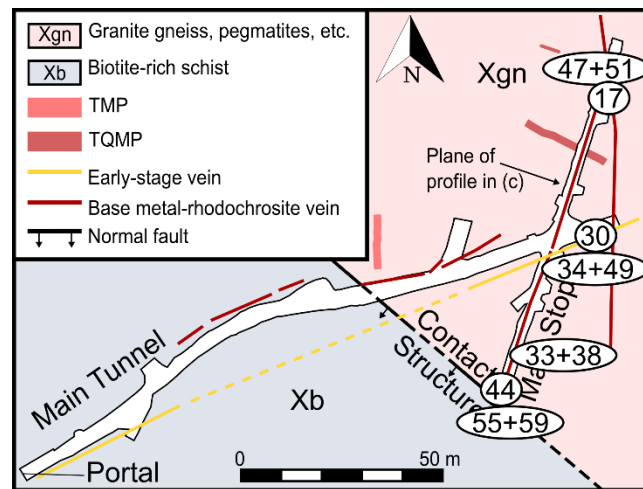
Appendix Figure 8 Simplified geological map (plane view) of the adit level (3515 m.a.s.l.) of the Detroit City Portal. Numbers in white circles refer to locations of samples with DC-prefix, TMP Monzonite porphyry, TQMP Quartz-monzonite porphyry, DCP Detroit City Portal, SHP Sweet Home Portal (see text), modified from Stoltnow et al. (2022).

C Supplementary tables to chapters 2, 3, and Appendix A

The tables can be found on the attached CD and include:

- Appendix Table 1 Methods conducted on the Sweet Home samples (Chapter 2)
- Appendix Table 2 Microthermometric and Laser Raman data of fluid inclusions hosted in early-stage ore and gangue minerals from the DCM, Colorado (Chapter 2)
- Appendix Table 3 Isotope data of fluid inclusions ($\delta^{18}O_w$ and δ^2H_w in ‰ vs. VSMOW) in minerals from the early, main sulfide and late stage, $\delta^{18}O_c$ (in ‰ vs. VSMOW) and $\delta^{13}C_c$ (in ‰ vs. VPDB) isotope ratios of rhodochrosite samples and CO_2 carbon isotope ratio of fluid inclusions in minerals from the early stage (in ‰ vs. VPDB) (Chapter 2)
- Appendix Table 4 Results of noble gas analyses of crush-released fluids in ore and gangue minerals from the DCM, Colorado (Chapter 2)
- Appendix Table 5 Sulfur isotopic composition of sulfides from the early and main sulfide stage (Chapter 2)
- Appendix Table 6 EPMA data (Chapter 3)
- Appendix Table 7 Sample origin and description (Chapter 3)
- Appendix Table 8 Marked drill cores from Chinchillas (Appendix A)

Curriculum Vitae

Malte Stoltnow

Address:	GFZ German Research Centre for Geosciences
	Inorganic and Isotope Geochemistry
	Telegrafenberg
	Potsdam, D-14473
Tel:	+49 331 288-27553
Email:	mstolt@gfz-potsdam.de

Academic Education

11/2018 – today

Ph.D. in Geosciences
University of Potsdam
GFZ German Research Centre for Geosciences
- Specialization: Ore deposit geology, Geochemistry, Numerical Modeling
- Thesis title: Magmatic-Hydrothermal Processes along the Porphyry to Epithermal Transition
- Member of the GFZ doctoral student council

11/2015 – 10/2018

M. Sc. in Geosciences/Economic Geology
TU Bergakademie Freiberg
University of Potsdam
- Specialization: Ore deposit geology, Geochemistry, Resource Management, Economic geology
- Thesis title: "Petrographic, geochemical, and mineral microanalytical investigations of the sulfide-rich mineralization in skarns from the Schwarzenberg mining district, Germany"
- Member of the SEG Student Chapter Freiberg

10/2012 – 11/2015

B. Sc. in Geosciences
University of Potsdam
- Specialization: Mineralogy, Petrology, Geochemistry
- Thesis title: "Geochemistry and Sr, Nd and Pb isotopic composition of Late Variscan Li-mica granites of the Eibenstock Massif in the western Erzgebirge Mountains"

Practical experience

01/2023 – today   *Research Associate*
Federal Institute for Geosciences and Natural Resources (BGR)
- Africa-wide strategic and economic critical raw material assessment of active and planned industrial projects (exploration, mining, refining)
- Development of investment recommendations for the EU based on the raw material project assessment, including additional factors (e.g., ESG, infrastructure, small-scale mining).
- Collaboration and coordination of detailed case studies on the mining sector of the DR Congo and Namibia
- Coordination with EU and African project partners
- Project reporting and public relations, workshop organization and contributions (especially in Africa).

11/2018 – 10/2022   *Research Associate (PhD Student)*
University of Potsdam
GFZ German Research Centre for Geosciences
- Various rock preparation and geochemical laboratory activities
- Numerical modeling of ore deposits in a C++ environment
- Planning of the research budget for procurements and business trips (conferences, workshops, field work)
- Coordination of and cooperation with mining companies (Argentina and USA) and internal and external scientists
- Publishing in peer-reviewed scientific journals
- Teaching assistant and supervision of a Master thesis
- Attendance at national and international conferences

09/2017 – 10/2018   *Student Research Assistant*
TU Bergakademie Freiberg
- Reorganization of the teaching collection (approx. 10,000 ore specimen) and creation of a database
- Preparation of vector graphics and data research for publications on metals of Germany (DESMEX project)

02/2017 – 07/2017   *Student Research Assistant*
Helmholtz Institute Freiberg for Resource Technology (HIF)
- Execution and evaluation of geometallurgical lab experiments

06/2016 – 08/2016   *Internship*
MAXAM Ghana Ltd. und AngloGold Ashanti in Tarkwa (Ghana)
- Planning of open pit blastings
- Production of explosives in a chemical plant
- Drill core logging
- Planning of mine progress

Further professional experience

- Petrography of ore deposits (transmitted and reflected light microscopy
- Fluid inclusions analysis (microthermometry, Raman spectroscopy)
- Rock sample preparation, mineral separation (mechanically, heavy liquids)
- Mineral dissolution/ preparation in the clean lab
- Element separation using standard cation exchange techniques
- Measurement of radiogenic isotope ratios (Rb-Sr, Sm-Nd, Pb-Pb) via thermal ionization mass spectrometry (TIMS)
- Experience in C++ programming/ application of the CSMP++ modeling software
- Visualization software: ArcGis, QuantumGis, ParaView, R, Rhino
- Further software: Inkscape, Adobe Illustrator and Photoshop, Microsoft Office
- Field work and mapping experience: Argentina, Austria, Czech Republic, France, Germany, Ghana, Great Britain, Ireland, Spain, Sweden, Switzerland, USA

Publications, conferences and thesis contributions

Published:

Stoltnow M., Weis P., Korges M. (2023) Hydrological controls on base metal precipitation and zoning at the porphyry-epithermal transition constrained by numerical modeling. *Scientific Reports* **13**:3786.

Stoltnow M., Lüders V., De Graaf S., Niedermann S. (2022) A geochemical study of the Sweet Home mine, Colorado Mineral Belt, USA: formation of deep hydrothermal vein–type molybdenum greisen and base metal mineralization. *Mineralium Deposita* **57**:801-825.

Sośnicka M., De Graaf S., Morteani G., Banks D. A., Niedermann S., **Stoltnow M.**, Lüders V. (2022) The Schlaining quartz-stibnite deposit, Eastern Alps, Austria: constraints from conventional and infrared microthermometry and isotope and crush-leach analyses of fluid inclusions. *Mineralium Deposita* **57**:725-741.

Prepared:

Stoltnow M., Romer R. L., Glodny J., Kärstens J. M. The role of the Laramide orogeny in the formation of Climax-type molybdenite mineralization: constraints from Re-Os and Rb-Sr isotope systematics. Prepared and edited for submission in *Mineralium Deposita*.

Conferences:

Stoltnow M., Weis P., Korges M. (2023) Numerical constraints on the magmatic-hydrothermal fluid evolution forming the Pirquitas Sn-Ag-Pb-Zn deposit in NW Argentina. 17th SGA Biennial Meeting in Zurich, Switzerland (extended abstract)

Stoltnow M., Lüders V., de Graaf S., Niedermann S. (2022) Formation of deep hydrothermal vein-type Mo greisen and base metal mineralization at the Sweet Home mine, Colorado (USA). *EGU* - Copernicus Meetings (online oral presentation).

Stoltnow, M., Lüders, V., de Graaf, S., Niedermann, S. (2021): Formation of deep hydrothermal vein-type Mo greisen and base metal mineralization at the Sweet Home mine, Colorado (USA) -

Abstract Book, *e-CROFI* - European current research on fluid and melt inclusions (online oral presentation).

Stoltnow, M., Lüders, V., Romer, R. L., Weis, P. (2019): Constraining the magmatic-hydrothermal fluid evolution from proximal to distal settings by fluid inclusion and isotopic analyses of ore and gangue minerals - Conference Abstracts, *GSA Annual Meeting*, Phoenix, USA (poster presentation). https://doi.org/10.1130/abs/2019AM-338439

Stoltnow, M., Lüders, V., Weis, P., Romer, R. L. (2019): Constraining the magmatic-hydrothermal fluid evolution from proximal to distal settings by fluid inclusion and isotopic analyses of ore and gangue minerals and numerical modelling - Program and Abstracts, (Terra Nostra - Schriften der GeoUnion Alfred-Wegener-Stiftung; 2019/1), 25th *Latin-American Colloquium of Geosciences* in Hamburg, Germany (poster presentation).

Stoltnow, M., Seifert, T., Jeske, T., Gilbricht, S., Krause, J. (2019): Contributions to the mineralogical and geochemical characterization of Fe-Sn-Zn-Cu-In skarn-type mineralization in the Schwarzenberg mining district, Germany. Proceedings of the 15th Biennial Meeting of the *Society for Geology Applied to Mineral Deposits (SGA)*, Volume 2, Life with Ore Deposits on Earth, Glasgow, Scotland (poster presentation, peer-reviewed extended abstract).

Stoltnow, M., Seifert, T., Jeske, T., Gilbricht, S., Krause, J. (2019) Petrographic, geochemical, and mineral microanalytical characterization of sphalerite from sulfide-rich mineralization in skarns from the Schwarzenberg mining district, Germany. 4th *Geology of Ore Deposits (GOOD)* Meeting, Bremen, Germany (oral and poster presentation).

Supervised thesis:
Kärstens J. M. (2020) Ore Petrography and Geochemistry of the Detroit City Mine, Colorado, USA. Master thesis examined by P. Weis and U. Altenberger. **M. Stoltnow** guided sample selection and preparation, transmitted and reflected light microscopy, mineral separation, sulfur isotope and EPMA data evaluation and performed stylistic improvements.

Participated Workshops and Short courses

05/2019	Fluid Inclusions - Critical Review, Applications, Computer Modeling (Montanuniversität Leoben)
02/2019 – 03/2019	Field methods and digital data analysis DeArGeoNet - LIDAR Workshop, field school NW Argentina
12/2018	Zinc Deposits: 16th Freiberg Short Course in Economic Geology by Sarah Gleeson (GFZ Potsdam), Maria Boni (University of Naples), Markus Schaefer (Vedanta Zinc Int.), Koen Torremans (iCRAG/UCDublin)